THE ELECTRICAL AND OTHER PHYSICAL PROPERTIES OF HALOBORATE GLASSES AND GLASS-CERAMICS

by

A.P. Kemp

A dissertation submitted to the University of Warwick in application for the degree of Doctor of Philosophy

January 1988

DECLARATION

This dissertation is submitted to the University of Warwick in support of my application to the degree of Doctor of Philosophy. It contains an account of my work carried out principally at the Department of Physics of the University of Warwick during the period October 1983 to September 1986 under the general supervision of the late Professor P. W. McMillan and Dr. D. Holland. No part of this dissertation has been used previously in a degree thesis submitted to this or any other university. The work described is the result of my own independent research except where specifically acknowledged in the text.

A. P. Kemp

January 1988

ACKNOWLEDGEMENTS

I would like to express my gratitude to the late Professor P.W. McMillan for his interest, encouragement and general supervision in the early stages of this work. I am indebted to him for making the facilities of the Department available to me.

I would like to acknowledge the ability and effort provided by Dr. Diane Holland to replace him as my academic supervisor following his death. Furthermore, to the academic staff both at the University and Borax Research Ltd., who provided the fuel for many of the ideas presented in this thesis, I express my thanks, particularly Dr. K. Swindon of the University engineering department for useful discussions concerning mechanical strength, and Professor R. Thompson, Dr. J. Farmer, Mr. S. Badzioch and Mr. J.A. Kydd for the knowledge and insight afforded me in the enormous subject of the properties of boron and its many compounds acquired during a series of fruitful discussions.

The contribution of the mechanical workshop technicians, particularly Dan Lee and Pat Boocraft, for their ingenuity, knowledge and expertise, cannot pass unrewarded. Similarly the staff of the electronics workshop, Adrian Lovejoy, Pete Pedrick and Roger Buckle, with their cynical appraisal of "dead" commercial electronics equipment, prior to reviving it at great reluctance, added to my knowledge and understanding of electronic components and circuits in a highly professional yet most enjoyable manner. The light-hearted yet serious approach to microscopy afforded me by Steve York and Gerry Smith can only be experienced as one of life's great adventures. Other contributors to my knowledge, of which only now am I beginning to realise the extent and depth, are too numerous to mention. To be present in such an atmosphere where the experiences acquired only by the passage of time are so freely and glibly relived is, I feel, to be unique and unforgettable. Thank you.

For the "everyday" assistance, patience and understanding, I must not forget the support provided by the resident technicians in the glass-ceramics group, Bob Lamb and Harold Mathers. Contributors to more tangible aspects of my work are Kajal Mallick, for the time spent

in acquiring some of the F.R.A. data presented here, James Bonnyman for working with me to write the conductivity analysis program (?) and Keith Briggs and Dr. Roger Bayliss for the awful jokes that were so welcome in the lean times.

I am further indebted to my examiners, Dr. M. D. Ingram and Dr. R. Pottifer, for their careful reading of the following text and for their suggestions to improve its clarity and accuracy.

My heartfelt thanks are also expressed to Mrs Margaret Carter for her patient and diligent typing of this manuscript.

The provision of the funding for this work by an SERC CASE award with Borax Research Ltd., is gratefully acknowledged.

'Alternative funding', from the many industrial companies, with their donations of materials and specialised technical data, is also recognised.

Finally, I must thank my family for their emotional support and understanding throughout the work described in this thesis, and particularly for their increased encouragement and dynamicism during its writing. It is my sincerest belief that this would not have been possible without them.

ABSTRACT

The effect of a series of classical nucleating agents upon the nucleation and mechanical properties of anhydrous borax ($AB_2Na_2B_4O_7$) glasses and glass-ceramics have been investigated. These results have been compared to those obtained for NaCl-doped compounds and a commercial β''-Al_2O_3 ceramic to examine the applicability of haloborate glass-ceramics as a solid electrolyte in the high temperature sodium-sulphur cell.

The nucleation of these materials was found to be predominantly surface oriented. A new technique has been introduced to increase the number of surface nucleation sites.

Direct and indirect structural comparisons of these materials have been carried out using X-ray diffraction and infra-red and Raman spectroscopy. Results from the NaCl-doped materials have tentatively indicated that the chlorine atom plays a direct structural role. Subtle modifications to the structure are thought to results in previously determined high ionic conductivities.

A variety of techniques have been examined for the measurement of ionic conductivities based on time and frequency domain spectroscopy. A frequency domain measurement system has been designed and built and a computer program written to analyze the acquired data. Equipment exploring a complementary technique based on the multiple disc stacking arrangement postulated by Tubandt has been built. Results from these two techniques appear promising.

CONTENTS

		Page No.
LIST OF FIGURES		iv
CHAPTER 1:	INTRODUCTION	1
CHAPTER 2:	REVIEW	5
2.1	MATERIALS	5
2.2	TECHNIQUES	7
2.2.1	Conductivity	7
2.2.1a	Mechanisms	7
2.2.1b	Dielectric Relaxation	11
2.2.1c	Measurement Systems	14
2.2.2	Structure	20
2.2.2.1	Models of Glass Structure	20
2.2.2.2	Direct Methods of Structure Determination	24
2.2.2.3	Indirect Structure Determination Methods	27
2.2.2.3.1	Infra-red and Raman Spectroscopy	27
2.2.2.3.2	Coefficient of Linear Thermal Expansion	31
2.2.2.3.3	Thermal Properties	32
2.2.2.3.4	Viscosity	36
2.2.2.3.5	Density	37
2.2.2.4	The Structure of Borate Glasses	37
2.2.2.5	The Effect of Halide Addition	39
2.2.3	Mechanical Properties	41
2.2.3.1	Elastic Properties	41
2.2.3.2	Mechanical Strength	41
2.2.3.3	Measurement	45
2.2.3.3.1	Hardness	45
2.2.3.3.2	Toughness	47
2.2.3.3.3	Stereological Investigations	53

		Page No.
2.3	SPECIMEN PREPARATION	54
2.3.1	Melting	54
2.3.2	Annealing	55
2.3.3	Nucleation and Crystallisation	55
2.3.4	Polishing	56
2.4	AIMS OF THE THESIS	58
CHAPTER 3:	EXPERIMENTAL AND RESULTS	60
3.1	PREPARATION	60
3.1.1	Glass Melting	60
3.1.2	Nucleation	62
3.1.3	Machining	65
3.2	CONDUCTIVITY	66
3.2.1	Fixed Frequency Measurements	66
3.2.2	Time Domain Techniques	68
3.2.3	Frequency Domain Dielectric Spectroscopy	72
3.2.4	Transport Number Measurements	82
3.3	STRUCTURE	86
3.3.1	X-Ray Diffraction (XRD)	86
3.3.2	Spectroscopic Investigations	88
3.3.2.1	Infra-red Studies	88
3.3.2.2	Raman Spectroscopy	90
3.3.3	Thermal Expansion Coefficient	92
3.3.4	Thermal Properties	92
3.3.5	Density	93
3.4	MECHANICAL PROPERTIES	94
3.4.1	Young's Modulus	94
3.4.2	Hardness	94
3.4.3	Fracture Toughness, K_{1c}	94

Page No.

3.4.4 Fractographic Analyses 96
3.4.4.1 Sodium Chloride Doped Glass-Ceramics 96
3.4.4.2 P_2O_5-Doped Materials 97
3.4.4.3 TiO_2-Doped Materials 97
3.4.4.4 Platinum Nucleated Materials 98
3.4.5 Sodium β'' alumina 98
3.4.6 Interpretation of Mechanical Property Measurements 99
3.4.6.1 Overview 99
3.4.6.2 NaCl 101
3.4.6.3 P_2O_5 102
3.4.6.4 TiO_2 102
3.4.6.5 Platinum 103

CHAPTER 4: DISCUSSION 104

CHAPTER 5: CONCLUSION 109

CHAPTER 6: FUTURE WORK 112

REFERENCES 114

APPENDICES

LIST OF FIGURES

Figure		Follows Page No.
1.1	The principle of load levelling	1
1.2	Practical efficiencies of a selection of energy storage systems	2
1.3	Schematic drawing of the sodium-sulphur cell	2
2.1	Explanation of a simple ionic conduction model using a one-dimensional potential well	9
2.2	Illustration of the mismatch functions obtained for different theoretical fits of conductivity data	11
2.3	The basic principle of a 4-point measurement technique	15
2.4	Data representations used in complex impedance analysis	19
2.5	Nominal equivalent circuit for a polycrystalline conductivity specimen	20
2.6	Effect of modifier addition upon the structure of a silicate glass	22
2.7	Effect of modifier addition upon the structure of a borate glass	24
2.8	Variation of number of 4-coordinated boron atoms with modifier content in borate materials	26
2.9	Structure and nomenclature of groups found in borate glass	26
2.10	Energy level diagrams indicating transitions in infra-red and Raman spectroscopy	28
2.11	Infra-red spectra for a series of different metal oxide-borate glasses having the same modifier content	30
2.12	Potential well diagram used to explain thermal expansion behaviour	31
2.13	The relationship between the liquid, solid and glassy states	33
2.14	Variation of linear thermal expansion coefficient with modifier content	37
2.15	Illustration of quantities used in equations for Young's modulus and K_{1c} determinations	41
2.16	Typical strength distributions for specimens having different degrees of surface damage	42
2.17	Illustration of Vickers and Knoop impressions	46
2.18	The three fracture modes encountered in mechanical strength testing	48
2.19	Variation of specimen compliance with notch to depth ratio for two different calibrations	49
2.20	Nomenclature of the cracks formed from a sharp indenter.	50
2.21	Comparison of toughness values obtained using indentation and conventional means	51

Figure		Follows Page No.
2.22	Model of stress corrosion mechanism in silica glass	53
2.23	Crystal nucleation and growth kinetics	56
2.24	Classical interpretation of polishing damage via the Beilby layer	57
2.25	Illustration of a new polishing criterion using an elastic-plastic deformation theory	57
3.1	Graph showing rate of chlorine loss with melting time in a chloroborate glass	61
3.2	Hot stage micrograph showing poor nucleation and spherulitic growth in glassy borax	62
3.3	Effect of particle size and chemical composition of the surrounding powder on the nucleation properties of glassy borax	62
3.4	Nucleation studies of glassy borax using NaCl	63
3.5	Nucleation studies of glassy borax using P_2O_5	63
3.6	Nucleation studies of glassy borax using TiO_2	63
3.7	Nucleation studies of glassy borax using Pt	63
3.8	The effect of water upon the crystallisation behaviour of glassy borax	63
3.9	Examples of a microscopic investigation of air-etched polished sections of borax nucleation specimens	64
3.10	Examples of a microscopic investigation of water-etched polished sections of borax nucleation specimens	64
3.11	Schematic of the conductivity measurement apparatus used by Borax Research Ltd.	66
3.12	Examples of resistivity hysteresis behaviour in the Arrhenius plot for a $90Na_2B_4O_7.10MnCl_2$ (wt. %) melt	66
3.13	Averaged Arrhenius plots of a series of $Na_2B_4O_7$-$MnCl_2$ melts	67
3.14	Variation of resistivity isotherms with manganese content for a series of $Na_2B_4O_7$-$MnCl_2$ melts	67
3.15	Electrode geometry used in "d.c." and time domain spectroscopy conductivity measurements	69
3.16	Arrhenius plots for Pilkington's float glass	71
3.17	Arrhenius plots for a $90CaB_4O_7.10CaCl_2$ glass-ceramic with silver plate electrodes	71
3.18	EDAX analysis of silver concentration with depth for a glass-ceramic specimen coated with silver paste electrodes during a series of conductivity measurements	71

Figure		Follows Page No.
3.19	Schematic diagram of the measured time dependences of current flowing during a "d.c." conductivity measurement for a given applied voltage sequence	71
3.20	Illustration of some data fitting trials from time domain studies of Pilkington's float glass	71
3.21	Schematic diagram of the cell constructed for frequency domain conductivity measurements	74
3.22	Timing diagram for data acquisition from the Solartron 1180 plotter interface	76
3.23	Various representations of input and output voltages in a.c. measurements	76
3.24	Theoretical Cole-Cole plot illustrating the phenomenon of depressed semicircles for a combination of discrete electrical components	77
3.25	Cole-Cole plot for the test circuit built for the 1172 and attempt at evaluation of component values	77
3.26	Typical Cole-Cole impedance plot obtained from the Coors Al_2O_3 substrate used as a secondary test to demonstrate goodness of theoretical fit	79
3.27	Arrhenius resistivity plot for a Coors Al_2O_3 ceramic substrate, the values having been inferred from optimisation techniques	79
3.28	Arrhenius resistivity plot obtained by fitting Coors data to two distinct relaxation mechanisms via an optimisation routine	79
3.29a	Cole-Cole impedance plot illustrating the anomalous responses obtained for borax-based glasses	80
3.29b	Arrhenius resistivity plot obtained "geometrically" for $Na_2B_4O_7$-NaCl glass specimens	80
3.30	Typical Cole-Cole plot for the glass-ceramic conductivity specimen showing "normal" behaviour	80
3.31	Cole-Cole plot for the glass-ceramic conductivity specimen exhibiting an electrode dissolution reaction 1: Introduction of a Warburg impedance	81
3.32	Cole-Cole plot for the glass-ceramic conductivity specimen exhibiting an electrode dissolution reaction 2: Warburg impedance combined with intermediate frequency loop	81
3.33	Arrhenius plot for a $80Na_2B_4O_7.20NaCl$ glass-ceramic specimen	82
3.34	Arrangement of disc specimens in a Tubandt experiment	84
3.35	X-ray diffraction data for NaCl-doped glass-ceramics	87
3.36	X-ray diffraction data for P_2O_5-doped glass-ceramics	87
3.37	X-ray diffraction data for TiO_2-doped glass-ceramics	87
3.38	X-ray diffraction data for TiO_2-doped glass-ceramic specimens formed in a 3-stage heat treatment	87

Figure		Follows Page No.
3.39	X-ray diffraction data obtained at Harwell	87
3.40	Comparison of X-ray diffraction spectra for a devitrified $Na_2B_4O_7$ specimen	87
3.41	Comparison of X-ray diffraction spectra for a devitrified $90Na_2B_4O_7.10NaCl$ specimen	87
3.42	MATR arrangement for infra-red spectroscopy	88
3.43	Comparison of infra-red data obtained by different methods	89
3.44	Infra-red spectra obtained from NaCl-doped materials	89
3.45	Example infra-red difference spectrum from two devitrified haloborate glasses	89
3.46	Raman spectra of NaCl-doped glasses	91
3.47	Raman spectra of NaCl-doped glass-ceramics	91
3.48	Schematic D.T.A. arrangement	92
3.49	Typical D.T.A. trace	93
3.50	Drawing of notching jig used for specimen preparation for SENB K_{1c} tests	95
3.51	Drawing of 4-point bend jig used for fracture toughness tests	95
3.52	Load-displacement curves obtained during strength tests of glassy and devitrified materials	95
3.53	Typical fractographic investigation of a glassy specimen	96
3.54	Examination of the fracture surface of devitrified borax	96
3.55	Fractographic investigation of a $90Na_2B_4O_7.10NaCl$ glass-ceramic specimen	96
3.56	Fractographic investigation of an $80Na_2B_4O_7.20NaCl$ glass-ceramic specimen	97
3.57	Fracture surface of a devitrified $99Na_2B_4O_7.1P_2O_5$ fracture toughness specimen	97
3.58	Fracture surface of a devitrified $98Na_2B_4O_7.2TiO_2$ fracture toughness specimen	98
3.59	Fracture surface of a devitrified $Na_2B_4O_7$ + 10^{-4} mol % Pt fracture toughness specimen	98
3.60	Fractographic analysis of a commercial β''-Al_2O_3 ceramic	98

CHAPTER ONE
INTRODUCTION

One of the chief areas currently attracting a great deal of commercial attention is that of the production and efficient usage of energy, a consequence of the numerous predictions of the limited extent of remaining fossil fuel resources. The notable options for future provision of electrical power that have been developed so far fall into three main categories; "clean" discontinuous sources such as solar, wind and tidal power; "clean" continuous sources, including geothermal energy and also proposed nuclear fusion power stations, and finally the arguably "dirty" continuous nuclear fission plants already in use. However, all of these choices suffer from an inability to respond rapidly to consumer demand, which changes sharply depending on time of day and season. Consequently, a "spin-off" from this intense research programme has been to investigate, optimise and commercially produce a means of energy storage that can be employed simply and efficiently on both a short- and long-term basis. The principle of "load levelling" is illustrated in Figure 1.1.

Just as there are many new and diverse forms of energy production, so there are equally diverse storage mechanisms, including fuel cells, gravity feed liquid storage tanks, and direct electrical storage in electrochemical cells. Each technique has its own particular problems: fuel cells with storage and controlled release of potentially explosive chemicals; liquid storage by limited sites which may have other uses; and electrochemical cells by electrode/electrolyte degradation and containment. Therefore, it would appear most promising in the long term to concentrate effort on a fuel cell/electrochemical cell system, and attempt to solve technological, rather than environmental and ecological problems.

Although both types of cell require materials that are cheap to manufacture, economic to operate and durable throughout several hundred charge and discharge cycles [1], it is to the electrochemical power sources which we shall now devote our attention.

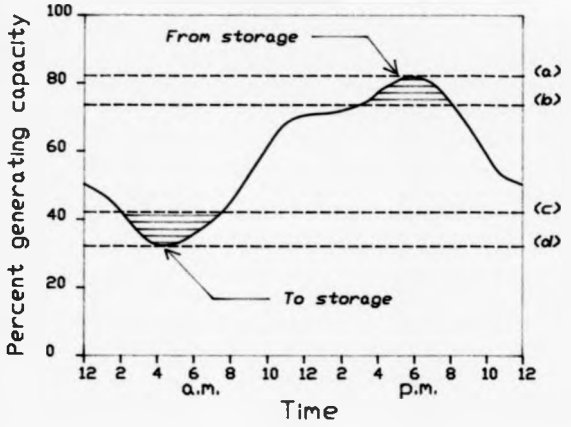

(a) Maximum load

(b) Maximum load with storage

(c) Minimum load with storage

(d) Minimum load

Figure 1.1.

Basic principle of load levelling. Figure indicates reduced dependence upon fossil fuels by storage of off-peak electrical power.

Probably the easiest starting point is to examine the electrical efficiency of a variety of cells. This is displayed graphically in Figure 1.2, which shows specific power (energy release rate per unit mass) vs. specific energy (total recoverable energy per unit mass) for some commercial and experimental storage systems. It must be emphasised that this is only a general guide, since other factors such as rate of open circuit discharge (length of time taken for a cell to discharge without any external loading, caused by electronic, rather than ionic, charge transfer between the electrodes) have not been considered. From the figure, it can be seen that there are cells having values of specific power and specific energy superior to the lead-acid batteries currently adopted for general domestic and industrial usage. These cells are of the liquid electrode, solid electrolyte type. Here, the mobile ionic species can pass through the solid electrolyte with similar conductivities to those observed in analogous liquid electrolyte cells. These materials, which have only been investigated for the past thirty years or so, are known as fast ion conductors (FIC's). These cells usually operate at elevated temperatures (typically 300 - 400°C), to benefit from a higher electrolyte conductivity, as well as to melt the electrode materials.

Much of current industrial interest is directed to the lithium and sodium-based cells, due to the high relative abundance of the constituent materials. Historically, however, it was the announcement of the Na-βAl_2O_3 solid electrolyte in 1966 by the Ford Motor Company in the United States [2] and the ensuing research programme that revolutionised the design and fabrication of high-temperature cells and sparked off the recent research drive by many groups in Europe, the USA and Japan. The main interest is the Na-S cell, which is illustrated schematically in Figure 1.3.

In spite of the apparently ideal suitability of Na-βAl_2O_3 as a solid electrolyte material from the point of view of high Na ion conductivity, low electrical conductivity and high mechanical strength, the cell itself is still in the developmental stage due to the associated materials problems, namely degradation from both liquid sodium and sulphur, and sodium diffusion at the α-Al_2O_3/β-Al_2O_3 interface, leading to crack formation and failure. These problems are, however, being slowly overcome.

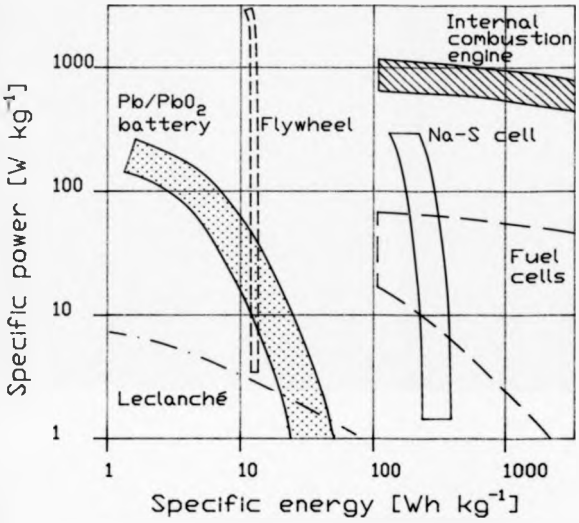

Figure 1.2.
The relative efficiencies of some commercial and experimental storage systems.

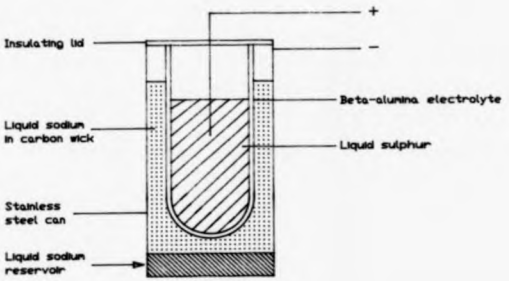

Figure 1.3.
The sodium-sulphur cell.

One problem was the formation of high tolerance tubes on a production line basis. An early technique was that of slip casting [3]; the mixing of fine-grained sodium aluminate powder ($Na_2O + Al_2O_3 \xrightarrow{1400°C} NaAl_2O_4$) and α-Al_2O_3 with liquid to form a slurry, which was poured into a mould and the liquid evaporated off before firing at 1450°C to sinter the final product. This resulted in the formation of pores, and also of regions of inhomogeneous thickness, leading to "hotspots" in the prototype versions and thereby accelerated failure. The current production technique employs Hot Isostatic Pressing (HIPing) [4], which yields a higher proportion of better quality tubes. However, the process of electrolyte degradation is still not fully understood [5], and therefore cannot be overcome with the same degree of ease as tube production.

An alternative solution to this problem is to develop another electrolyte material which has a reduced susceptibility to Na ion diffusion and chemical attack. One group of materials which have been the subject of considerable experimentation are sodium borate- based glasses [6, 7], but these have not been commercially exploited due to their reported low ionic conductivities. However, in a recent piece of work, Badzioch [8] showed that devitrified halide-doped borax-based ($Na_2O.2B_2O_3$) glasses appeared to exhibit higher (~ x 10^3) conductivities than that of the base glass. This was verified to an extent by Daniels [9] who carried out more systematic studies of this glass system.

A necessary extension of this exploratory work is to develop and categorise these materials more fully so as to optimise their technical and commercial viability. The advantages of a glass-ceramic based material are that subtle changes can be made in the chemical composition of the parent glass, which can produce quite remarkable physical property variations upon devitrification. Generally, lower melting temperatures are possible, thereby reducing initial preparation cost. Furthermore, more versatile casting techniques provide a route for less complex tube production, with the possible incorporation of a blocking graded seal to reduce sodium ion diffusion and the attendant interfacial cracking at the α-alumina seal. Finally, if one of the models for electrolyte degradation is correct, namely precursor crack growth from pockets of liquid sodium trapped in the intercrystalline voids present in β-alumina, then the lower porosity of a glass-ceramic could appreciably reduce this problem.

The purpose of the present work is to attempt to explain the apparent conductivity enhancement on a structural basis, and to perform basic tests on these haloborate glass-ceramics to assess their applicability for usage in an electrochemical cell.

CHAPTER TWO
REVIEW

2.1 MATERIALS

The definition of a 'glass', or more generally an amorphous material, is problematic for reasons which are reflected in its many diverse uses in science, engineering and art, i.e. its immense versatility in production, appearance and usage. Previous attempts at definition have been based on the atomic sizes of constituent elements [10] and on the lack of long-range order on the microscopic level as evidenced by the diffuse haloes obtained from X-ray diffraction (XRD) patterns [11], but in all cases the entire range of compositions cannot be shown to be glassy by performing a single experiment. One of the most quoted definitions was proposed by the American Society for the Testing of Materials (ASTM) in 1945, that "glass is an inorganic product of fusion which has cooled to a rigid condition without crystallising". This excludes any organic glass systems and the spectrum of compounds that can be formed by methods other than melting, e.g. by vapour deposition. The problems associated with an accurate definition have been expounded by McMillan [12]. The most recent definition [11] is discussed later (section 2.2.2.3.3).

On the basis of the above definition, however, certain of the general properties of glassy materials can be qualitatively interpreted by comparison with other technological analogues.

Since there are no crystalline grains present, there are no grain boundaries (hence the transparency of a single phase glass), thereby eliminating their contribution to mechanical failure. This is observed in practice, since pristine glass has a high mechanical strength until surface flaws are externally introduced, either by corrosion or by abrasion [13]. Similarly, once these flaws are present and the glass is strained, at some critical stress value the crack will extend unimpeded and break each chemical bond in its path individually, which will require approximately the same force throughout, and so will propagate very quickly. For this reason glasses exhibit "fast" or "brittle" fracture characteristics.

If, however, a ceramic material having a high density of small crystallites connected by a low proportion of residual glass is considered, and the bonding between the glassy and crystalline phases is strong, then a similar crack will in general require more energy to propagate through this composite; the crack having to "start" and "stop" on a microscopic level to overcome the different critical stresses

The way in which other properties of this agglomerate differ from those of glasses may also be interpreted from this viewpoint.

For example, in a crystalline material, ion transport is inhibited in general by the small free volume present as a consequence of the inherent periodic arrangement; i.e. the number of vacant sites and the routes an ion may take to reach them are low. The corresponding glass, however, by virtue of the more "random" atomic arrangements, produces a strained network having a higher net interatomic separation and thus larger "channels" through which ions may pass more easily. It must be remembered that this size criterion alone is not sufficient to obtain high measured conductivities, as shown by a series of numerical calculations of structure oriented electrostatic interactions in FIC materials [2], although the above description does allow for a broader distribution of channel sizes and hindering barrier heights which increases the likelihood for optimum transport conditions to be obtained within the network as a whole.

Additionally further conduction pathways are available within a polycrystalline material, either along the linking grain boundaries or through the residual glass phase.

Within the constraints of this presented concept, it is therefore unlikely for the conductivity of a polycrystalline compound to exceed that of a glass of equivalent composition since the distribution of optimum conduction pathways will be lower over macroscopically large distances in the composite. Moreover, the effects of "blocking" channels having conductivities superior to those in the glass by large immobile impurity ions or high densities of the smaller majority charge carriers will be more marked.

If the crystals can be grown from a large number of evenly- dispersed nuclei within the glass matrix in a controlled fashion, then the final product is termed a "glass-ceramic" [12], which can be engineered to a specific requirement by changing parameters such as crystal phase, volume fraction and grain size. If, however, crystallisation occurs from relatively few nuclei, then this is termed uncontrolled devitrification and the end product is not, in general, as useful as a glass-ceramic. An alternative production technique is to obtain crystalline powders of the required particle size distribution and heat them at a fraction (~ 2/3) of the measured liquidus temperature (the temperature below which a single liquid phase is thermodynamically unstable) and diffusion of various species will occur, leading to fusion of the crystallites [14]. (An alternative may be to heat above the solidus [3]). This is known as sintering and is generally used for high melting point composite materials, or where a high proportion of crystal is required. Typically a glass-ceramic will contain 5 - 10% glass by volume, and a sintered ceramic < 2% [12]. However, articles produced by sintering will, by the nature of the process, contain "voids" between the crystallites which constitute porosity and exhibit enhanced corrosion rates when used as a solid electrolyte [15]. A more detailed comparison of these three types of material is given below in terms of measurements that can be and are made on both a commercial and scientific basis.

2.2 TECHNIQUES

2.2.1 Conductivity

2.2.1a Mechanisms

Electrical conduction occurs due to the cooperative movement of either electrons or ions under the influence of an applied potential gradient. The ease with which this transport process is effected is reflected in a high measured conductivity value. Typical results for a series of material classes are shown in Table 2.1, together with the presumed predominant conducting species. However, compounds possessing comparable contributions from more than one type of charge carrier, known as mixed conductors, are known to exist [16].

Table 2.1 Typical Conductivities for a Series of Materials

Type of Conduction		Approximate $\log_{10}$ Conductivity at 20°C (Ω^{-1} cm^{-1})
Electronic	Ionic	
	Fused silica	-22
PTFE		-20
High Alumina ceramic (95% Al_2O_3)		-15.3
Lithium Alumino-silicate glass		-13.7
	Window glass	-12
Pure silicon		-5
	$Na_2O.11Al_2O_3$ (sodium β^2-alumina)	-1.7
	$RbAg_4I_5$	-0.5
Pd-Si amorphous alloy		3
Copper		6

Conductivity values are usually temperature dependent, thereby requiring the presence of an additional quantity (the Boltzmann activation energy) to effect a complete description of the behaviour of a linear, macroscopically homogeneous, isotropic specimen. For materials not fitting this description further parameters may be introduced to take note of harmonic, directional and localised composition effects respectively. Furthermore, in all cases except metals, (where a higher temperature corresponds to increased phonon densities in the lattice, and hence greater disruption of the periodic potential wells through which the electrons travel) an increased conductivity is measured with increasing temperature as more potential charge carriers are excited to higher states.

Since the electronic transport in the majority of solid materials is now described fairly accurately by theoretical models backed up by a substantial database of high-quality experimental data comprising a wide variety of specimens, electronic conduction will be ignored in the following review by limiting future discussion to materials which have a large electron band gap ($\gg$ ionic activation energies). A preliminary introduction to the theory and experiment of electronic conduction in solids can be obtained from the references cited for metals [17], semiconductors [18], and dielectrics [19].

In general ion transport is not easily measured in ionic or covalent solids under ambient conditions, movement from their normal lattice sites only occurring via crystal defects. It is only at more elevated temperatures (a significant fraction of the liquidus temperature) that an increased defect population can produce more measurable conductivity values, and the mobile species can be thought of as a fluid passing through a lattice "sponge".

There exists a group of materials that exhibit this property at temperatures much lower than the liquidus but above some characteristic transition temperature. These materials are known as fast ion (or superionic) conductors (FICs). Interestingly, they all appear to exhibit a characteristic thermal phase transition of some kind that coincides with the transition from the low to the high conducting state, which may be (and often is) interpreted in terms of the "melting" of the "liquid" sub-lattice. Indeed, thermodynamic calculations of the sum of the enthalpy changes in this phase transition and the melting of the residual "rigid" lattice "sponge"

correlate remarkably well with a theoretical value of the specific heat calculated on the basis of no low-temperature phase transition [20].

The transport mechanisms postulated for FICs do not rely on semi-quantitative arguments involving enhanced defect concentrations but on the presence of conducting "channels" throughout the crystal, and have not, except in rare cases where a great deal of high quality structural work has been performed, been fully explained [20]. From these few proposals, it seems apparent that no simple theory will be able to encompass all the observations and specific structural interpretations made from the ever increasing number of mono- and multi-valent anion and cation conducting systems that exhibit this remarkable property. Therefore, it is felt that each system must be treated essentially individually for the present time.

In an attempt to state our principal structural requirement for a highly conducting material, it seems reasonable to require the compound to possess as many highly "conducting channels" as possible, both to pass ions through the matrix, and (in a polycrystalline solid) to increase the probability of transference from one "channel" to another between grains. As an example of the materials investigated so far, McGeehin and Hooper [21] review the 1, 2 and 3 dimensional conduction paths for a selection of well-known FICs (e.g. the tungsten bronzes, β-Al_2O_3 and AgI) and tabulate their conductivities for comparison.

The conduction process may be understood by reference to a simple theory of ion conduction [22]. Figure 2.1a indicates a distribution of potential wells that a would-be mobile ion carrying charge Ze may face in a perfect 1-dimensional crystal with no applied electrical potential. The transport is thermally activated and is proportional to the Boltzmann factor $\exp(-E/kT)$, where k is the Boltzmann constant and T is absolute temperature. In Figure 2.1b, the height of the barrier has been effectively lowered by an amount $(Ze\varepsilon d)/2$ in the direction of the applied field ε, thereby leading to a net flow of ions from A to B.

When correlation effects are observed in ionic motion (i.e. the change in the field surrounding a potentially mobile ion when a neighbouring mobile ion has "hopped" to leave a vacancy), information about the mechanism can be obtained from a comparison of chemically

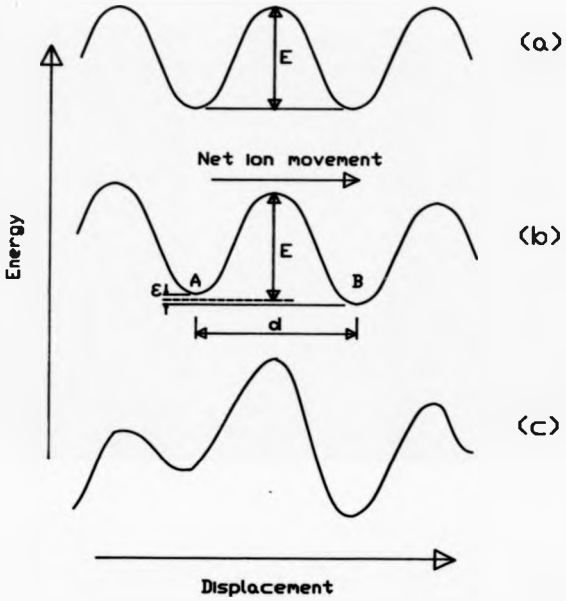

Figure 2.1.

One-dimensional potential barriers in a simple model of ionic conductivity.

and electrically-determined diffusion constants D. This is parameterised via the Haven ratio H_R, provided as a correction for this correlation of ion movements observed under the influence of an applied electric field when compared with chemically-driven radioactive diffusion experiments via a modified Nernst-Einstein equation [23]

$$D_i = \frac{H_R kT \sigma_i}{n_i (Z_i e)^2} \qquad (2.1)$$

where σ_i, n_i and Z_i are the conductivity, number density and charge associated with conducting species i in the material under investigation. In general, H_R varies between 1 (for no correlation) and 0.6.

Now assume that the "mobile" ion has a residence time τ_0 in a given well, and the time of flight to the next well is τ_1. This leads to two extreme cases:

1. $\tau_0 \gg \tau_1$, and the ion movement is occasional i.e. solid state behaviour,
2. $\tau_1 \gg \tau_0$, and transport occurs virtually all the time i.e. liquid-like behaviour.

In both cases the surrounding lattice has to accommodate these movements, and this is the basis of an alternative kinetic theory developed to explain FIC [20], its success stemming from the inability to model liquids in a more rigorous and meaningful manner.

The potential barrier model can also qualitatively explain one further relevant observation; that of measured conductivity in a glassy material being higher than its polycrystalline analogue in many cases ([24], section 2.1). In this instance, it is reasonable to assume a random distribution of stationary ions, and hence of potential barrier heights (Figure 2.1 c) in an amorphous material having a lack of long range order, and that mobile ions will ultimately pick the route through the barriers having as small an activation energy as possible, thereby showing the higher measured conductivity value. The reported exceptions are due to the rejection of alkali ions by the crystal phase into the residual glass upon conversion to the glass-ceramic [24]. This produced an exceptionally highly conducting glass matrix, thereby leading to a spurious result in the overall measured conductivity.

Finally, the temperature dependence of ionic conductivity also seems to present a further complication to the theoretical description, in that it does not appear to follow predicted trends accurately. Jain [25] has examined the fit of conductivity values for several alkali borate and silicate glasses to four expressions, of which only three were reported to have any theoretical basis. The published findings indicate that a two parameter fit, not surprisingly, gives a smaller least squares difference than a single parameter one; the second variable being explained as a measure of the width of the (Gaussian) distribution of activation energies in the materials. However, the figures presented in this work to illustrate the "goodness of fit", by plotting the relative difference between theory and experiment (the "mismatch function") as a function of reciprocal temperature show similar features, as illustrated in Figure 2.2. The effect of the different theoretical expressions upon the "mismatch function" appears to merely change the magnitude of the discrepancy, and not the shape. This indicates to the author that there may be a previously unobserved additional structure-based contribution superimposed upon the base conductivity variation which may require explanation in future theoretical expressions.

2.2.1b Dielectric relaxation

Having considered in a generalised summary the way in which ionic conduction occurs in materials, it would now seem appropriate to illustrate charge transport on a more physical level as a precursor to measurment, to aid in deciding upon the type of experiment to be performed, and the information that may be obtained therefrom.

Following the route taken by a standard text [17], the assumption is made that a (single) relaxation time can be defined, and then the effects of supplying a static and alternating electric field to the material under test are expressed on a more mathematical basis.

The concept of the relaxation time τ is introduced as a measure of the rate by which the charge polarisations present respond to changed in the applied field. If changes in the applied field occur in times smaller than τ, then the charges will be unable to "follow" the field; but will interact with the applied field for changes in time greater than τ. It is the interlacement between these two extremes that provides the information desired by the experimentalist

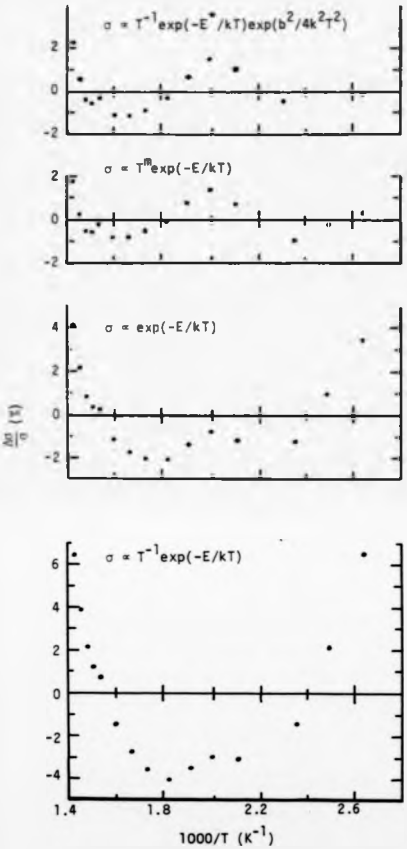

Figure 2.2. Illustration of the mismatch functions obtained for different theoretical fits of conductivity data. (After Jain [25]).

performing material categorisation. That a single relaxation time can be inferred from experimental data is another facet of an old and much maligned concept; namely the deduction of microscopic information from a

For the time being, it is to the dipolar source of polarisation that we shall direct attention, since these are generally assumed to have the largest response times of the polarisation mechanisms considered by solid state physicists.

Upon application of a static electric field E, the "steady state" saturation dipolar polarisation will be given as P_{ds}, so the value of dipolar polarisation P_d at time t may be tentatively expressed as

$$P_d(t) = P_{ds}(1 - e^{-t/\tau}), \tag{2.2}$$

or, in differential form,

$$\frac{dP_d(t)}{dt} = \frac{1}{\tau}(P_{ds} - P_d(t)). \tag{2.3}$$

This equation may also be employed in the case of an alternating applied field $E = E_o e^{j\omega t}$ if the following generalisation is made: since the electric field is now time varying, so the saturation polarisation will be time varying also, in that $P_{ds}(t)$ will be the polarisation obtained for the instantaneous applied field E(t). Therefore the more generalised differential equation becomes

$$\frac{dP_d(t)}{dt} = \frac{1}{\tau}(P_{ds}(t) - P_d(t)). \tag{2.4}$$

The "instantaneous" dielectric constant $\varepsilon_{(\infty)}$, determined by the "fast" response polarisations $P_{(\infty)}$ (due to electronic and atomic movements, for example), is now defined:

$$P_{(\infty)} = \varepsilon_{(\infty)} E \tag{2.5}$$

The total polarisation may now be expressed as

$$P_{ds} = P_s - P_{(\infty)} = (\varepsilon_{(0)} - \varepsilon_{(\infty)})E, \tag{2.6}$$

where $\varepsilon_{(0)}$ is the "static" dielectric constant (i.e. at zero frequency). Substituting (2.6) into (2.4) gives

$$\frac{dP_d}{dt} = \frac{1}{\tau}\left((\varepsilon_{(0)} - \varepsilon_{(\infty)})\, E_o e^{j\omega t} - P_d\right). \qquad (2.7)$$

Solving (2.7), we obtain

$$P_d(t) = Ce^{-t/\tau} + \frac{\varepsilon_{(0)} - \varepsilon_{(\infty)}}{1 + j\omega\tau} E_o e^{j\omega t} \qquad (2.8)$$

Considering the steady state component only, and substituting this into the definition of the electric displacement D, we obtain

$$D(t) = \varepsilon^* E(t) = \varepsilon_{(\infty)} E(t) + P(t). \qquad (2.9)$$

ε^* is the complex dielectric constant, normally expressed as

$$\varepsilon^* = \varepsilon' - j\varepsilon''. \qquad (2.10)$$

Combining (2.8), (2.9) and (2.10), expressions for ε' and ε'' result

$$\left.\begin{aligned} \varepsilon'(\omega) &= \varepsilon_{(\infty)} + \frac{\varepsilon_{(0)} - \varepsilon_{(\infty)}}{1 - \omega^2\tau^2} \\ \varepsilon''(\omega) &= (\varepsilon_{(0)} - \varepsilon_{(\infty)}) \frac{\omega\tau}{1 + \omega^2\tau^2} \end{aligned}\right| \qquad (2.11)$$

These last two relationships are known as the Debye equations. An equivalent result is obtained from a modified lattice dynamics-based argument [26].

To visualise the ramifications of the above result, it would seem easiest to consider the effect of a periodic external field upon an ideal capacitor. Simple a.c. theory provides the result that a current, determined by the capacitative reactance $1/\omega C$, will flow due to a charge/discharge process, and will "lead" the applied field by 90°. In a practical capacitor, the charge transfer from the polarisation charge will generate heat by a series of phonon interactions, which is equivalent to resistive-type losses. Since a current through a resistor is in phase with the electric field applied through it, the phase angle between field and current observed in a capacitor will be less than 90° by a material constant δ.

Therefore, for a field $E = E_o e^{j\omega t}$, the associated displacement within the specimen will be $D = D_o e^{j(\omega t - \delta)}$, where $(90-\delta)$ is the measured phase angle. From (2.9),

$$\varepsilon^* = \left|\frac{D_o}{E_o}\right| e^{j\delta}, \tag{2.12}$$

which may be decomposed via (2.10) into

$$\left.\begin{aligned} \varepsilon' &= \left|\frac{D_o}{E_o}\right| \cos\delta \\ \varepsilon'' &= \left|\frac{D_o}{E_o}\right| \sin\delta \end{aligned}\right| \tag{2.13}$$

which is an equivalent form of (2.11). It may be easily shown that the energy loss is governed by ε'', hence the reason that $\sin\delta$ is referred to as the loss factor of a circuit component. However, since $\tan\delta = \varepsilon''/\varepsilon'$ is more readily calculable, this is generally taken to be the loss factor, but is only valid for small values of the loss angle δ.

From the above two proofs (equations (2.11) and (2.13)), it can be seen that an equivalence exists between a dielectric material and a parallel contribution of a pure resistance and a pure capacitance. This results in a considerable simplication in data analysis, enabling a single relaxation mechanism to be represented by a parallel R-C network, and following a simulation using this strategy the resistance and capacitance values obtained used to derive the dielectric constants for the material under investigation.

2.2.1c Measurement Systems

In order to report accurate and meaningful conductivity values for an ionically-conducting material, several fundamental difficulties have to be faced, and where possible, overcome. Ideally the "d.c." or steady state condition should be chosen to ensure that the measured effect is indeed due to long range ion transport and not simply to ions migrating to low barrier height potential wells under the influence of an applied step voltage as described in section 2.2.1a.

The principal conceptual problem is how the transition between the "pure" electronic conduction of the measuring systems' connecting wires and the speculated highly ionic conduction in the specimen under test is effected. For the case of good charge transfer between electrons and ions (e.g. in liquid electrolytes such as $CuSO_4$ with Cu or Zn electrodes), the region in which this occurs is referred to as the electrical double layer, since a "polarisation" effect arises from a depletion region in the specimen caused by charge conservation at the interface. The various situations arising at the interfaces in solid electrolytes have been analysed by Bergmann and Tannenberger (Chapter 11 in reference [23]). However, in the light of our earlier assumption of a high electron band gap, this transfer process is further complicated by a space charge build up that has been discussed in some detail by Couturier et al. [27], who also proposed a new technique for ionic conductivity measurement to try and overcome this problem. This comprises a four terminal measurement system shown schematically in Figure 2.3, with the central measurement electrodes "situated symmetrically in the bulk of the sample ... not too close to the interfaces" to measure the voltage within the specimen (presumed to be characteristic of pure ion transport) and the outer electrodes serving the dual purpose of supplying the drive voltage and measuring current flow.

This problem is eliminated in more conventional experiments by using either a suitable intermediate electrode material* or modelling the effect and finally removing it numerically from the data obtained from a simpler measurement system, since the double layer appears merely as a capacitor (from the effect of the depletion region).

---

* For example, liquid sodium for a sodium ion conductor [28], thereby allowing ion transport across the specimen-electrode interface. This type of electrode is known as non-blocking or reversible, since it permits conduction by both electrons and the mobile ions in the specimen, whereas previously only blocking electrodes have been discussed. One immediate experimental problem with this type of system is the containment and usage of sodium metal, and so an alternative, safer option, using solid non-blocking contacts, such as sodium β-alumina, could be used instead. The difficulty with this would be in determining those areas of electrode and specimen materials which are in sufficiently intimate contact to allow ion transfer. This will be addressed in a later section.

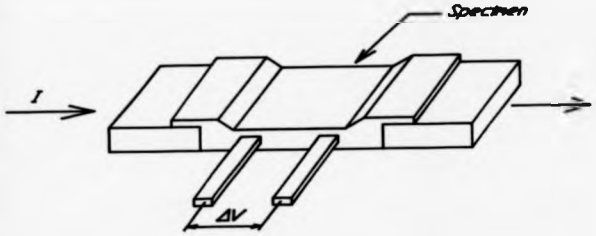

Figure 2.3.

Four-point measurement used to eliminate electrode effects in conductivity measurements.

The second experimental difficulty now becomes apparent - the measurement of the "d.c." current. Because of the slow tail-off following the rapid initial decrease in current after the step voltage has been applied, it becomes more difficult to interpret the steady state condition, and to eliminate any noise from what may be a bona fide structural response. By this reasoning, the alternative strategy also in widespread general usage may be arrived at. This is to characterise the sample by making measurements over as wide a range of distinct frequencies as possible, and interpret the appropriate system behaviour before extrapolating the conductivity frequency dependence to zero (i.e. infinite time) to obtain the "d.c." value. The equivalence of the two measurements is validated since the transport mechanisms in the low frequency limit will be similar to those in the "d.c." analogue. This technique is known as frequency response analysis (FRA).

Whilst the advantage of an increased signal to noise ratio from the use of phase-sensitive detection is well-known [29], there is a strong disadvantage with this type of measurement at the low frequency end of the spectrum, specifically long times are required to perform measurements over a single voltage cycle.

Disappointingly, though, a good deal of published data on glasses and ceramics only refer to measurements at a single frequency, or worse, "d.c." values are reported which have been obtained by measuring the transient current some (generally unspecified, but presumed fairly long) time after application of a step voltage [30-33]. In light of the preceding discussion and results to be presented, the conclusions that can be formed from these works can only be, we feel, semi-qualitative when compared on an intrinsic basis.

In some of the remaining cases, the current decay as a function of time is recorded, and this data subjected to a Fourier transform to convert from the time domain to the frequency domain for ease of analysis.

This highlights one of the remaining problems with time domain spectroscopy, namely that uncertainties arise in the frequency limits that can be assigned to the transformed data.

In order to obtain a valid step response by the method described above, the relaxation processes (i.e. the microscopic mechanisms by which ion transport attains its equilibrium value for a given conduction pathway) which occur in the specimen up to time τ_D must initially be in a fully polarised state. This implies that the specimen must be charged for a time $\tau_C > \tau_D$, and this has to be determined for each specimen such that $i(\tau_D) \neq i(\tau_C)$.

The above problem carries on over to the Fourier transform since all the relaxations should have decayed significantly at time τ_D to permit valid assignment of the corresponding frequency $1/\tau_D$. These difficulties have been reviewed in more detail by Hayward et al. [34].

Turning attention now to a.c. measurements, the data obtained is fairly easy to analyse conceptually compared to the difficulties outlined in the previous time domain overview. The responses of similar circuits to a sinusoidal voltage using a.c. theory and a step voltage using Laplace transforms are presented in Appendix I to illustrate the relative simplicity of the frequency domain expression and the need for Fourier transforms to aid interpretation of the time domain data; the time domain current expressions being more insensitive to changes in R and C, thereby hampering attempts to extract the base component values. A further difficulty in component determination is implied by the loss of information in the time domain case, specifically the phase of the current flowing with respect to the applied voltage, having no meaning for an applied step function voltage.

One further point must be made when considering the results obtained from conductivity data, namely the effects associated with high applied potentials.

To illustrate the underlying physical principles, we shall initially consider a linear system. When subjected to a perturbation x(t), the response y(t) may be expressed either in the form of a single nth order differential equation in y:

$$a_0 x(t) + a_1 \frac{d}{dt} x(t) + a_2 \frac{d^2}{dt^2} x(t) + \ldots a_n \frac{d^n}{dt^n} x(t) =$$

$$b_0 y(t) + b_1 \frac{d}{dt} y(t) + \ldots b_n \frac{d^n}{dt^n} y(t) \qquad (2.14)$$

or a set of a first order differential equations.

Therefore, taking probably the simplest drive function,

$$x(t) = A\cos\omega t = \mathrm{Re}(Ae^{j\omega t}),$$

the corresponding response will be of the form

$$y(t) = B\cos(\omega t - \phi) = \mathrm{Re}(Be^{j(\omega t-\phi)}).$$

If we now consider x to be the applied electric field and y the measured electric displacement, then

$$\frac{x(t)}{y(t)} = \varepsilon^*,$$

showing the loss angle δ introduced in the previous section to be equivalent to phase angle ϕ.

The assumed linearity condition is invalidated when the perturbing signal amplitude A becomes too large, since the higher order terms in the Taylor expansion for the change in y for a deviation in x

$$\Delta y = \frac{dy}{dx}\Big|_{x_0,y_0} \cdot \Delta x + \frac{1}{2}\frac{d^2y}{dx^2}\Big|_{x_0,y_0} \cdot \Delta x^2 + \ldots \qquad (2.15)$$

are no longer negligible. It can be shown relatively easily for the cosine variation given above that this deviation leads to the production of higher harmonic responses, the measurement of which leads to other structural information.

As stated in the previous section, the strategy for the analysis of conductivity data is to treat the specimen under test and the measurement cell as an electrical "black box" comprising an unknown parallel and series arrangement of resistors and capacitors.

A variety of theoretical combinations of pure resistors and capacitors are then modelled to the experimental frequency response, and best fit component values determined. Then, by systematic variation of measurement conditions such as electrode area and specimen thickness, the physical representation of each component of the chosen model may be assigned. Finally,

the optimum equivalent circuit may be derived from the continuity of their respective temperature dependences and this used to determine the d.c. conductivity values.

These are the essential requirements of techniques currently supported by the ASTM [35,36].

The kind of data that might be obtained from this kind of experiment is shown schematically in Figure 2.4 to illustrate the most common types of presentation and subsequent interpretations that are in current use. Figures 2.4a and 2.4b are typical examples of dispersion and absorption of a driving force common to many branches of physics (see for example [37]) which deal with relaxation phenomena, but it is Figure 2.4c that appears unique to this particular field. This plot of imaginary vs. real parts of the response is known as a Nyquist or Cole-Cole plot, after the workers who contributed so much to the understanding of dielectric relaxation phenomena in condensed matter.

In the refinement and extension of these principal relaxation models, the library of alternatives that have been presented to parameterise the observed deviations from the fundamental semicircular arcs (some of which are based on the structural interactions of polymeric compounds) meet with various degrees of success [38].

A more revolutionary postulate of a "universal" dielectric response has been presented by Jonscher [39-41], on the basis of the similarities in time and frequency dependent relaxations for a variety of systems, encompassing liquids, glasses and solids. These general similarities are felt to be important, as stated by Cole [42], but the assertion of several different models fitting the same data equally well is felt to be valid here. This serves to introduce a certain cloudiness to the interpretation of data from a more widespread viewpoint, specifically the concept of a single mechanism. However, a combined experimental and theoretical work by Almond et al. [43] has met with considerable success in the interpretation of complex admittance data in terms of Jonscher's universal law.

In the more specialised applied area of glassy and ceramic materials, the work of Syed et al. [44] places the condition of a right-angled intersection of the complex impedance curve

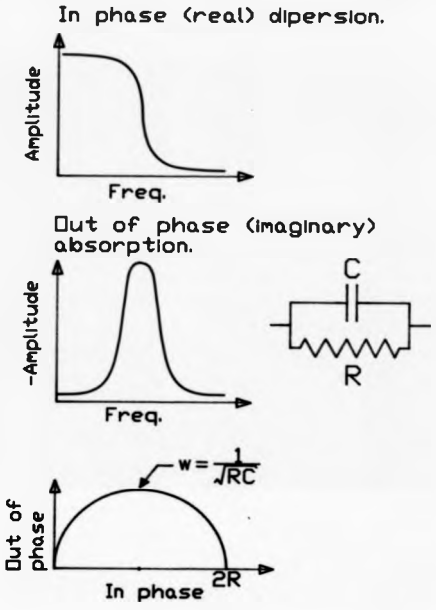

Figure 2.4.
Illustration of the types of graphs used in low frequency electrical measurements by reference to the response of the simple circuit shown.

with the "real" axis at the low and high frequency ends of the spectrum, and therefore some of the more phenomenological relationships previously presented [38] may be discarded in later discussions. Instead, equivalent circuit component values are found either geometrically [45] or numerically [46,47] as stated previously, and if possible any underlying relaxation processes assigned later.

One such case of an additional complication as outlined above in polycrystalline specimens is that of the inter-granular conductivity. Ordinarily the interconnecting glassy phase would provide an inordinately large contribution to the measured conductivity, but in certain circumstances the measured conductance can be comparable and sometimes smaller than the contribution from the higher relative volume fraction of inter-granular interface regions. Even more surprising perhaps are the reports and interpretations of the sensitivity of the overall conductivity to the condition of this interface, the introduction of trace levels of impurities producing an enhancement of a factor of approximately 5 in the measured conductivity [48,49].

This is one example of the additional insight into a problem that can be provided in special cases from this difficult and often time-consuming measurement.

Finally, we can now construct the essential modules necessary for our initial equivalent circuit. Obviously the "d.c." resistance, R_b, its associated capacitance, C_b, and the double layer capacitance C_{dl} are present; C_{dl} being in series with a parallel network of R_b and C_b, with the electronic resistance R_e (hopefully infinite) acting across the specimen part of the circuit.

In anticipation of a polycrystalline specimen, one more segment can be added for the grain boundary contribution, namely a parallel arrangement of R_{gb} and C_{gb}, leading to the final circuit shown in Figure 2.5, which will be the basis for all later analysis in the present work.

2.2.2 Structure

2.2.2.1 Models of Glass Structure

Whilst the structure of polycrystalline materials are now determined on an almost routine basis [50-52], the amorphous equivalent remains somewhat more intractable, both on an

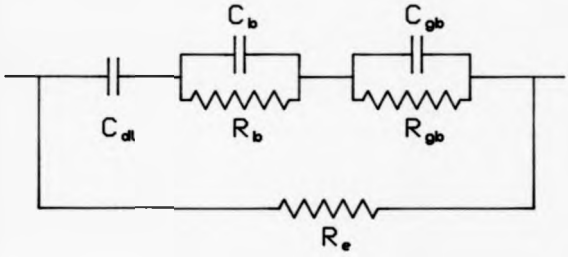

Figure 2.5.

Fundamental equivalent circuit for a polycrystalline material.

experimental and philosophical level. It is not within the scope of this work to present a particularly detailed review of this ever evolving discussion, however the general features of currently accepted models must be summarised to provide a yardstick against which evidence obtained from direct or indirect structure probing techniques can be compared.

Of the models presented to "build" the macroscopic glass from its molecular sub-units, the ones which appear to be the most relevant for this work are the Random Continuous Network (RCN) [53], the microcrystallite adaptation of this by Gaskell [54] and the newly-introduced strained mixed cluster model of Goodman [55]. The other corner-stone of the modelling of amorphous solids, the Dense Random Packing of Hard Spheres (DRPHS) is of relevance only to amorphous metallic alloys [56].

As can be seen from the work of Gaskell and Goodman, the trend in modern thinking appears to be towards the visualisation of an amorphous solid composed of micro crystallites, which for additional confirmation, are also reported to have been observed in an ultra high resolution transmission electron microscope [57].

Let us concern ourselves with the local environments of atoms within the glass. The compounds which are combined to form glasses can be distinguished on an operational basis to fit into three categories: glass formers, modifiers and intermediates.

Glass formers are those compounds which by themselves form glasses, and are an essential constituent in more complex mixtures to retain the "amorphous state". These are (for oxide-based glasses) SiO_2, B_2O_3, P_2O_5 and GeO_2. The non-oxide based or chalcogenide glasses exhibit similar behaviour to the oxide glasses and are discussed in more detail elsewhere [58]. For the purposes of illustration of the structural implications of the final two categories, SiO_2 is usually chosen as the typical glass former, due to the vast amount of corroborating evidence available from work already performed and its relative structural simplicity compared to B_2O_3 and P_2O_5. We shall also follow this strategy for the time being, and return to the more anomalous behaviour of B_2O_3 shortly.

The effects of modifier oxides, such as Li_2O, Na_2O, MgO and CaO, and intermediate oxides such as PbO and Al_2O_3 can be understood by reference to Figure 2.6. Figure 2.6a shows a regular four-coordinated, two dimensional network (for clarity) which may be thought of as vitreous silica, with each silicon atom joined to four others via an oxygen atom. Several molecules of modifier (Na_2O) are added to this "glass" in Figure 2.6b, thus breaking some of the Si-O-Si bonds to create a more non-bridging network by the mechanism illustrated at the side. The ramifications of this action may be observed relatively easily experimentally, in that the viscosity at a given temperature (which may be visualised as a shearing of bonds in a fluid) decreases with increasing modifier content since there are now fewer bonds to "break". This is further reflected in other properties which may be directly linked to the influence of chemical bonding, e.g. thermal expansion, T_g (the glass transition, which will be discussed later), and infra-red absorption bands [22].

Ultimately, as one might imagine, at higher modifier concentrations sufficient bonds will be broken to prevent a network from being formed, and so it will not be theoretically possible to form a glass. For example, 1 molecule of Na_2O creates 2 non- bridging oxygens (nbos) from Figure 2.6b, and so ½ mol of Na_2O added to 1 mol of SiO_2 would create a two-dimensional network on a statistical level, since the majority of Si atoms would then have three bridging oxygens (bos). The addition of 1 mol of Na_2O would therefore form a one dimensional network of Si-O-Si chains, which would presumably tangle on cooling to form a glass, and as such, it is not possible to form silicate glasses at significantly higher concentrations than 50 mol % modifier on the basis of this model. This is observed in practice for the "simpler" modifier oxides cited above [12].

Taking the modified "glass" in Figure 2.6b and adding an intermediate oxide to it strengthens the network again by provision of extra bonds between the multivalent atoms responsible for the network in the first place, as shown in Figure 2.6c. This is also verified experimentally by a return towards the behaviour of vitreous silica of the properties previously employed to illustrate the effects of modifier oxide addition.

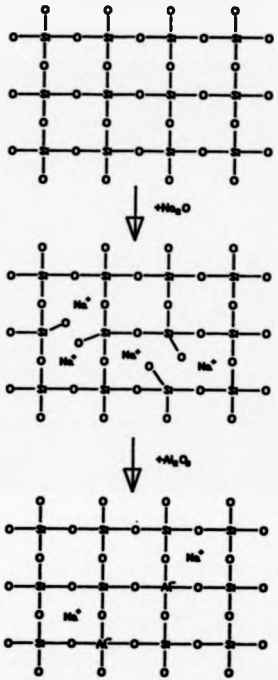

Figure 2.6.
Effect of modifier addition upon the structure of a silicate glass. (Drawn as a regular 2D array for clarity.)

This somewhat simplistic description is complicated by interpretation of some experimental anomalies, namely that in mixed modified silicates, e.g. "invert" glasses, the glass forming region can be observed up to a total 60% modifier [12], and in the binary PbO-SiO_2 system, glasses up to ~ 90 mol % PbO have been reported [59] but do not appear to be reproducible [60]. The explanation of this second observation is based on the interpretation of the varying role of PbO in the network. Although the existence of glasses with lead as the sole central atom have not been universally accepted, it is widely believed that the role of lead changes from a modifier at low concentrations to an intermediate in materials having a higher lead content. This has been related to a change of the bonding of lead in the network, from ionic to covalent, for both silicate [61] and borate [62,63] glasses.

For the sake of completeness, we include an additional category in the set of materials available for glass formation, namely conditional glass formers. These are compounds which form glasses when combined with certain other non-glass forming oxides, but which cannot be obtained in a glassy condition by themselves. Typical examples include TeO_2, Al_2O_3 and Bi_2O_3 (see for example the CaO-Al_2O_3 and SrO-Al_2O_3 systems [64]).

Consideration of the more relevant case, namely boric oxide-based glasses, leads to additional complications. The ground state electronic structure of $^{11}_{5}B$ is $1s^2 2s^2 2p^1$. When energy is injected into the atom (e.g. during the formation of chemical bonds, provided by the bond energy), the electronic structure reflects the excited state of the atom, changing from

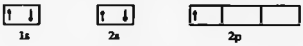

to

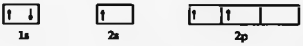

$3 \times sp^2$

which may then form $3 \times sp^2$ hybrid orbitals as indicated above. Furthermore, the empty sp^2 hybrid orbital can then accept a dative bond, the modified orbitals then becoming $4 \times sp^3$. This

generally occurs when additional oxygen, in the form of a modifier, is introduced into the glass, forming a mixture of 3- and 4-coordinated boron atoms in the network via a lone pair from the oxygen 2p shell *.

The revised situation is shown schematically in Figure 2.7. In a similar manner to that of Figure 2.6, Figure 2.7a represents the basic B_2O_3 network, with Figure 2.7b showing the effects of low modifier concentrations, and Figure 2.7c the 'structural reversal' upon subsequent intermediate addition.

The direct structural techniques available for confirmation of this concept comprise X-ray and neutron diffraction, and nuclear magnetic resonance (NMR).

2.2.2.2 Direct Methods of Structure Determination

X-ray diffraction work on borate-based glasses has been used with the random network model previously presented to study the structure of Na_2O-B_2O_3 glasses, as a function of Na_2O content [65]. Neutron diffraction merely provides an alternative view of the same problem, namely the interpretation of the broad bands with increasing 2θ (where θ is the angle between specimen and incident radiation) from the determination and analysis of the radial and pair distribution functions.

This behaviour can be qualitatively understood by considering the micro crystallite model once again in a generalised re-statement of the Porai-Koshits model of glass structure [66]. The broadening of an X-ray peak obtained for a crystalline specimen is dependent upon the spread of incident X-ray wavelengths (a consequence of the uncertainty principle), thermal excitations of the atoms within the crystal under examination, crystal defects (stress broadening, for example), and the physical size of the crystallites.

---

*The electron promotion illustrated above forms a precursory step in bond hybridisation. The energy required to perform this is supplied by the dative bond formed by the 'additional' oxygen atom.

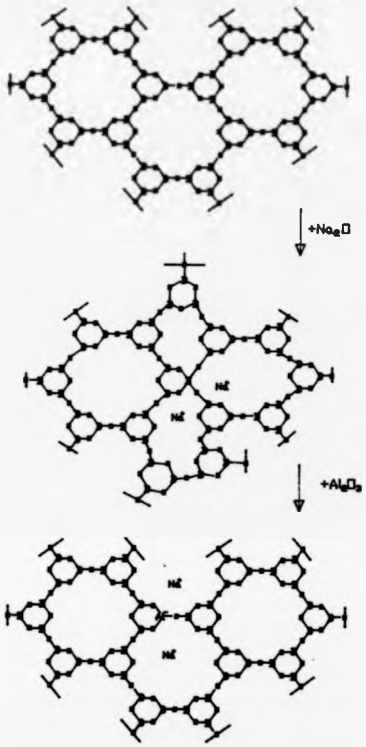

Figure 2.7.

Effect of modifier addition upon the structure of a borate glass.

As the broadening increases, then peak intensity diminishes, leaving the total scattered intensity from a given specimen essentially constant, depending upon the measurement conditions. The effects of the last two mechanisms can be quantified from measurements of the peak width, within certain limitations.

For crystallite sizes < 0.1 μm the peak full width at half maximum (FWHM) can be employed to determine mean crystallite sizes [67,68]. In the limit, the peaks can be visualised as becoming sufficiently small and broad to no longer be resolvable, and the result is an X-ray amorphous material. This normally constitutes < 1 ppm by volume of crystal phase, which is the common practical lower limit of verification of the glassy state, in stark contrast to an early attempt at the definition of a glass [12].

The stumbling block of the above argument is in the definition of a crystallite in the lower limit, which lead to the eventual retraction of the Porai-Koshits model. The author feels that once this theoretical debate has subsided, the simplistic visualisation presented above may then be more meaningfully interpreted.

The principal difference between information derived from these two scattering techniques arises from the relative scattering factors of the constituent elements of the material under investigation. For X-rays, the most powerful scatterer is the oxygen atom, whereas for neutrons, the $^{11}_{5}B$ nucleus dominates. However, isotopically enriched boron must be used in neutron diffraction experiments, since the absorption from $^{10}_{5}B$, although only ~ 20% abundant in nature, can totally destroy the signal [69]. Even so, isotopic enrichment is not as selective for boron as with other elements, with typical purities reaching only 95% $^{11}_{5}B$.

More useful structural insight is obtained from determination of the inter-atomic distances within the corresponding crystalline phase, and then linking this to the comparative response of glass and crystal in indirect structural measurement techniques such as infra-red spectroscopy. Much of this work was pioneered by Krogh-Moe [70], and has since been continued by other workers (see for example [71,72]).

NMR is able to examine both glassy and crystalline samples equally well, since it is dependent on the local environment of the atomic species under scrutiny [73]. Initial experiments presented in the classic paper by Bray and O'Keefe [74], shows a dependence of N_4, the fractional concentration of 4-coordinated boron atoms, with modifier concentration of the form displayed in Figure 2.8. This has since been repeated and re-analysed (see for example [75,76]) with slightly different trends appearing at low modifier contents, presumably due to the hygroscopic nature of B_2O_3, which in turn presents a further experimental difficulty [77]. As can be seen from the figure, a maximum of $N_4 \approx 0.4$ exists at ~ 30 mol % modifier, the decrease with increasing modifier content being attributed to the increased formation of non-bridging oxygens [78]. This was in disagreement with the popular hypotheses presented for the concentration dependence of N_4 [79], which over the years, has enjoyed considerable attention. Examination of Figure 2.7b shows that 1 mole of a monovalent cation oxide will produce 2 moles of 4-coordinated borons. Therefore for x moles of added modifier in a glass of composition $xR_2O.(1\text{-}x)B_2O_3$, the number of 4-coordinated boron atoms will be 2x. The total number of boron atoms is 2(1-x), thus giving $N_4 = x/(1\text{-}x)$, which is shown as the dashed line in Figure 2.8.

A more recent model, based on a statistical mechanical re-analysis of the respective energies of the boron-oxygen "building blocks", presented by Bray et al. [80], appears to fit the experimental data better to higher concentrations, and is shown as the solid curve in Figure 2.8 for comparison.

The more indirect structural investigation techniques, however, whilst possessing sensitivities to the (amorphous or crystalline) state of the test material somewhere between NMR and diffraction studies, examine in the most part, the vibrational response of the material comprising an "intermediate range order", between the local atomic environment of NMR and the "lattice" periodicity of X-ray and neutron diffraction. Therefore, interpretation of this data is normally made in terms of identifiable structural groupings brought over from X-ray structure determinations of crystalline borate compounds, which are shown in Figure 2.9.

Figure 2.8. Variation of number of 4-coordinated boron atoms with modifier content in borate glasses of general formula $xR_2O.(1-x)B_2O_3$.

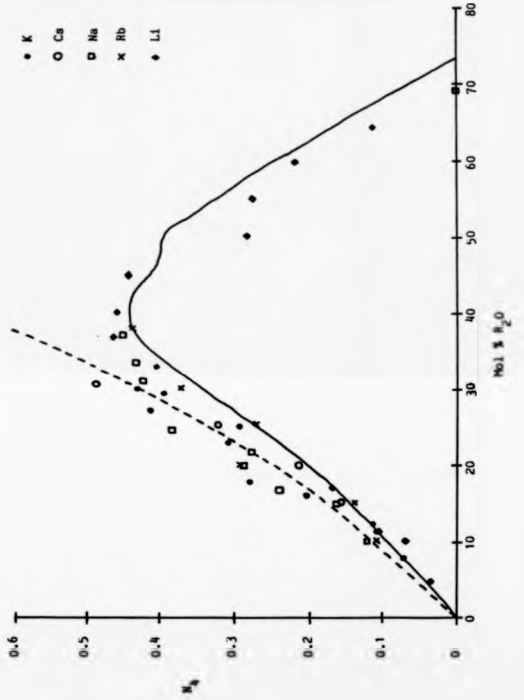

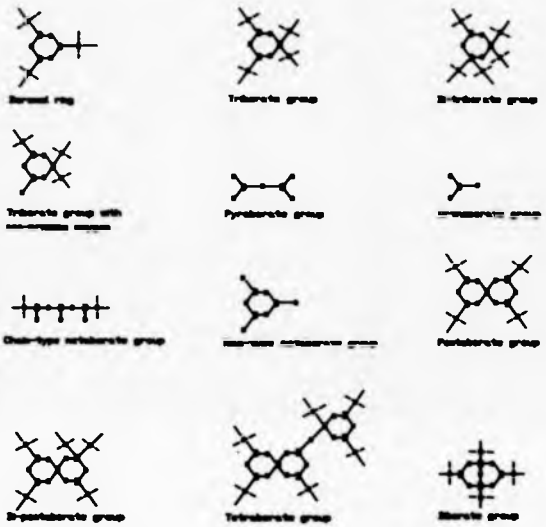

Figure 2.9.

Structure and nomenclature of groups found in borate glasses.

2.2.2.3 Indirect Structure Determination Methods

2.2.2.3.1 Infra-red and Raman spectroscopy

Probably the technique best suited to begin this particular section is that of infra-red spectroscopy, both from the viewpoint of experimental simplicity and availability, and theoretical interpretation on a microscopic level [81]. At infra-red frequencies, the interactions between the test material and the incident radiation that are most commonly excited are those pertaining to atomic vibrations. We may visualise the subsequent absorption (if any) by extrapolation from the oscillating behaviour of the simplest case, namely a diatomic molecule with constituent masses m_1 and m_2, and coupling constant k. The resonant frequency is expressed as

$$\nu = \frac{1}{2\pi}\sqrt{\frac{k}{\mu}} \qquad (2.15)$$

where μ is the reduced mass $= \frac{m_1 m_2}{m_1 + m_2}$ from a classical mechanics formalism [37].

This concept is established with far more rigour in a treatment of the simple harmonic oscillator by Wong and Angell [11]. One might be inclined to imagine that a measure of the force constants of, for example, some of the constituent groups displayed in Figure 2.9 may be obtained from this kind of measurement by linking the (resonant) absorption frequencies to the masses of the constituent atoms in the specimen. However, this elementary explanation is complicated in reality by three problems, all of which are magnified in the investigation of glassy materials.

1. Principally, a large crystal exhibits a rapid increase in the number of normal vibrational modes from that of a diatomic molecule, due to the added possibilities of transverse, rotational and higher cooperative group motions, for example the expansion and contraction of a boroxol ring, known as "breathing" [82].

2. Moreover, due to the changeable local environments from the inherent lack of long

range order, the sharp peaks that might be expected are broadened quite considerably. This effect diminishes with the increased symmetry produced upon crystallization, but is not completely eliminated (see for example [79] and section 3.3.2.1).

3. This localised distortion in the amorphous state also manifests itself in one further aspect of infra-red spectroscopy previously unmentioned here; that of "dipolar selection". To return to a simple case, consider two of the longitudinal normal modes of a linear triatomic molecule (say CO_2). In the first type of vibration, the two oxygen atoms move in phase with respect to the carbon atom, giving a zero dipole moment, which is therefore unable to interact with electromagnetic radiation and give an infra-red absorption band. In the second type of vibration, the respective carbon-oxygen bonds are stretched and compressed, thereby exhibiting no symmetry and thus a periodic variation of the dipole moment at the (resonant) oscillation frequency, and hence an infra-red absorption.

Vibrations associated with a dipole moment are nominally defined as infra-red active, and those with a zero dipole variation as infra-red inactive. However, this latter class of vibrations may still be probed in the infra-red, as we shall see shortly. The effect of the random atomic arrangements characteristic of an amorphous material is to once again distort the localized electric fields and produce partial dipole moments, thereby allowing some "forbidden" absorption.

This leads us to the two types of infra-red spectroscopy most commonly used in the investigation of molecular vibrations, infra-red absorption and Raman scattering. The difference between the two techniques is that for infra-red absorptions, a frequency scan of the incident light is used to determine the absorption bands. Raman, however, is based upon the generation of electromagnetic radiation in the molecules by the electromagnetic field of the incident radiation, thereby requiring a single frequency, high intensity source, since these additional lines are far weaker than the concomitant Rayleigh scattering. The phenomenological description of this effect may be given with reference to Figure 2.10.

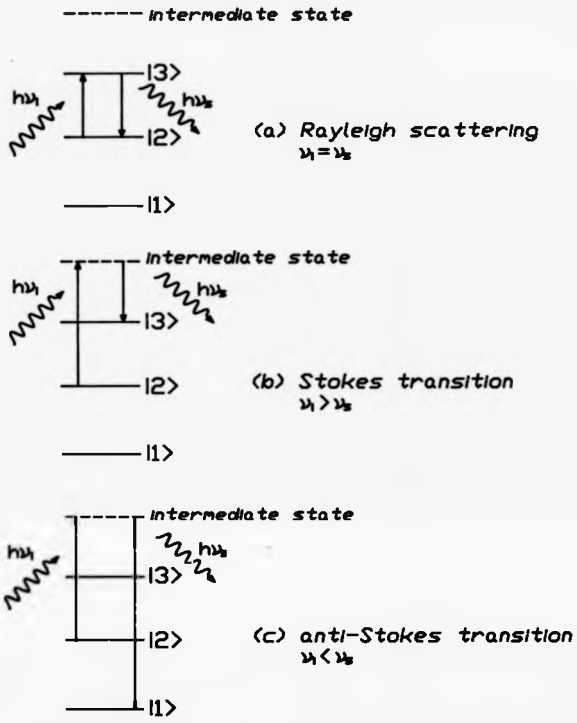

Figure 2.10.
Energy level diagrams for
infra-red and Raman spectroscopy

An incident photon of frequency ν_i is absorbed into a virtual state within the molecule and must then decay to one of three stationary states in the time dictated by the Heisenberg uncertainty principle $\Delta E \Delta t = h$ upon discovery that the molecule has no energy levels:

1. Elastically, recovering its initial energy $h\nu_i$ (Figure 2.10a).
2. A higher energy state, emitting $h\nu_{out}$ and leaving energy $h\nu_k$ (Stokes lines - Figure 2.10b).
3. A lower energy state, emitting $h\nu'_{out}$ and depriving the molecule of energy $h\nu'_k$ (anti-Stokes lines - Figure 2.10c)

Because of the cause of the Raman effect, it can be shown that Raman transitions will only occur where there is an associated change in the polarisation of the scattered light [83]. This generally occurs where there are no net dipole moments, and as such, is complementary to infra-red, i.e. infra-red inactive is Raman active.

Early ground work in the spectroscopic investigation of glassy materials placed great emphasis upon the systematic assignment of characteristic absorption bands to the previously identified structural groupings, with a surprising level of success, as shown by the summary in Tables 3.3 and 3.4. However attempts at more detailed assignments began to show the shortcomings of this strategy.

An intensive work programme was undertaken to measure the relative concentrations of 3- and 4-coordinated boron atoms possessing both double and single boron-oxygen bonds in a variety of glasses. The purpose of this was presumably to correlate data acquired from infra-red, NMR and X-ray spectroscopic methods [84]. Unfortunately, the attempt failed because of the previously-stated limitations of optical techniques, presented as reasons for this misfortune. Further limitations, highlighted by a combined argument based on recent experimental work by Konijnendijk [72], and a theoretical work by Brü [82], are that ring-based structures (boroxol to diborate) are not distinguishable by examination of their respective infra-red vibrational spectra.

However, infra-red spectroscopy appears sufficiently sensitive to indicate the presence of bond distortion within the glass network from different alkali ions added to the glass. This is

indicated in Figure 2.11, which shows infra-red spectra for a variety of isomorphic monovalent oxide borate glasses. The network structures indicated by the system responses are essentially the same, but closer examination reveals a number of subtle differences. Previous publications have not interpreted these variations in this manner. The "absolute" metal ion vibrations within the lattice "cage" are thought to be most visible at lower wavenumbers (the spectroscopic unit of frequency = $1/\lambda$) following a definitive piece of work by Exarhos and Reisen [85] that does not appear to have been more quantitatively investigated, hence the above presumption of lattice distortion by Newton's third law.

Other evidence of this alkali ion perturbation of the vibrational spectrum which is of questionable relevance here can be found from the X-ray spectra of potassium silicate glasses [86]. The essence of the argument is presented below. If an increased number of potassium ions are present in the structure, then one may imagine that they will enter "holes" in the network, which would then be forced to expand, thereby manifesting itself as a shift of the maxima in the RDF (Radial Distribution Function) towards greater distances with increasing potassium concentration. This is not observed in practice, nor does the measured inter-potassium ion distance decrease with increasing concentration as would be expected for a single structure RCN model. Therefore two intermingled structures were assumed in the initial work; one of the "pure" oxide, and the other comprising a potassium-rich phase. This was further validated from the "difference" radial distribution curves obtained from the modified glasses and pure SiO_2. The bands were seen to have the same general shape in all cases, but sharpening with higher modifier contents.

The above concept is accommodated in the micro-crystallite model by assuming two (or more) different types of "crystallite". Hence the observation of the proposed metal ion distortion could be magnified by the "concentration" of surrounding metal ions in the second "phase".

This network distortion argument is equally applicable to Raman spectroscopy.

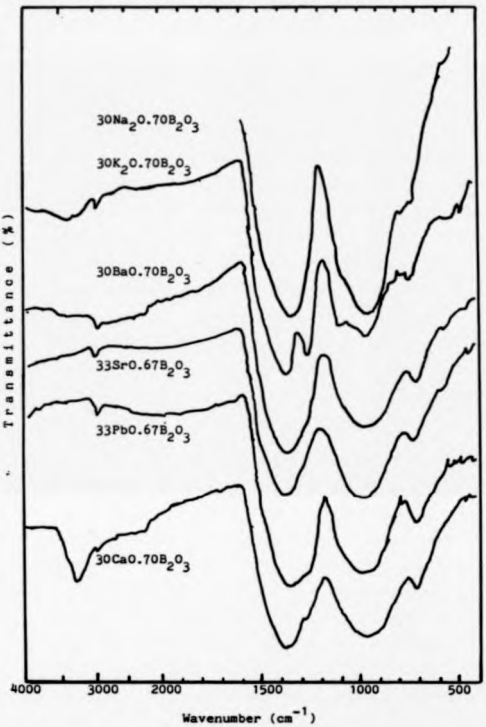

Figure 2.11. Infra-red spectra for a series of metal oxide-borate glasses having the same modifier content.

2.2.2.3.2 Coefficient of linear thermal expansion

The microscopic interpretation of thermal expansion measurements can best be undertaken by reference to the potential well diagram in Figure 2.12. Towards absolute zero, an atom will 'sit' at the bottom of its potential well and be fixed in its crystallographic position. Upon increasing the lattice energy to give rise to a temperature T, the atom may now oscillate in this well up to an energy kT (where k is the Boltzmann constant = 1.380×10^{-23} JK^{-1}) as shown in the diagram, thereby increasing (for the majority of cases) its mean displacement from the given origin due to the asymmetry of the well, which is reflected in a positive measured thermal expansion coefficient. Some measurements of negative expansion coefficients have been reported in glasses (for example in aluminosilicate systems [87]) and in other materials [88] which appear contradictory to this argument, and are attributable to hinge-like vibration modes of the O-Si-O bridges in the former instance. Therefore, in principle, information about the shape of the localised atomic potential wells may be obtained.

From the above description, it is not surprising to learn that the measured expansion coefficient, the associated T_g value (to be discussed in the next section) and the dilatometric softening point M_g (the temperature at which viscous flow exactly matches the thermal expansion and so no net increase in length is observed in a vertical measurement apparatus) are strongly dependent upon specimen preparation and measurement conditions. These comprise the thermal history (the temperatures and associated heating/cooling rates employed in the attainment of these temperatures to which the specimen has previously been subjected) of the specimen [22] and the heating/cooling rates of the measurement [89], since this is a measure of the net departure from dynamic equilibrium and the ability of the glass structure to accommodate it. Correlation of thermal expansion data with thermal history does not seem possible on a quantitative basis, however, since the strain introduced to the bonds will undoubtedly vary throughout the specimen in both a spatial and temporal manner in different amounts on each successive heat treatment.

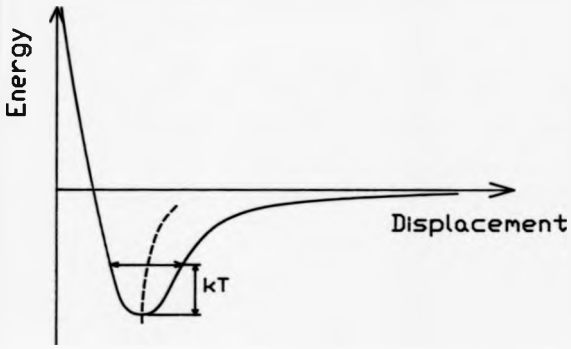

Figure 2.12.
Simple view of thermal expansion. As the temperature increases, the centre of oscillation moves to increse interatomic separation.

It should therefore be common practice to state the full measurement conditions and thermal histories in all reports of thermal expansion data.

2.2.2.3.3 Thermal properties

The thermal response characteristics of glasses can be processed to yield fundamental kinetic properties which are useful both from a quality control viewpoint in the commercial production of an article and as a guideline for proposed heat treatment schedules in the laboratory. The most common methods of undertaking these measurements are differential thermal analysis (D.T.A.) and differential scanning calorimetry (D.S.C.). The primary differences between these two techniques are in their respective sensitivities and in the form of the output data.

Formally, the physical basis of any thermal evaluation is to measure the temperature of the material under test when contained in a thermal reservoir of high thermal mass (heat capacity), and comparing it to that obtained from a standard material possessing similar thermal constants to those of the test material (preferably one which does not exhibit a phase transition in the temperature range of current interest) under similar conditions. The ensuing analysis normally produces one or more thermal "constants", characteristic of the material and also measurement conditions e.g. the presence of water. These parameters are principally specific heat capacity, thermal conductivity and thermal diffusivity, together with the enthalpies of any phase changes. The interpretation of these quantities are the amount of heat energy absorbed by a substance for a given temperature change, the steady state transference of heat energy, and the rate at which a material will transfer energy under dynamic conditions respectively. These thermal constants reflect certain responses of the D.T.A. curve. For instance, a mismatch of the thermal diffusivities of sample and reference will give rise to a systematic baseline drift, a phenomenon which is the cause of considerable worry to some experimentalists. Similarly, a constant offset is measured for discrepancies in specific heat, mass and volume of the two materials. Therefore a zero baseline should be considered as a special case only. The reader is referred elsewhere for a more in-depth discussion of these observations [90].

In the case of a phase change though, a peak is measured with an area directly related to the enthalpy of the change and a maximum at some characteristic transformation temperature, before returning to the original baseline trend shortly afterwards.

If the specimen has a higher temperature than that of the reference, then energy is being rejected, indicating an ordering to be taking place by losing free energy, which may be indicative of, say, crystallisation. The converse is also true, representing for example, the melting of a given crystal phase. A further example of this latter condition, characteristic of glasses, is that of the glass transition.

Imagine an experiment where some macroscopic property, say the volume (of equal validity are other thermodynamic properties such as enthalpy and entropy, or viscosity and thermal expansion [91], or ionic conductivity [92]) of a liquid is being determined as the liquid is cooled. The results are depicted schematically in Figure 2.13. Initially, the parameter will decrease linearly along line ab until the liquidus temperature T_f is attained, whereupon a discontinuous decrease (increase for viscosity and ionic conductivity) characteristic of crystallisation will occur (along bc), followed by a new temperature dependence associated with the new crystal phase upon subsequent cooling, along line cd. The effect of crystallisation may be postponed to a lower temperature if the liquid supercools. A third option is available for a glass cooled from the melt: here liquid-like behaviour is observed down to some particular temperature T_g (below the liquidus), whereupon a second-order discontinuity of the volume-temperature curve occurs at e, followed by a new volume-temperature dependence along line ef. (This is equally applicable to the other properties listed above). This discontinuity is known as the glass transition, and the associated mean temperature as the glass transition temperature T_g. Moreover, if the glass is held at temperature T, the volume will decrease gradually to point g extrapolating from the liquid-like cooling behaviour, reinforcing the concept of glass as a supercooled liquid.

Strictly speaking, from examination of the representative behaviour shown in Figure 2.13, T_g values should be given as a range to indicate more explicitly the uncertainty associated with it. Numerous attempts have been made to uniquely interpret this phenomenon on a

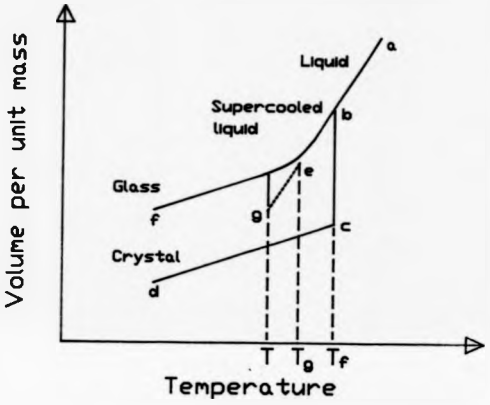

Figure 2.13.
The relationship between the liquid, solid and glassy states.

structural basis [93], but it is not within the scope of this work to discuss them critically. Needless to say, a very general (and thermodynamically inaccurate) inference might be that the glass transition represents a "partial crystallisation" and reorganisation of the melt, from the viewpoint of the microcrystallite model. For more stable glasses (i.e. ones which do not crystallise easily, e.g. window glass) the observation of T_g should, and in fact does, become more difficult due to a reduction in the required reorganisation of the structure. It is postulated here that in the limit of enhanced glass stability, T_g will be "invisible" for precisely the kind of material that such a measurement should be ideally suited to i.e. the existence of Tg appears to imply a non-stable structure at a given temperature, a concept which may be readily understood by more careful examination of Figure 2.13. If the glassy condition (curve abef) is favoured, and the material is held at some arbitrary temperature T_o, then the glassy value will slowly diminish to equalise with the corresponding extrapolated supercooled liquid value, as shown by the dashed lines on Figure 2.13. This demonstrates that the glass is metastable with respect to the supercooled liquid structure.

Consider now a more stable glass: the reorganisation necessary to transform from the liquid into the "glass" will now be much smaller, such that this material may, in the limit, be indeed considered not to exhibit the glass transition. If the most recent attempt at the definition of a glass, namely, "Glass is an X-ray amorphous material that exhibits the glass transition, this being defined as that phenomenon in which a solid amorphous phase exhibits with changing temperature a more or less sudden change in the derivative thermodynamic properties, such as heat capacity and expansion coefficient, from solid-like to liquid-like values" [11], is now examined, we are faced with one of two problems. Either the stable structure is a glass, in which case the definition is in conflict with the above argument, or the structure is indeed a supercooled liquid, thereby requiring a more precise distinction between a glass and a supercooled liquid.

Now, having measured the thermal behaviour of the system which may be represented in the form of a ΔT vs. T graph similar in character to Figure 2.13, the desire for more detailed information becomes apparent: for example, the enthalpy of crystallisation, which could be

related to nucleation and crystallisation kinetics in the production of a given (commercial) article. It is at this time that the differences between D.T.A. and D.S.C. become apparent. Whilst D.T.A. can be used to obtain semi-quantitative thermal parameters, D.S.C. can be calibrated absolutely.

The D.T.A. apparatus generally employed in this type of work is the commercial equivalent of that originally proposed by Saraschu [90], and like all conventional D.T.A. equipment, uses a single differential thermocouple between specimen and reference to give an optimum accuracy of about 5%.

For D.S.C., however, there are two main principles of measurement: the first is to measure the heat flux of a given volume (the specimen/reference sample holders) in a thermal reservoir, and the second is to measure the power which must be supplied to either the test material or standard to balance the temperature changes obtained from a conventional D.T.A. technique. Due to the experimental facilities currently available, it is to the former that we principally direct attention.

This consists of a regular systematic array of several hundred similar thermocouples connected together in series to form a thermopile. Because of the very nature of this arrangement, the e.m.f. generated from this thermopile is proportional to the total amount of heat exchanged between the specimen holder and the surrounding heat bath. The specimen and reference thermopiles must therefore be carefully matched during construction and the sensitivity and response times of the output signal ultimately equalised by the use of electrical and thermal shunts. Therefore, by evaluation of the relationship between the signal amplitude and physical power dissipated, calorimetric determination of the thermal constants of the unknown sample may be undertaken. This calibration is either performed by the Joule effect (placing a small heater in the sample holder), the Peltier effect (using some of the thermocouples in the thermopile independently of the detection system), or by measurement of heats of fusion of a standard material.

The alternative approach to D.S.C. is to introduce furnace elements into the (thermally well isolated) sample holders which are then used to increase the measurement temperature and compensate for the energy differences previously described.

2.2.2.3.4 Viscosity

In a general forming process in glass technology, it is often desirable to use a glass system where virtually constant flow conditions exist over a fairly wide temperature range, just as a low thermal expansion coefficient is useful to reduce the probability of cracking during cooling due to differential contraction. The former condition is satisfied where a low viscosity activation energy is observed i.e. the slope of the ln(viscosity)-temperature curve is relatively flat. This is also particularly useful after the formation process during annealing, where strains introduced by uneven cooling during forming are relieved by heating and holding the glass at a temperature where distortion of the article is not apparent, and cooling slowly thereafter to ensure the strains are not reintroduced.

Thus the need for a viscosity-temperature curve becomes apparent to eliminate many time (and money) consuming trials, and as might now be expected in this section, the basis of viscosity lies on a partially accessible fundamental microscopic understanding of the structure in general. Elementary undergraduate texts covering macrophysics [94] and kinetic theory [95] interpret and analyse viscosity on the premise of atomic layers sliding over each other under the influence of a shear force, which also appears equally applicable in more comprehensive theoretical descriptions requiring the input of a viscosity-based argument.

The implications to glass structure, therefore, are essentially trivial, namely that of providing a "feel" of the strength of individual bonds to the aforementioned shear force, or more simply, the resistance of the now more fluid "network" at elevated temperatures. This in turn provides insight from which more definitive experiments to investigate a given property may be contrived.

From section 2.2.2.3.3, viscosity is a material property which exhibits the glass transition; corresponding values being typically in the range 10^{11} - 10^{12} Poise for all the systems measured

[96], thereby implying that subtle structural complexities must be present in any physical model of the glass transition [55,57].

2.2.2.3.5 Density

The final property to be discussed in this section, density, is arguably one of the simplest to measure and one of the most informative for the effort required. From a knowledge of the glass composition (formula weight F), the molar volume v (a macroscopic measure of the efficiency of atomic packing) can be calculated from the density ρ, since

$$v = \frac{F}{\rho}. \qquad (2.17)$$

from the definition of density.

In the particular case of borate-based glasses, as with other hygroscopic materials, care must be taken to avoid contact with water, both with the glass itself, and by the choice of an immiscible immersion fluid such as liquid paraffin (nujol) or glycerol. This latter condition has implicitly assumed that picnometry [94] is employed due to its ease and superior accuracy.

2.2.2.4 The Structure of Borate Glasses

Having now examined the various measurements that can be employed to determine the structure of glasses, we now briefly review the results obtained, their conflicting inferences, and the models presented to explain them.

Historically, probably the first model presented was that by Biscoe and Warren [97], to explain the observed minimum in the graph of thermal expansion coefficient vs. modifier oxide concentration, at ~ 17 mol % modifier as shown in Figure 2.14 +.

+ Fluctuations in the position of this minimum can be observed by consulting the literature, but it is believed by the author that this may be attributable in part, if not in full, to the preparation and measurement conditions (see 2.2.2.3.2).

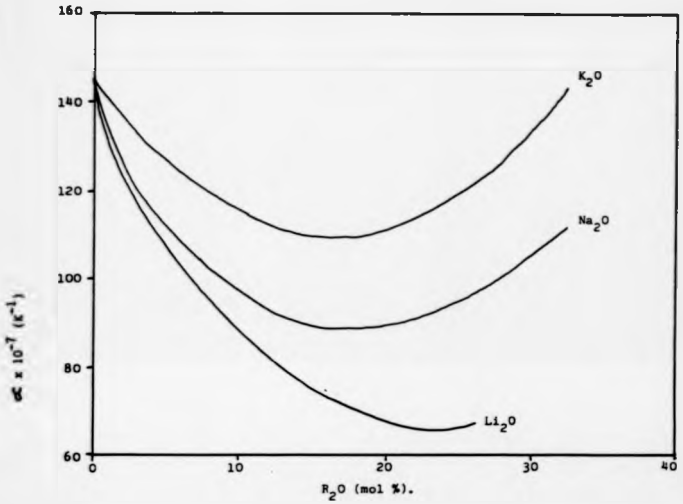

Figure 2.14. Variation of linear thermal expansion coefficient with modifier content. After Rawson [22].

This model postulated the structure of glassy B_2O_3 to be a random arrangement BO_3 triangles, with added modifier forming BO_4 tetrahedra, thereby increasing the packing densities in the network and thereby decreasing the thermal expansion coefficient. This process was thought to occur up to ~ 13 mol % whereupon non-bridging oxygens would be formed to weaken the network and again increase the thermal expansion coefficient.

The next major contribution was presented by Abe [98], who proposed a model with a series of arbitrary "selection rules", the principal one being that two 4-coordinated boron atoms (B4) would preferentially avoid each other. This implies that tetrahedra are only formed to the $R_2O.5B_2O_3$ composition, since beyond this "forbidden" B4-B4 linkages would be necessary. This led to the conclusion that N_4 should remain constant at higher modifier concentrations.

Other, more controversial models were also presented of borate glass structure. Perhaps the most notable of these was an early work by Grojtheim and Krogh-Moe [99], where boric oxide itself was postulated to comprise boron atoms 4-fold coordinated by oxygen. Moreover, this four-fold coordination was postulated to revert to 3-fold upon modifier oxide additions.

Experimental evidence was at that time fairly unreliable and so no formative ideas regarding the validity of one or more models or concepts could be obtained. It was in the early 1960's that the definitive experiment cited previously (by Bray and O'Keefe [74]) was eventually performed with the required result. The conclusions of this experiment were far-reaching: the N.M.R. evidence now showed a consistent increase in N_4 with modifier concentration from ≈ 0 at $x = 0$ to ≈ 0.5 at $x \approx 0.4$ for a variety of cation species, thereby sweeping aside many of these previous models. However, a more puzzling question was now posed: what structural effects are responsible for the observed concentration minima in thermal expansion and T_g at ~ 17 mol % modifier, which also appear to correspond to concentration maxima in other properties such as viscosity.

The peculiar behaviour outlined above is now well known as the boric oxide anomaly. A variety of models to explain this more detailed behaviour have since been presented, ranging

from quantitative theories relying on empirically-determined constants for their agreement [100], to the more widely-accepted view of molecular groups by Krogh-Moe [101] (see Figure 2.9). An earlier publication, which contained extensive analyses of the models favourable at that time and reports of interesting thermal analogies between systems [102] does not appear to have been well-received in its original form. The reader is directed elsewhere [103] for a more detailed review of these models.

One further series of observations are presented in Appendix 2 which may be able to link the NMR data to the more obtuse macroscopic anomalies occurring at ~ 17 mol % modifier.

It is interesting to note, perhaps, that no models have yet been presented for borate glasses using the micro-crystallite model. The alkali borate glasses, however, appear to exhibit similar compositional trends to those of the crystal. If the argument for the dismissal of the micro-crystallite model is valid, then one should exercise extreme care when comparing "long range" (of the order of the diameter of a micro-crystallite) interactions of structural groups between glassy and crystalline compounds.

2.2.2.5 The Effect of Halide Addition

The structural implications of halogen introduction to a borate glass network introduce an additional complication to the preceding discussion: the majority of workers in this field seem to be of the opinion that the halide resides interstitially i.e. is not directly bonded, within the network, from an abundant supply of experimental evidence, derived for the most part from NMR studies [75], where the variation of N_4 vs R ($[R_2O]/[B_2O_3]$) was not seen to change halide addition. However, several other pieces of work imply the existence of B-X (X = halogen) bonding to some extent, albeit with some qualifications.

Chemically, there are two criteria to be satisfied initially, namely the sizes and electronegativities of the halides must be compatible with the existing borate network, i.e. will the halogen fit into the local environment surrounding, and bond with, a boron atom? Values of ionic radii and electronegativities for the halogens are shown in Table 2.2, with oxygen included

Table 2.2 Ionic Radii and Electronegativities for the Halogens and Oxygen

Ion	Ionic Radius (Å)	Electronegativity
F^-	1.33	4.0
Cl^-	1.81	3.0
Br^-	1.96	2.8
I^-	2.16	2.5
O^{2-}	1.32	3.5

for comparison purposes. As can be seen from this simplistic chemical viewpoint, there is no reason whatsoever why B-X bonding cannot take place. The stumbling block would appear to be in the thermodynamics of the reaction itself, for which reported data is not of sufficient applicability to perform suitable calculations.

In glass science itself, only three intrinsically diverse pieces of work have been found that look favourably upon this structure modification, for fluoride, chloride and general halide-containing glasses respectively. All report the difficulty of halide retention during melting, which seems to be exacerbated by the presence of water [77].

An NMR investigation of the $NaF-Na_2O-B_2O_3$ system by Kline and Bray [104] concluded that some of the retained fluorine was directly bonded to boron over a concentration range for NaF (= $[Na_2O]$) of ~ 1 - 25 mol %. However, this figure is undoubtedly influenced by water since the stoichiometry assumptions (from which these concentrations were obtained) were not self-consistent.

Mossbauer and ESR studies performed on potassium borate glasses containing a low concentration (~ 0.6 mol %) of potassium chloride together with ferric oxide (included for the Mossbauer studies only) [105] showed from both techniques that B-Cl bonds exist for modifier oxide concentrations higher than 15 mol %, but that interstitial chlorine is prevelant below this.

Finally, a series of papers directed towards the $AgX-Ag_2O-B_2O_3$ system (X = halogen) by Minami et al. [33,106] showed, from measurements of silver ion conductivity in glasses having a constant AgX content and variable Ag_2O concentration, that not all the silver ions contribute to the measured conduction. With additional information obtained from quantitative infra-red studies, a model was presented to explain this based on the 'pinning' of silver ions within the network, necessitating the presence of B-X and B-O-X bonds to maintain electroneutrality.

However, the evidence in favour of interstitial halides is overwhelming, both in the ionic lithium and sodium systems, based largely on conclusions obtained from ^{11}B NMR, as stated earlier. A further report of Raman spectroscopy of lithium halioborate glasses [108] also

attempts to show no direct structural reorganisation with halide addition, but subtle differences in the spectra presented can be observed upon careful examination. Moreover, a simple calculation also enables spectra to be compared by eliminating any discrepancy that may be due to the introduction of additional oxide if the halogen were to have volatilised during melting.

Therefore, one may conclude that it is highly unlikely for boron-halogen bonding to dominate in a haloborate glass, but that any effect present will increase as the pentaborate composition is approached.

2.2.3 Mechanical Properties

2.2.3.1 Elastic Properties

These comprise the main elastic moduli, namely Young's, shear and bulk, and the Poisson ratio σ, which are interrelated by a series of simple equations [108]. In general, Young's modulus E is paid the most attention by the materials science community, since it can be used indirectly to check one type of fracture toughness measurement, which will be discussed in more detail shortly. Young's modulus can be found by a variety of techniques, but in practice 3- or 4-point bend tests are used, the formulae for which may be obtained from results given by Hollenberg et al. [109] for bars of rectangular cross section:

$$E = \frac{Fl^3}{4\xi B^3 w} \qquad \text{(3 point)} \qquad (2.18)$$

$$E = \frac{(L-l)^3(L+2l)F}{4\xi B^3 w} \qquad \text{(4 point)} \qquad (2.19)$$

where the appropriate quantities are indicated in Figure 2.15. It can be seen that equation (2.19) reduces to equation (2.18) for $l = 0$.

2.2.3.2 Mechanical Strength

When a structure is loaded to failure, the ensuing catastrophic collapse may be categorised into two dominant regimes. Both are dependent upon the presence of defects, but the interactions between these and the applied stress are completely different.

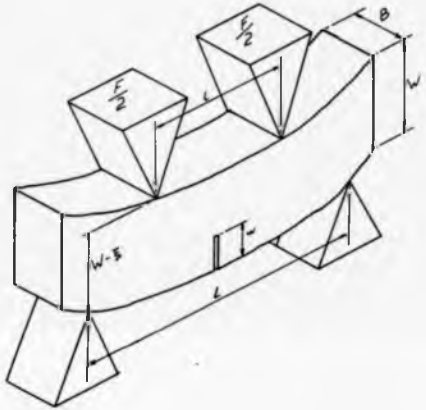

Figure 2.15 Illustration of quantities used in equations for Young's modulus and K_{1c} determinations.

The first, with which one is probably most familiar, is that observed in ductile metals. The behaviour is elastic up to the limit of proportionality, whereupon plastic flow occurs due to the sliding of crystal planes over each other, producing a large number of dislocations which tangle and temporarily strengthen the material (yielding) before eventual failure [110]. In this instance, the presence of "stationary" defects within the crystallites' lattice act to pin the dislocations and postpone the effects of plastic deformation to higher applied stresses. This is the main purpose of large interstitial and substitutional atoms introduced to form high strength steels, and the tempering process to produce small prestressed grains.

The second, which will be most prominent in the following discussion, is fracture oriented, i.e. failure before the onset of large scale yielding. In this instance the introduction of large scale flaws (e.g. surface scratches, inclusions or voids) and the surrounding localised stress fields are of prime importance to the observed strength. Here the microscopic defects are of secondary relevance. The so-called brittle strength of solids is determined by two principal mechanisms: the introduction of these flaws, and their subsequent extension under an applied stress. The defect ultimately responsible for failure is known as the critical flaw.

The starting point for this discussion then is to examine the effect of a given flaw distribution on the measured strength of a solid material. The first reference to this for brittle solids (i.e. when failure occurs almost instantaneously, known as fast or brittle fracture) was in 1922 by Griffith [13], who investigated the flexural strength of glass fibres as a function of exposure time to atmospheric moisture. The critical force was found to depend strongly upon this parameter, changing from a broad distribution for the pristine fibre to a sharper one having a lower mean strength for damaged specimens (see Figure 2.16) [111].

For the pristine fibre, the flaw density is relatively low, thereby necessitating the introduction and subsequent propagation of flaws via the coupled stress alone. For this reason, the strength was found to approach the theoretical value for glass (the force required to break each chemical bond in turn), thereby providing experimental confirmation for a theoretical assumption used in the mathematical models which attempt to interpret these observations,

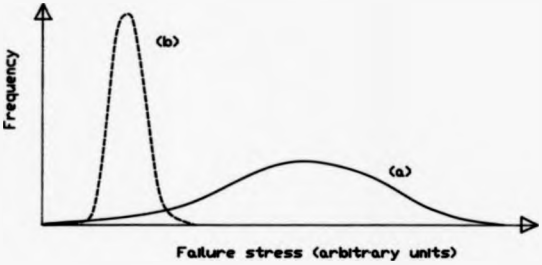

Figure 2.16.
Typical distribution of flexural strengths for specimens having
(a) a low residual flaw density.
(b) a high residual flaw density.

namely an atomically sharp crack. The scatter in values arises from two effects, namely the uneven flaw distribution and thereby its erratic spatial position, and the strong position-dependent tensile stresses experienced at the surface.

However, for the fibres exposed to moisture for a longer time, small unobservable surface cracks are postulated arising from some "corrosion" mechanism (known as Griffith cracks). These are distributed more uniformly and there is now a higher probability of a flaw being present in the region of maximum stress, thereby leading to the observed combination of a sharper breaking strength distribution at a lower mean value. A similar distribution sharpening was also observed with increasing fibre diameter, since this will also produce a higher flaw population per unit length. In fact, this particular dependence was used to calculate the above-mentioned theoretical strength, by extrapolation to zero diameter fibres.

Furthermore, Griffith presented an energy balance criterion for crack extension. That is to say, if the probabilities of all the possible fracture paths were evaluated from an energy-oriented viewpoint, the most probable option and all subsequent parameters obtained therefrom could be predicted. For example, to extend a crack, the energy supplied must be greater than the sum of the free surface energy of the newly-created surfaces, the bonding energy of the matrix through which the crack extends, and other additional terms from the extension of the plastic stress field, to be discussed shortly. This energy is obtained from the decrease in the localised elastic strain energy as the crack propagates.

In practical situations the presence of a great many variables, such as slow crack growth, fatigue, and stress corrosion cracking, render an energy-based description highly complex. Therefore, an equivalent approach which circumvents these difficulties is now favoured following its development by Irwin [112], and is termed the stress intensity approach. It essentially states that for a crack to extend, a material in the vicinity of the crack must have been stressed beyond its elastic limit, and can therefore be thought of as experiencing a localised plastic stress field. The behaviour of the crack in this local environment can now be visualised in terms of applied stresses rather than energy, with the plastic stress field having to attain some critical value for the crack to extend. The magnification of the stress observed at the crack tip relative to the applied

stress is known as the stress intensity factor K, arising from the result central to all theories of crack extension, namely that the point stress is higher in regions of small curvature.

It is the measured value of K at failure (the critical stress intensity factor, or fracture toughness) that is generally felt to be a measure of the overall mechanical resistance. This, as we shall see, is not as comforting as might be first thought, for a variety of reasons.

In practical systems, the thermal and chemical effect of the environment on the stress at flaw tips is of major importance. Allen [113] recently drew attention to this by examination of the static fatigue (failure under a constant, sub-critical load) of sodium β-alumina in liquid sodium. Results showed that the fracture toughness has but a small dependence on overall lifetime; the primary effects being the threshold stress intensity factor (where the crack first begins to extend), and the dependence of crack extension and the initial flaw size upon the stress intensity factor.

This work, as did the foundation work of Griffith, includes the additional effect of a chemical environment in the vicinity of the crack. This must we feel be considered in all cases, since to dismiss the effect of a chemical environment without suitable precautions, as has been demonstrated in these two pieces of work, can produce surprising consequences in a more thorough study. Various other pieces of work have shown that the presence of different media at the crack tip can effect either crack extension (which when combined with an applied stress leads to the phenomenon of stress corrosion cracking [114]) or crack "blunting" (i.e. dissolution of surrounding material to increase the local radius of curvature, hence reducing the stress concentration [115,116]). In some cases, generally with the presence of an inert medium, partial crack healing (the closure of a fracture surface, illustrating the "reversal" of the energy balance equation) has been reported [117,118]. Even this simple introduction, then, provides a flavour of the subtlety and complexity required to perform meaningful and reliable strength measurements.

2.2.3.3 Measurement

2.2.3.3.1 Hardness

The measurement of a low hardness value may be thought to indicate the ease of introduction of surface flaws into the specimen, a property deemed important by the arbitrary criteria presented in the above introduction. An extension to this concept has also created interest in the idea that the stress field formed in a conventional hardness test may be used as the site of a critical flaw in a new type of toughness test, to be discussed in the next section. A hardness value is determined from the local plastic deformation of the test material by a small area probe (indenter) under a given load for a given (standard) time.

Testing falls into two categories, using "sharp" and "blunt" indenters.

Hertzian [119] and Rockwell [120] tests employ blunt indenters, the Hertzian test relying upon the initiation and propagation of a "cone crack" around the test piece following the line of stress concentration, and as such is destructive in that the specimen is tested to failure. Furthermore this method is in general only applicable to transparent specimens since the crack has to be seen to form right round the indenter, although significant progress has been made to generalise the technique to opaque solids using sapphire spheres both as an indenter and an objective lens [121]. However this technique is not considered generally applicable since the deformation of the indenter itself has to be corrected for in the ensuing analysis and is therefore relegated to its particular specialised applications. Rockwell tests, however, measure the size of the plastically-deformed region beneath the spherical (usually steel) indenter. This uses in effect an "intermediate" material deformation mode, between the destructive Hertzian method and the "non-destructive" sharp indenter measurement techniques described below.

Measurements made using sharp indenters provide fewer constraints to the experimenter. Here diamonds are used as the probe material, thereby eliminating the problem of later correction for indenter deformation in the analysis. Also, since the specimen does not have to be tested to failure here, sharp indenters can be used in quality control of finished products in an industrial environment.

The indent should not weaken the structure since if the material "passes" the test, then a load exceeding the design limits will be necessary to overcome the surrounding compressive stresses and extend the localised cracks [122].

One ambiguity exists when comparing hardness values presented by different authors, in that the hardness value is force per unit area (per unit time), which leaves the areal parameter open to interpretation as either actual contact area or measured area on a horizontal projection. Although a simple premultiplier correction is available, it does not appear to be widely adopted, and may be omitted in the majority of cases.

As one final note, a method has been tentatively presented for the determination of Young's modulus via the measurement of hardness using two different indenter geometries, namely the Vickers and Knoop diamonds, shown schematically in Figure 2.17. As can be seen, the Vickers indenter is of square cross-section, and will produce a pyramid-like imprint. The Knoop geometry, however, with its 7.11:1 aspect ratio produces a "boat-like" indentation, which will deform the test materials anisotropically with respect to its two principal axes upon removal of the load; the restoring forces on the minor axes giving rise to a much larger elastic-plastic deformation. As indicated, this is dependent upon the elastic moduli of the test material, and the relative deformations have been shown analytically to lead to a measurement of the ratio E/H when combined with the comparatively isotropic relaxation from a Vickers geometry [123,124]. One might then be tempted to quote E from this measurement if the other parameters can be suitably approximated. However, as pointed out in the work cited, the measurement uses two different hardness values, and so the problem of selection is presented. This method should therefore be discouraged except to draw the most tentative conclusions. One further indenter type has been presented in the literature based on a tetrahedral geometry [125]. However its lack of versatility in new toughness measurements appears to have restricted further investigation.

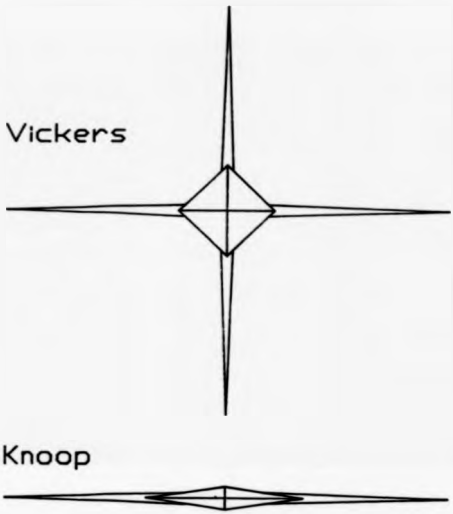

Figure 2.17.

Comparison of Vickers and Knoop indentations.

2.2.3.3.2 Toughness

The quantity used to provide a measure of the resistance of a material to crack propagation under an applied stress is termed the toughness of a material. This should be distinguished from strength as quickly as possible; for example wood is tough but not strong, steel is strong but not tough. The extensive investigations performed in the literature on brittle materials might then be thought to have been directed towards high strengths (i.e. maximum sustained loads), but as indicated in the introduction to this section, it is the resistance to crack propagation (hence the toughness) that is of paramount importance in the development of engineering ceramic composites.

The first problem in this type of measurement is concerned with the size and position of the critical flaw. Specimens may be tested in an "as received" condition, and the history of the critical flaw determined by examination of the fracture surface. The work reported [126-128] does appear encouraging in the adoption of the method, but for the possibility of ambiguities introduced at sub-critical stresses. One example of this is stress corrosion cracking, where atmospheric solvents attack the exposed highly-stressed regions of the crack, causing extension at very low loads [129-131]. Elimination of this process is straightforwardly accomplished by surrounding the crack, and particularly the crack tip, with an "inert" medium [132]. This in turn defeats the purpose of the test to some extent, since the material will be exposed to potentially hostile chemical environments under normal service conditions.

Another, possibly more satisfying alternative, would be to introduce a known critical flaw to the material, and examine the progress of the crack under an applied stress by later reference to the fracture surface. Once this work has been performed to a satisfactory conclusion, the flaw statistics associated with a given production process may then be determined via measurement of the Weibull modulus [133,134].

Ideally, the most satisfactory measurements would be obtained from industrial components, but this can be prohibitively expensive. A cheaper, easier and more informative

strategy is to perform a series of tests upon simple geometries (i.e. bars and plates) and process the results to provide a feel for the overall mechanical response. The quantity most often associated with this concept is the critical fracture toughness in flexure, K_{1c}. The difference in failure modes is illustrated in Figure 2.18, and assigned the nomenclature first proposed by Irwin [135].

Obviously, the additional freedom allowed for the directionality of crack propagation provided by the biaxial test (using a plate specimen) means that the results obtained will be more easily related to a complex fracture (i.e. in an industrial component), but unfortunately they cannot be simply analysed to indicate the corresponding toughness value, although a measure of the resistance to failure can be derived via the Weibull modulus [136]. Even so, a brief indication of the biaxial strength technique is useful, since it can in principle provide more valuable information than the uniaxial test (using a rod or bar specimen) when material strengths are compared intrinsically.

There are three principal methods for the biaxial determination of toughness. These are the A.S.T.M. method for testing ceramic tiles [137], and the ball-on-ball/ball-on-ring tests designed and implemented by Ritter et al. [138]. These latter techniques have been compared with the conventional uniaxial results in order to derive a "feel" for any correspondence between material independent parameters (which K_{1c} is often presented as [139,140]) and the critical stress values obtained from biaxial measurements. These have included a limited study of the overall effect of a known critical flaw (a Vickers indentation, see 2.2.3.3.1) beneath the contact area of the loading ball on the opposite side [141]. This is not as quantitative as might be first thought since the interaction of the driving stress field from the point of application of the stress with the flaw is a strong function of displacement. This problem will be returned to in the following description of some methods used in uniaxial testing.

Historically, the determination of toughness was oriented towards all three failure modes, and the description of a semi-empirical relationship which would allow values to be calculated for geometrically simple specimens on a routine basis. Moreover, simple shapes are relatively easy to machine on a large scale, an important consideration in material evaluation,

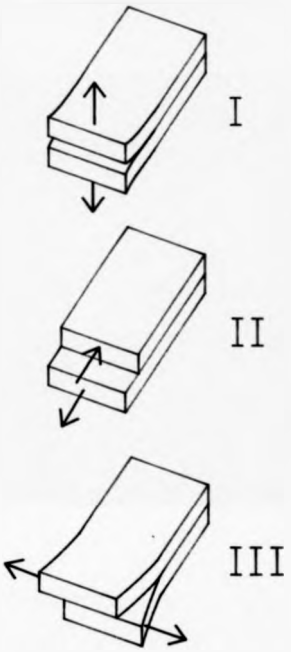

Figure 2.18.
The three fracture modes encountered in mechanical strength testing.

since despite numerous attempts to obtain mechanically similar specimens, a 10 - 15% scatter typically exists in all previously reported work [142].

In the special case of the K_1 fracture mode, the first steps were taken in a series of papers in which "K calibrations" for 3- and 4-point loading of a standard brittle metal bar were experimentally determined [143] and compared with the results from a theoretical non-linear stress analysis approach [144,145] by Brown and Srawley [146]. The "K-calibration", or specimen compliance, measures the size of the elastic-plastic stress interaction by the systematic determination of displacement as a function of (non-critical) load for a variety of critical flaws (in this case, milled slots of different depth). An investigation of the dependence of other experimental variables was also undertaken (height, width and length of the test bar, together with the separation of the loading points) to produce the following equations which were found to hold so long as the conditions given below the equations were satisfield.

$$K_{1c} = \frac{3F_cD}{BW^2}w^{\frac{1}{2}}\left[1.99 - 2.47\left(\frac{w}{W}\right) + 12.97\left(\frac{w}{W}\right)^2 - 23.17\left(\frac{w}{W}\right)^3 + 24.8\left(\frac{w}{W}\right)^4\right] \tag{2.20}$$

$$K_{1c} = \frac{3F_cD}{BW^2}w^{\frac{1}{2}}\left[3.86 - 6.15\left(\frac{w}{W}\right) + 21.7\left(\frac{w}{W}\right)^2\right]^{\frac{1}{2}} \tag{2.21}$$

$$D = \left(L - \frac{l}{2}\right)$$

$l/W \geq 2$; $L/W \geq 4$; $0 \leq w/W \leq 0.6$; $2 \leq W/B \leq 8$, so that friction on the loading points becomes insignificant. The appropriate quantities are indicated in Figure 2.15.

These have been conveniently summarized by Ewalds and Wanhill [112] from the ASTM standard. One of the criteria is that $0.45 \leq w/W \leq 0.55$, but by graphically plotting the (dimensionless) polynomial approximations to the specimen compliance [146] (i.e. without the specimen dependent premultiplier terms) presented above as a function of w/W (Figure 2.19), it can be seen that a w/W of 0.3 is at the extreme position of agreement between the above relationships. Therefore a w/W of $\approx$ 0.3 will be used for the toughness determinations in this work.

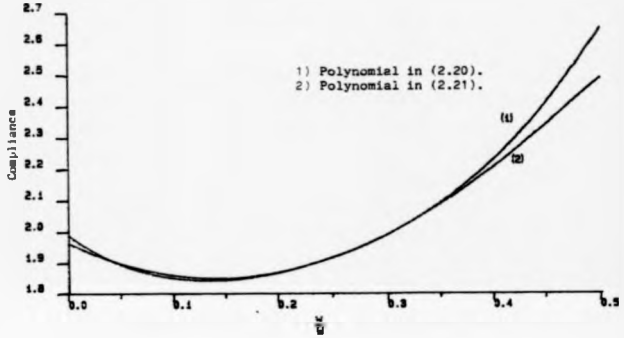

Figure 2.19. Variation of specimen compliance with notch to thickness ratio for two different calibrations.

Even so, the requirement for a technique which was equally applicable both in the laboratory and in an industrial quality control environment was quite strong, and a new method, using an indentation as the source of the critical flaw, was developed to meet this need [127,128]. It was further postulated that a value directly proportional to the K_{1c} value determined by notched-beam methods could be obtained from the length of the radial crack and the size of the central plastically-deformed zone. The nomenclature of the three different types of crack caused by a sharp indenter is indicated in Figure 2.20. In many respects, the indentation method of toughness testing seems ideal: the critical flaw closely resembles the crack that would cause failure "in the field", namely cracks introduced during final machining, and several values for K_{1c} can be obtained from a single test piece. If a second, similar indent is situated close to the first, but sufficiently far away that the associated stress fields do not interact appreciably, then one of the cracks will extend sub-critically to the approximate size of the critical flaw at the onset of failure of the other under application of a given load. This allows a value of the crack size at the instant of failure to be independently obtained. Furthermore, stress corrosion effects can be eliminated by simply placing a drop of an inert medium (e.g. silicon oil) on the selected site prior to indentation [127], and subsequent flexure in a 4-point bend. This geometry is necessary due to the uniform stress distribution required on the tensile surface between the central loading points [147]. The type of indenter must be restricted to a Vickers, since symmetrical cracks are required both parallel and perpendicular to the faces of the test piece, to evaluate the sub-critical crack extension experienced upon loading. The relevant equations for K_{1c} by this technique are:

$$K_c = \phi_V^R \left(\frac{E}{H}\right)^{\frac{1}{2}} \frac{P}{c_o^{3/2}} \qquad (2.22)$$

where ϕ_V^R is a material independent constant for Vickers indentations experimentally determined to be 0.016 ± 0.004,

$$K_c = \eta_V^R \left(\frac{E}{H}\right)^{1/8} (\sigma P^{1/3})^{3/4} \qquad (2.23)$$

where $\eta_V^R = [(256/27)(\pi\Omega)^{3/2}\ \phi_V^R]^{\frac{1}{2}} = 0.59 \pm 0.12$ [128]

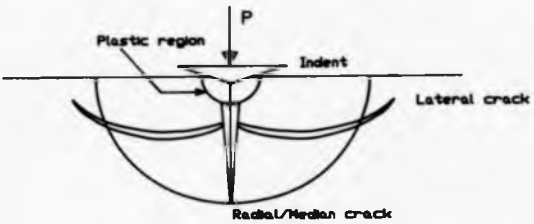

Figure 2.20.
Nomenclature of cracks formed from a sharp indentation.

$$K_c = A\sigma_m c_m^{1/2} + B, \qquad (2.24)$$

where A = 2.02 and B = -0.68 $MPam^{1/2}$ [148]

Here, P is the indentation load, c_o the crack length immediately after indentation (care being taken to eliminate any environmentally assisted sub-critical extension by performing the indent in inert surroundings), c_m the crack length of a neighbouring indent after fracture, Ω a crack-geometry factor, and σ the applied stress at failure.

Unfortunately, the indentation technique suffers from several fundamental problems. Firstly, the K_{1c} values determined are consistently and systematically lower than those obtained from conventional notched beam tests, which led to the introduction of a "universal calibration" [149], reproduced in Figure 2.21. This was modified in a later publication [145]. This discrepancy in K_{1c} values is attributed here to the additional energy required by an indentation in the creation of lateral cracks, the effects of which have not been satisfactorily accounted for in the general case within the background theory [150]. More importantly, perhaps, is that the measurements of toughness determined from this indentation method are only as valid as the notched beam reference values. Examination of the currently accepted materials science technique from an engineering-based metallurgical standpoint clearly shows the adopted test geometries to be invalid [135], since calculated values of the size of the plastic stress field surrounding the crack tip are, in general, a significant fraction of the specimen thickness. Moreover, the dimensional requirements associated with equations (2.20) and (2.21) are often violated. These conclusions essentially state that K_{1c} values are dimension and preparation dependent to some extent in ceramic materials. This is further demonstrated by reference to two other pieces of work. Henshall et al. [125] reviewed a number of polynomial expansions for compliance in 3- and 4-point flexure, by comparison of the processed K_{1c} values for silicon carbide. The optimum fits were then ranked by examination of their respective dimensional dependences, namely the notch depth to thickness ratio a/W. Ideally, for a valid determination of a material property to be made, the processed value should exhibit no dependence upon material dimension, which is reflected by the correlation of the evaluated parameter with

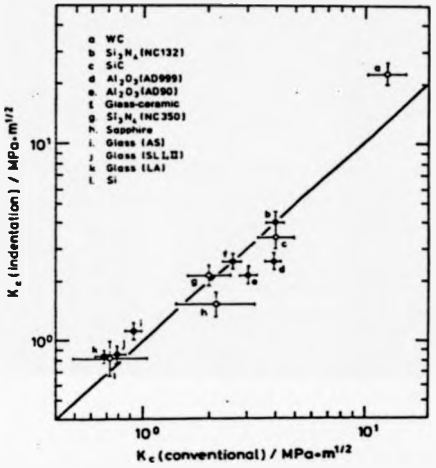

Figure 2.21. Comparison of toughness values obtained using indentation and conventional means. After Anstis et al. [149].

specimen size. For a valid material property the correlation coefficient will be zero. In this trial to obtain the supreme equation for K_{1c} determinations, the "best" equation was found to yield a correlation coefficient of 0.11.

The effect of the notch introduction from a mechanical standpoint has been researched by Pabst [151], who has demonstrated that the measured K_{1c} is slightly dependent upon the notch shape and the grit size of the diamonds on the saw used to cut the notch, but quite surprisingly, highly dependent upon the notch thickness itself, for notches having a square profile. These conclusions are in agreement with a non-linear stress analysis performed by Manning [152]. In the instances where the fracture toughness is dependent upon specimen size as stated by the ASTM standard, an effective K_{1c}, K_{1Q}, can be determined and equated to the "actual" value if a series of criteria can be satisfied [112].

One further problem, which is applicable to all strength measurements in brittle solids, is the important effect of slow crack growth. If a flaw is present in an otherwise elastic material, then a crack will extend over a period of time to alleviate the localised stress field. In this manner, an initial microscopic flaw can grow to a crack of catastrophic dimensions. This is the basis of the description presented for the lateral cracks present in indentation toughness testing [150].

This phenomenon is further complicated by the effects of a chemical environment in the case of surface flaws. The ensuing degradation is termed stress corrosion cracking, and although investigated extensively by engineers [114,116], has only recently attracted limited interest on a qualitative basis by materials scientists [115,116,131].

Qualitatively speaking, the mechanically-observed consequences of a mildly corrosive external environment on a stressed section of material are extreme. In some instances, the plastically deformed areas surrounding the crack tip are preferentially dissolved instead of the exposed individual chemical bonds at the crack tip, thereby increasing the crack tip radius and so decreasing the localised stress [153]. This is colloquially termed "crack blunting". However, for the remainder of materials, it is the crack tip itself that is attacked, thereby further weakening

the material, and is accelerated still further under the influence of an applied tensile stress. The mechanism can be interpreted by reference to Figure 2.22 after Lawn [116], which indicates the basic features of stress corrosion.

Most systems, however, are not quite so fortunate in that the underlying mechanisms cannot be readily understood, and it is felt by the author that unless specifically investigating this aspect of material degradation in a hostile environment, the potential influence of stress corrosion should, where possible, be eliminated. In the event of doubt, the toughness tests should be performed under more reproducible standard conditions.

2.2.3.3.3 Stereological investigations

Generally speaking, the proportion and relative size of different material phases in a composite are only evaluated when looking at a particular aspect of strength, namely its variation with grain size and distribution. Work of this kind implies that the bulk strength passes through a maximum when plotted vs. the variation of mean crystallite size in sintered materials [154-156]. Volume fraction measurements are used as a complementary technique to provide a "feel" for the inter-granular separation. With the superior control of such macroscopic quantities realised by glass-ceramics, the need for measurements of this type become even more important, so that nucleation densities and crystallisation conditions may be optimised.

Just as mechanical strength may be linked to volume fraction and mean crystallite size by the statistical distribution of fracture paths (crack branching being assumed to be reduced for "fast" fracture, implied by sharp critical flaws [112]), so should conductivity by the relative trans- and inter-granular contributions. Hence a tenuous link between these two quantities has been established, and as such would seem a natural parameter to interpret electrolyte degradation results, although the reproduction of a similar argument in the literature appears to be lacking.

One major problem exists in the interpretation of these measurements that has not been mentioned yet - that of the characterisation of particle shape. In order to calculate mean crystallite size, assumptions of simple, readily expressed geometries must be made [157]. To justify the equivalence of volume fraction measurements to simple point counts (frequency of

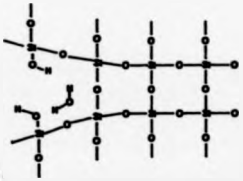

(I) Physisorption of water molecule onto strained crack tip bond.

(II) Reaction occurs to rupure bond

(III) Formation of silanol covered fracture surface

Figure 2.22.
Stress corrosion mechanism in silica glass. (After Lawn [115])

occurrence of a given phase lying on a grid comprising equidistant points, normally on a square grid, which should ideally be based upon an equilateral triangle), the objects under examination must be randomly oriented spatially. This tends to place often difficult and unattainable limitations on the experimentalist, and so unjustified conclusions are drawn. Unfortunately, more time- and energy-consuming alternatives (namely line and areal ratios) do not provide proportionately more insight. The only formal description that has made some progress in this direction, albeit incomplete, is the complete functional description of the structure [158]. However, after the time spent in the acquisition of a sufficiently large database, the results must still be processed in a fairly basic way to enable correlation with other quantities of interest to the materials scientist, such as strength, thermal expansion and electrical conductivity. Therefore, it is probably more reasonable to take raw data for the simplest case (point count), and draw tentative inferences from the wholly unjustified relationships given for the simpler geometries.

2.3 SPECIMEN PREPARATION

This particular aspect of materials evaluation is often considered trivial and taken for granted. Here we review some of the techniques in general use, and present some ideas for modification in the light of these aspects, by which statistically better and esoterically more standardised results may be obtained.

2.3.1 Melting

Several problems are apparent here: the volatilisation of constituent compounds [159], the introduction of water to the melt (borax, $Na_2B_4O_7$, is found to contain 2 wt % water at its liquidus temperature under atmospheric conditions [160]), and the dissolution of the crucible by the glass itself (platinum, for example, is readily dissolved by melts having a high alkali oxide/halide content).

2.3.2 Annealing

Examination of the literature shows steep viscosity-temperature characteristics to occur in sodium tetraborate (borax)-based glasses [72,91], which when combined with values of linear thermal expansion coefficient [72,161], leads to the inference that very precise temperature constraints must be imposed to obtain large blocks of glass in this system. The reason for this is that the stresses caused by the expansion mismatch upon non-uniform cooling of the block to the annealing temperature will undoubtedly be comparable with the critical stress value necessary for fracture [22].

2.3.3 Nucleation and Crystallisation

When the kinetic barriers within a fluid favour crystallisation [162], the starting points (nucleation centres) fall into three categories: namely homogeneous, heterogeneous and surface nucleation. From the viewpoint of the commercial production of an article, probably the optimum and most reproducible physical properties are obtained in the above order.

In general, homogeneous nucleation is not observed for the majority of glass systems. Here the sites are distributed uniformly throughout the network on a microscopic level. More often localised concentrations of a more readily crystallising phase may be observed, giving rise to heterogeneous nucleation. This may be introduced artificially into less readily crystallised glasses by the addition of trace quantities of "nucleating agents" to the starting composition. The microscopic mechanisms associated with nucleation in general are complex and not well understood. Qualitatively, there are two main types of nucleating agent. Either a dispersion of metallic granules may be created or a microscopically small second glass phase which crystallises readily [163]. Larger crystals may then grow on the facets of these nucleation sites, or at the stressed interfaces of the second glass phase itself with the main matrix, although the concept of this latter mechanism has not been extensively studied.

Whilst the first two possibilities can produce a fine grained, evenly dispersed crystalline sub-structure within the finished article if the appropriate heat treatment schedule is employed

(the underlying reasons can be more easily understood by reference to Figure 2.23), the latter category, surface nucleation, leads to an overall reduction in physical properties and a generally unsightly appearance. Here the material is very poorly nucleated and the crystallites are free to grown in an uncontrollable manner, often forming large spherulites; the dendrites from which extend into the bulk to give axial non-uniformity in properties and a central depletion volume, known as piping. Probably the greatest single cause of this phenomenon is water [164], with other more widely publicised culprits, such as dust particles [11] and surface stress gradients coming a poor second.

Obviously from the above, albeit brief, overview, the value of kinetic evaluation of the nucleation and crystallisation properties of a material is immense. Much of the work in this field has been on heterogeneous crystallisation catalysts performed by James [163-165] on lithium silicate-based glasses, an excellent vehicle towards a fuller understanding of this important aspect in the production of high quality commercial products.

2.3.4 Polishing

Although again frequently taken for granted, the measured properties often reflect the way in which an article is finished. There is increasing evidence that the compressive surface stresses introduced during polishing give rise to an increased resistance to mild chemical attack and possibly greater observed mechanical strength. For instance, work performed on the degradation of sodium β-alumina in the environment that might be expected in service in the sodium-sulphur cell [5] has shown that fine ($\sim$ ¼ μm) polishing increases the time before the formation of dendritic sodium can be observed.

However, dissolution studies on optical glasses using water [166] have shown no dependence upon surface preparation. In the latter instance, it is postulated here that the effects of a pre-stressed surface would only be observable in cases of low corrosion rates, since in the case of a high dissolution rate, the chemical resistance itself is being examined and not the subtle microscopic variations characteristic of the reaction surface itself. Furthermore, in strength-oriented investigations using Vickers indents, a 50 μm compressive surface layer has

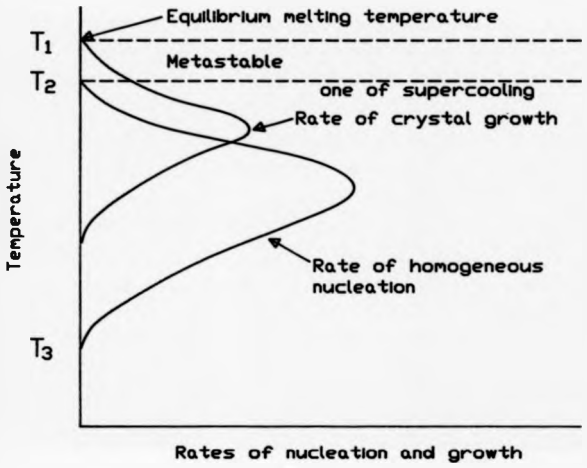

Figure 2.23.
Crystal nucleation and growth kinetics.

been shown to enhance the breaking strength of a commercial glass-ceramic by ~ 30% [167]. Therefore, it is felt that a realistic appraisal of the extent of this damage in strength specimens is valuable, so that accurate and meaningful estimates of bulk strength can be obtained. This necessitates an understanding of the mechanism of introduction of surface stresses, and so of the abrasion process on a microscopic level.

Abrasion in the first instance may be thought of by consideration of the concept of forcing a single sharp probe along an initially pristine surface. This will lead to the production of a modified planar version of the cracks and associated stress fields that might be expected from a sharp (e.g. Vickers) indenter (Figure 2.17).

For many years the understanding of the polishing mechanism followed similar reasoning. The microscopic 'ridges' were thought to flow into the 'troughs', creating regions of a new material phase, as indicated in Figure 2.24. This is known as the Beilby layer. A fairly recent article [166] has examined the polishing mechanism in more depth for a selection of optical glasses, by conducting an investigation of the variation in removal depth with changes in softening temperature, resistance to chemical attack and micro-hardness. Since the removal rate was not seen to be a strong function of softening temperature or chemical resistance Izumitani rejected the flow and plastic deformation theories. However, the concept of the Beilby layer was adopted since it explained the reappearance of surface scratches on a highly polished surface when lightly etched, which would also appear consistent with the plastically-deformed sub-surface idea. The conclusions made from this work indicate the principal material removal mechanism to be the creation of a 'soft' surface layer by the action of the lubricant employed, which can subsequently be more easily removed by abrasion. The author is in little doubt that the above results and conclusions are sound, but feels that the argument may obscure a full description of the surface after polishing, since this work unfortunately did not examine the surface properties after preparation with the same rigour as the behaviour during polishing.

More recent work based on metals [168] has favoured a plastically deformed sub-structure argument indicated in Figure 2.25a, to rewrite the standard explanation, and replace the old criterion for polishing with successively smaller grits; namely removing the

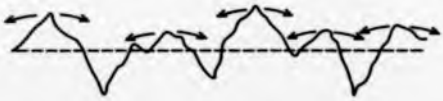

Initial surface. Arrows indicate direction of material flow during polishing.

Surface after polishing. Beilby layer shaded.

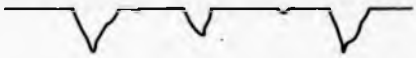

Reappearance of scratches after etching.

Figure 2.24.
The classical interpretation of polishing damage via the Beilby layer.

Deformation regions given by Elastic-plastic theory

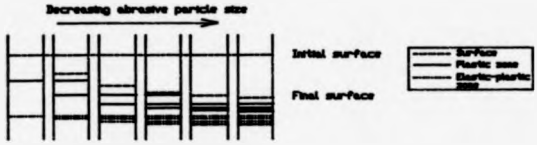

Deformation regions produced using accepted polishing criterion.

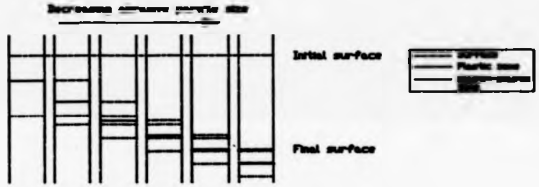

Deformation regions produced using modified Elastic-plastic criterion.

Figure 2.25.
Explanation of a new polishing criterion using an elastic-plastic theory.

scratches left by the previously used larger particles, by polishing with the "old" grit for a significantly longer (unspecified) time. A modified criterion is postulated here for brittle solids, assuming the plastic stress field to extend into the material to a depth a, of the order of the particle size causing the current surface damage, and the elastic-plastic boundary a further depth b, of the same order again. (This is validated by reference to Figure 1 in reference [167].) That is to say, an additional depth equal to the "old" particle size requires removal after the first observed disappearance of the associated scratches. The difference between these two techniques is illustrated in Figures 2.25b and 2.25c. These block diagrams indicate the build up of the stressed layers by showing the appropriate limits of a (the plastic zone) and b (the elastic-plastic zone) as the polishing progresses to finer abrasives. A high density of lines therefore indicates a high compressive surface stress. This compression has been investigated more fully by Johnson-Walls et al. [169]. Here, thin plates of brittle materials were prepared by highly polishing one side flat, and mounting upon a rigid bed prior to machining the other side with a coarse diamond wheel. The resulting curvature observed on removal was attributed to residual surface compressive stresses on the machined face. Therefore, the "old" polishing criterion is tantamount to the production of a significant compressive surface stress, where the postulated idea removes this. The primary vindication of this concept would be in the enhanced statistical correlation with a lower mean strength in a standard stress-to- failure test.

2.4 AIMS OF THE THESIS

Following the foundation work by Badzioch [8] and Daniels [9], where fixed frequency conductivity measurements were made as a function of temperature, the results were felt to be sufficiently encouraging to attempt to categorise those materials mechanically. This next step towards an eventual production route to sodium β''-alumina as a solid electrolyte would involve an optimisation of the crystallisation/microstructural characteristics for conductivity and strength. Therefore a superior working composition was to be produced, and the most satisfactory heat treatment schedule determined by a study of the nucleation and crystallisation kinetics.

Moreover, to show the anticipated superior properties of haloborate-based glass-ceramics to sodium β''-alumina, work of high intrinsic value, as well as of commercial importance, must be performed. One particular aspect of this prerequisite was to attempt to determine the reasons behind the unique observation of a higher measured conductivity for haloborate-based polycrystals than for the corresponding glass. This would require an extensive database to supplement the conductivity data obtained by Badzioch [72] for a variety of cation-halide dopants. Ideally, measurements should be made in an environment that simulates the eventual working conditions of the material, but this raises both safety problems and unnecessary experimental complexity for this stage of system development. As a result, only limited studies of this kind have been performed. In general, "inert" environments were used where possible for the experiments reported here. Previous work has shown measurable effects to occur in the use of some gaseous environments during conductivity studies. The presence of oxygen was therefore avoided since some work has postulated a degree of oxygen ion conduction in a similar glass system [171], although disputed in later work on oxygen diffusion in the same system [172]. However, it is the sodium ion which is thought to be the principal charge carrier in the systems to be examined in this work [6.7.9]. The strategy adopted here will involve some measurements consistent with previous work, and the examination of the conductivity variation over a wider frequency range.

In the case of mechanical strength, the behaviour of cracks in the materials under test at room temperature in an inert (oil) environment is also assumed to provide some indication of performance under actual service conditions.

Probably the most intrinsically useful strength measurement for a macroscopically homogeneous test piece is the biaxial method, which will be pursued with some vigour. In terms of engineering parameterisation, the notched beam test is favoured for toughness determinations, with indentation tests performed where possible for comparison.

To remove the possibility of interference in the strength tests from the compressive stress introduced during "conventional" polishing, the technique described in section 2.3.4 will be adopted at all times, unless specifically stated otherwise.

CHAPTER THREE

EXPERIMENTAL AND RESULTS

3.1 PREPARATION

3.1.1 Glass Melting

The glasses used in this work were prepared from intimately mixed powders of the starting materials. For the borax-based materials, glassy anhydrous borax (Dehybor), supplied by Borax Research Ltd. was used in the batches, for convenience and to maintain a lower melting temperature. Badzioch [170] has shown an equivalence in conductivity behaviour between "Dehybor"-containing glasses and glasses formed using more elementary starting materials (i.e. boric oxide/boric acid and sodium carbonate). Differences could have arisen due to the possibility of retention of the water and carbon dioxide volatilisation products in the "elementary" glass. A typical analysis of impurities present in "Dehybor" is reproduced in Table 3.1. For the other additives, only analytical grade reagents were used. The batches were melted in zirconia grain stabilised (ZGS) platinum/gold and platinum/rhodium crucibles in an electric furnace at ~ 900°C, at which temperature the melts were seen to be very fluid.

The casting of large blocks of glass was initially hampered by the devastating combination of cracking and/or crystallisation during annealing despite using moulds heated to different temperatures, various annealing temperatures, and changing the time between pouring and annealing. Remelting the failed product was found to be impractical due to an observed "memory effect" [12]. A previously crystalline cullet was found to crystallise far more readily upon remelting; therefore fresh batches were used for each melt. This had an additional advantage since volatilisation was also reduced. The effect is measurable, as can be seen by a selection of "wet" chemical analyses of the final products (performed by Borax Research Ltd.) shown in Table 3.2. In an effort to parametrise this loss with melting time, samples of a CaB_4O_7-$CaCl_2$ melt (one of the first systems to be investigated in this work) were extracted and "wet" chloride analyses kindly performed by Mr H.J. Mathers. A graphical representation of this

Table 3.1 Typical Analysis of Borax, $Na_2B_4O_7$ (technical grade dehybor) [173]

Compound	Percentage by Weight
Na_2O	30.7 %
B_2O_3	68.9 %
H_2O	0.3 %
Fe_2O_3	0.009%
SiO_2	0.15 %
Al_2O_3	0.08 %
CaO	0.013%
MgO	0.05 %
SO_4^{2-}	0.025%

Theoretical Composition

Na_2O	30.80 %
B_2O_3	69.20 %

Table 3.2 "Wet" Chemical Analysis of Some Chloroborate Melts

Composition as Made	Composition as Analysed
$Na_2B_4O_7$	$0.94Na_2O.2B_2O_3$
$0.9Na_2B_4O_7.0.1NaCl$	$0.95Na_2O.2B_2O_3.0.032NaCl.$ $\approx 0.9Na_2B_4O_7.0.03NaCl$
$0.8Na_2B_4O_7.0.2NaCl$	$1.03Na_2O.2B_2O_3.0.37NaCl.$ $\approx 0.8Na_2B_4O_7.0.15NaCl$
$0.7Na_2B_4O_7.0.3NaCl$	$0.80Na_2O.2B_2O_3.0.36NaCl.$ $\approx 0.7Na_2B_4O_7.0.14NaCl$

data is shown in Figure 3.1. The chloride loss may be due to one of two mechanisms:

$$3NaCl + B_2O_3 \rightarrow BCl_3 + Na_3BO_3$$
$$\downarrow + H_2O$$
$$B_2O_3 + 3HCl\uparrow \qquad [174] \qquad (3.1)$$

$$4NaCl + O_2\downarrow + 2B_2O_3 \rightarrow Cl_2\uparrow + 4NaBO_2 \qquad [175] \qquad (3.2)$$

A similar problem of cracking in this glass system has also been encountered by other workers [176]. The solution, found after considerable effort, was to cast large (~ 2" ϕ) cylindrical blocks, which reduced the stress concentration at the corners, and hence the number of crack nuclei. The only cracking now in evidence was around the cylinder base, with occasional circumferential cracks on the main body. The steep thermal expansion and viscosity temperature characteristics were still in evidence, characterised by the appearance of a "dimple" on the top surface of the cylinder during cooling in the mould.

One further point of interest was the peculiar appearance of the melt during cooling. From the onset of pouring the yellow-coloured liquid into the mould, the presence of two distinct types of material are indicated by the formation of fairly large (~ 2 mm x 10 mm) reddish glowing regions within the yellow-tinted bulk material. This phenomenon persists down to just above the annealing temperature, where an overall colourless appearance characteristic of a single phase glass can be seen. The specimens appeared to show no subsequent stress birefringence [177], but the different regions frequently reappeared on sections through the cylinders, being highlighted by a light etch in air, moderate abrasive surface damage or devitrification, shown in Figure 3.56a. The absence of prestressing therefore presupposes this effect to be based in a compositional variation. No mention of this behaviour in what is conventionally referred to as a single phase glass can be found in the literature, although borate-based glasses appear to be notorious for phase separation [171].

For compositions approaching the limit of the glass forming region, crystallisation also became a problem, generally nucleating at the rim of the crucible in contact with the meniscus during melting, presumably from the condensation of volatilised material from the melt onto the

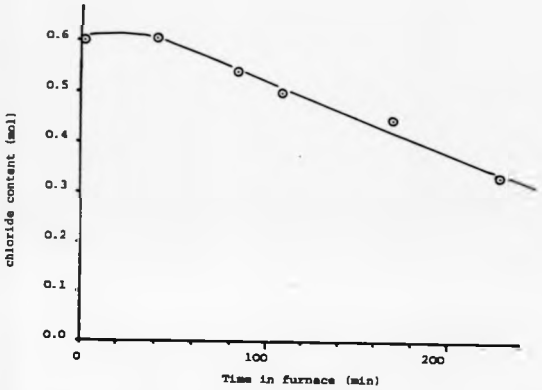

Figure 3.1. Graph showing rate of chlorine loss with melting time in a calcium chloroborate glass.

crucible. The inherent crystallisation within the mould was prevented by allowing the glass to precool slowly in the crucible before pouring. The mechanism may be thought of as reducing stress-induced crystallisation within the mould, as well as cooling the crucible rim and hence reducing the activity of these secondary nucleation sites. The above technique has also been successfully applied to other difficult glass-forming systems [178].

After performing a cursory check for the absence of residual stresses via observation of stress birefringence, the bulk glass was machined into specimens and, after visual rejection of damaged samples, subjected to heat treatment schedules.

3.1.2 Nucleation

Numerous trials to find an optimum heat-treatment schedule for the base glass, $Na_2B_4O_7$, were carried out, using both bulk glass specimens and hot-stage optical microscopy. In all cases the crystallisation was seen to be surface nucleated, in the form of spherulites penetrating the bulk glass (Figure 3.2), leading to the production of pipes in the final form (Figures 3.54a, 3.59). It was found that the presence of an "inert" powder surrounding the specimens leads to the production of a finer-grained surface microstructure. A series of rectangular blocks of glassy borax were prepared having an 800 grit surface finish and all sharp edges bevelled. The specimens were then surrounded in dried silica and alumina powders of different particle sizes on a clean, high alumina firebrick prior to heat-treatment. The effect upon the crystallisation process is shown in Figure 3.3. For the samples immersed in the finer-grained powders, the surface comprised a high density of small crystallites with no change in dimension. As the powder particle sizes increased, the specimens were seen to have expanded, leaving a thin (~ ¼ mm thick) crystalline crust on the surface of the alumina-coated material. Upon examination of a section through these specimens, large (< 1 mm ϕ) bubbles were observed. With the highest powder particle sizes available, very [illegible] of the glass was observed, with cracking of the block occurring from the large thermal expansion mismatch between the glass and the limited crystallisation from a single nucleus. No crystallisation was apparent for the specimen not surrounded by a powder used as a control. As

Figure 3.2. Hot stage micrograph showing poor nucleation and spherulitic growth in glassy borax.

Figure 3-3.

The effect of particle size and chemical composition of the surrounding powder upon the nucleation properties of glassy borax.

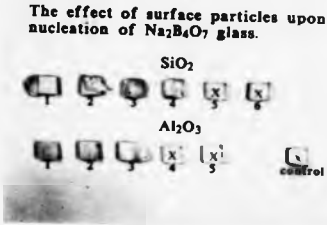

Powder size.	Particle size range (μm)
1	38
2	45 - 53
3	63 - 75
4	90 - 106
5	150 - 180
6	180

a consequence of this microstructure biaxial strength measurements were not thought to produce additional physical insight and subsequently rejected. Therefore, individually-machined specimens were exposed to the heat treatment schedules prior to machining and measurement.

It soon became apparent when this procedure was repeated with sodium chloride-doped glasses, that the nucleation density was vastly improved, although the devitrified materials still crumbled relatively easily under finger pressure. Therefore, bar specimens having a standard 300 grit finish were prepared from glasses containing different concentrations of the "standard" nucleating agents P_2O_5, TiO_2 and Pt and exposed to a simple heat treatment schedule for comparison purposes. The samples were placed on clean graphite dishes so that they did not touch each other, and these dishes were then stacked on thermally recrystallised alumina spacers in tiers prior to heat treatment to increase the thermal mass, thereby ensuring an equivalent heat treatment schedule for each series of "dopants". This comprised dwelling at 420°C for 3 h to relieve any surface strain introduced during machining and 500°C for 4h before cooling to room temperature, all temperature ramps being 4°C min^{-1}. The progression of the crystallisation process can be followed by reference to Figures 3.4 - 3.7, where the samples have been removed and air quenched at different times during the operation.

Several features should be noted from these figures:

a. All specimens appear to devitrify rapidly once some crystal growth has occurred.

b. Despite the consistent surface finish and heat treatment schedules, the devitrification of glassy borax (used as a control) was found to be irreproducible. "Complete conversion" to an opaque polycrystalline solid was found to occur at different points between the rise from 420°C to 500°C and holding to 500°C for 30 mins. This anomaly may be due to different concentrations of surface water that could have been unknowingly introduced in the sample preparation process. An experiment was carried out to investigate the effect of water: several rectangular pieces of glassy borax were ground to an 18 μm surface finish with champhered edges. These were then exposed to moisture sources for different times in an effort to determine the effectiveness of the storage techniques prior to heat treatment. The results of this study are shown in Figure 3.8, demonstrating that desiccator storage techniques produce similar

Figure 3.8.
Nucleation studies of glassy borax using NaCl.

Figure 3-5.

Nucleation studies of glassy borax using P_2O_5.

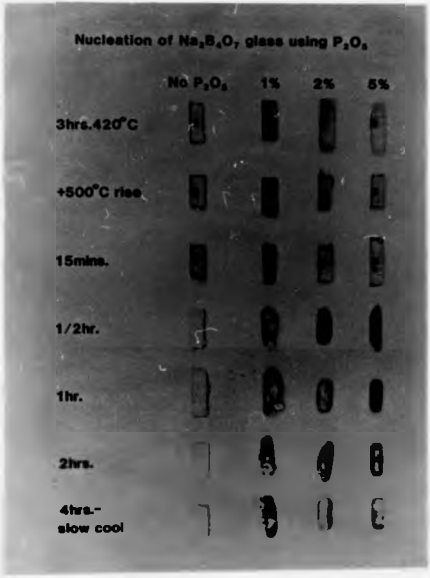

Figure 3.6.

Nucleation studies of glassy borax using TiO_2.

Figure 3.7.

Nucleation studies of glassy borax using Pt.

Figure 3.8. The effect of pre-exposure to water upon the crystallization behavior of glassy borax.

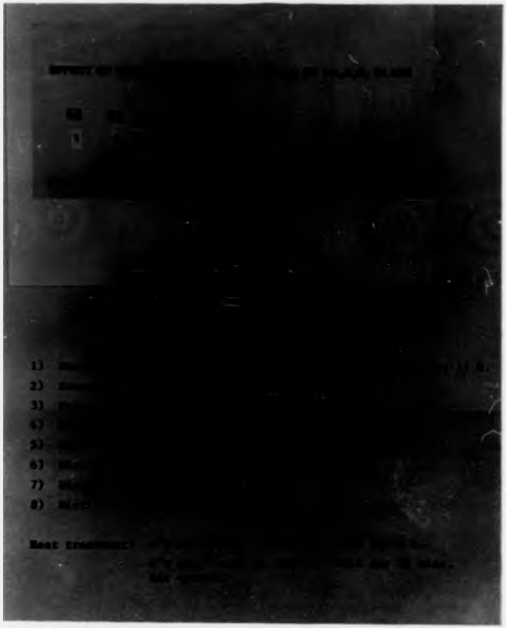

crystallisation behaviour to "as polished" specimens. Since water has a definite effect upon crystallisation (see also [164]) then the storage techniques appear to be adequate. However this data does not explain the above inconsistency.

c. Addition of 10% NaCl appears to stabilise the system, whereas further additions produced more rapid devitrification: the 30% dopant level is not truly representative, since a large piece of glass could not be formed; devitrification always occurring within the bulk upon pouring from the melt.

d. For the P_2O_5-doped specimens, it would seem that a darkening of the glass occurs as a precursor to crystallisation. The effect becomes less marked towards higher P_2O_5 concentrations, both in terms of the elapsed time in this "intermediate state", and in the final result, changing from a highly porous polycrystalline mass to a "redistributed" glassy material via a surface crystallised glass. The observed viscous flow increased the difficulty in the preparation of mechanical strength specimens.

e. In the case of TiO_2, the time at which crystallisation occurs appears to follow an approximate exponential trend with concentration.

f. For Pt, the glass stability appears to maximise at approximately 10^{-4} mol % Pt addition, in a manner analogous to the observations made using P_2O_5-nucleated specimens.

The specimens were then mounted in plastic and the polished sections examined using electron microscopy. A selection of the photographs taken are shown in Figure 3.9. Whilst the appearance is esthetically pleasing, the micrographs are not representative of the crystallisation process since a freshly polished specimen did not display these features, and must therefore be attributable to etching by atmospheric moisture.

A limited study of etch treatments was carried out using distilled water under ambient conditions for different immersion times, but as the micrographs in Figure 3.10 show, the results were not sufficiently encouraging to promote a thorough investigation of the nucleation and growth process on this basis, although similar features were apparent for very "mild" etches. Attempts to duplicate the previous effects by leaving the specimens in air were also unsuccessful.

Figure 3.9. Examples of a microscopic investigation of air-etched polished sections of borax nucleation specimens.

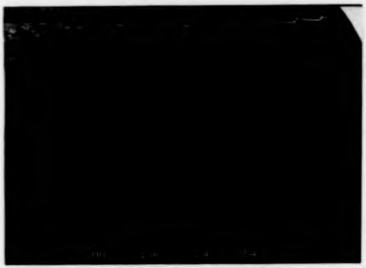

Figure 3.9a. General view.

Figure 3.9b. Closeup showing hexagonal nucleation sites with dendrites.

Figure 3.9c. Secondary nucleation from cracking.

Figure 3.10a. General view of freshly-polished specimen, for comparison.

Figure 3.10b. Closeup, showing no enhanced structure surrounding crystallites.

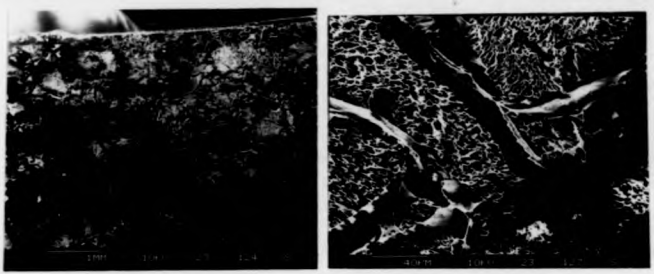

Figure 3.10c. 10min. etch.

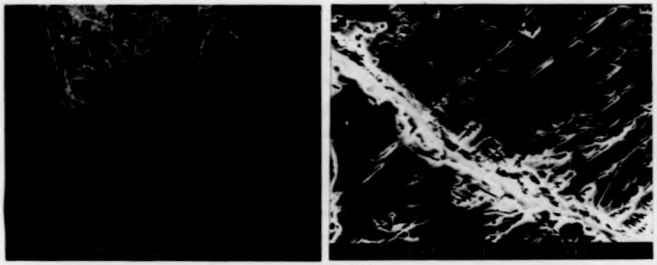

Figure 3.10d. 1min. 15s. etch.

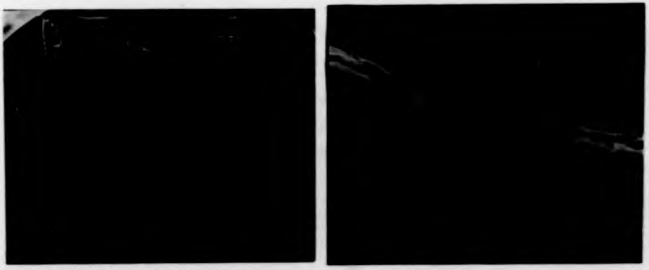

Figure 3.10e. 15s. etch.

The problems outlined above were not encountered by Daniels [9], who obtained fine grained bulk nucleated specimens for sodium chloride doped glasses using a similar heat treatment schedule.

Although nucleation tended to occur more in the bulk in these glasses, the overall resistance to finger pressure diminished compared with that of the recrystallised base glass, making preparation for strength tests more difficult.

3.1.3 Machining

To conserve materials during machining, (in order that properties from a single melt, or indeed a single block of glass might be determined), a thin (0.004 inch/~ 170 μm), diamond-coated (200 - 400 grit) high speed annular saw blade was employed for sectioning the material in an "inert" oil [179] environment. (This machine was also used to introduce the notches necessary for fracture toughness testing). Therefore, the bulk glass had to be fixed to a block using a suitable mounting wax with a melting point ~ 160°C [180]. This is a significant step in the overall thermal history of the specimens both from the point of view of stresses caused by the high thermal expansion coefficients and the low T_g values (~ 450°C) found in this glass system. (For good contact to exist between glass and wax, the glass must be raised to a temperature close to the melting point of the wax, which corresponds to ~ 60% of the absolute T_g value. By reference to the sintering criterion stated in Chapter 1, flow, and hence microscopic rearrangement, may occur at these temperatures).

After removal of the wax using 1-1-1 trichloroethane (a non-water containing solvent), the specimens were heat treated using the schedule described in section 3.1.2. However, very poor crystallisation occurred for the glasses having higher concentrations of P_2O_5 and TiO_2. Therefore an extended heat treatment schedule based on previous experience was employed to obtain higher concentrations of the crystal phase.

The TiO_2 specimens were subjected to a 3-stage heat treatment, the final stage being 4h at 590°C. This was felt unwise for the P_2O_5 containing specimens due to the flow previously observed (Fig 3.5). Therefore these specimens were held for a longer time (44 h) at the upper temperature of 500°C. The 5% doped P_2O_5 glass appeared to remain stable and so no further heat treatments were attempted for it. The specimens were then ground flat within 5×10^{-5} inch (~ 2 μm) using a Jones-Shipman surface grinder with white paraffin as lubricant (to eliminate stress corrosion effects) before fine hand polishing to 800 grit (~ 18 μm) using silicon carbide discs and an oil-based polishing fluid [181]. The criterion described in section 2.3.4 was used, and repeated on all sides. A "T" square was used to ensure 'square' faces during mounting and final checking. Any specimens found not square (by eye), or differing from the mean dimensions by $>$ 10 μm were discarded.

3.2 CONDUCTIVITY

3.2.1 Fixed Frequency Measurements

This apparatus, favoured by Borax Research Ltd., is a multi-purpose arrangement for the melting, heat treatment and conductivity measurement of glasses. A schematic of the essential features is given in Figure 3.11. The batch is first melted in the graphite crucible under an inert oxygen-free nitrogen atmosphere, and after thorough stirring using a graphite rod, the rod is placed centrally in the apparatus as indicated in the figure, to act as one electrode in the ensuing measurement stage, the other being provided by the crucible. Once the melt has cooled to a more rigid form, the drive voltage is applied and measurements initiated. The time at which measurements are begun must be considered carefully to prevent additional complications from dielectric breakdown and the possibility of electrically-induced crystallisation; both of which could arise from an unreasonably high initial measurement temperature. The process was repeated from melting for subsequent runs.

Results obtained for a series of manganese II chloride-doped borax-based glasses are shown in Figure 3.12. Direct structural interpretation is complicated by the paramagnetic nature of the manganese ion, giving rise to the capacity for electrical conduction via the overlap of the

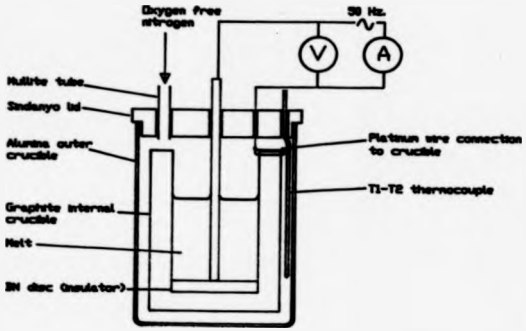

Figure 3.11.
Schematic of the conductivity arrangement used at Borax Research Ltd.
For this equipment, the resistivity ρ is given by

$$\rho = \frac{2\pi Rl}{\ln(b/a)},$$

where R is the measured resistance, l the depth of the melt, and a and b the radii of the internal and external cylinders respectively.

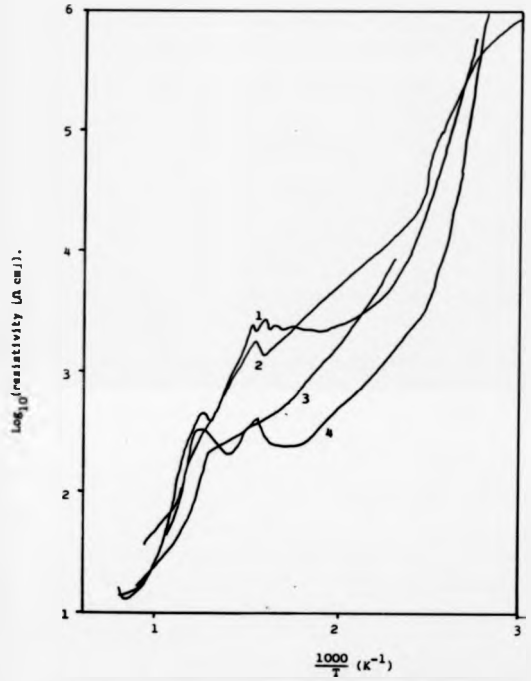

Figure 3.12 Examples of resistivity hysteresis behaviour in a $90Na_2B_4O_7.10MnCl_2$ (wt. %) melt. Run Numbers shown adjacent to curve.

3d orbitals [17]. Furthermore, the ionic conductivity contribution to the overall measured value may also be affected by the network distortion from the smaller manganese ions. This is a well-documented phenomenon known as the mixed alkali effect.

Although a quantitative parameterisation has been made by Tomandl and Schaeffer [182] using a modified Nernst-Einstein equation, the underlying physical interpretation still remains under debate. The original concept of modelling glass systems to a strong electrolyte was opposed by the excessive "blocking" requirements of the minority cation. However, by introducing a postulate of conducting pathways similar to those presented for superionic conduction, very few minority ions are required to inhibit free motion of the conducting species. Experimental evidence is available to support this latter hypothesis. A recent review reflecting current thinking and the applicability of the popular models at the time of writing has been published by Ingram [183]. A new interpretation, in terms of the strained-mixed cluster model of Goodman [14], was also presented.

As can be seen from the Arrhenius plots shown in Figure 3.12, a "hysteresis" effect is observable upon remelting, which may be in agreement with observations made on other FIC systems [20]. However, this behaviour may also be attributed to the technique itself (volatilisation losses or inaccurately assessed thermal gradients within the specimen), or perhaps a cooperative local structure rearrangement, due to a possible combination of electrically nucleated crystallisation and the "memory effect" first postulated in section 3.1.1.

The above mentioned hysteresis effect should be considered when looking at the effects of different $MnCl_2$ concentrations. Here a simple average of a series of runs has been taken to produce the plots shown in Figure 3.13. Since the activation energies obtained from this figure are ~ 0.1 eV it is only the pre-exponential factors that prevent these materials from being classified as FIC's.

The conductivity isotherms as a function of relative cation impurity shown in Figure 3.14 shows a series of maxima which would appear to preclude the possibility of ionic conduction by the mixed alkali effect, unless this system exhibits anomalous behaviour. The possibility of

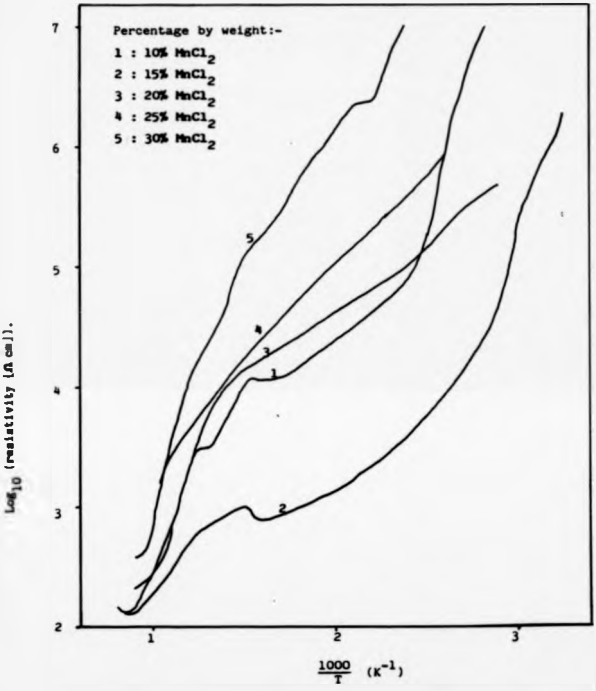

Figure 3.13 Averaged Arrhenius plots for a series of $Na_2B_4O_7$-$MnCl_2$ melts.

Figure 3.14. Variation of resistivity isotherms with manganese content for a series of $Na_2B_4O_7$-$MnCl_2$ melts.

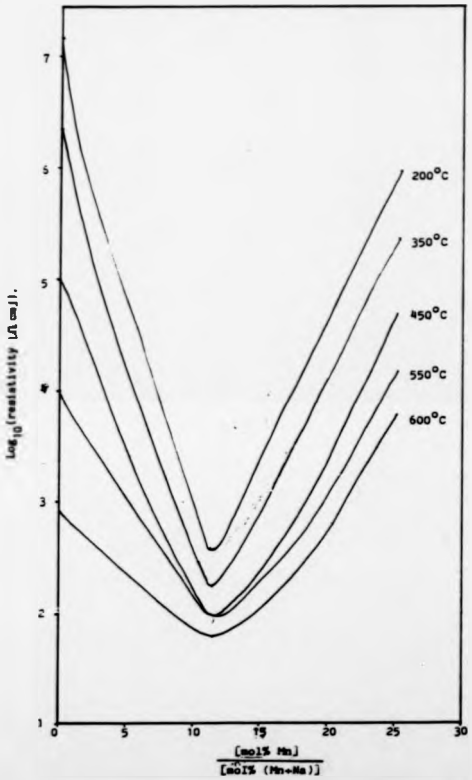

electronic conduction is apparent via the overlap of the 3d electrons in the manganese ions, which is responsible for the ferromagnetic behaviour in manganese metal [17]. The verification of electronic conduction could have been performed by electron spin resonance (ESR) or a Tubandt experiment (section 3.2.4), but these techniques were not available for experimentation. Further investigations of this glass system were impeded by the possibility of free manganese metal in the molten glass forming an amalgam with the platinum-based crucibles used for melting and D.T.A. Glass preparation in graphite or alumina crucibles used at Borax Research Ltd. was thought to be impractical due to dissolution of the crucible materials into the melt, thereby changing the measured properties. This would not be readily observable in the case of alumina, whereas platinum dissolution, for example, is highlighted by a grey discolouration in the final glass.

Additional information from other macroscopic techniques was not obtained due to the observed inhomogeneity of the samples when finally poured. The cause of this was the inclusion of small white lumps of boron nitride powder arising from the break up of the insulating disc. NMR was considered impractical due to the short T_1 caused by the high concentrations of paramagnetic ions in the specimen [73].

3.2.2 Time Domain Techniques

This technique, as with all the following conductivity techniques to be described here, favours the evaluation of the electrical properties of a machined block of material having a well-known thermal history.

The measurement system comprised a virtual earth amplifier in a capacitor compensated feedback circuit, having a detection limit of 10^{-13} A. The capacitor was used primarily for 'tuning' purposes by minimising the time constant of the measured current decay, to make a first order correction for the capacitance inherent in the system, although 'pure resistive' behaviour could not hope to be achieved due to the additional capacitances associated with the relaxation mechanisms within the specimen itself. This may be visualised by reference to the equivalent circuit representation of the system presented in sections 2.2.1b and 2.2.1c.

To provide an estimate of the equivalence of the specimen response to different polarity voltages, the drive voltage was switched at a rate determined by an externally applied "clock" and the current flow in each direction measured. The clock input was taken from the square wave output of a signal generator. To obtain more meaningful data by waiting for longer times before reading the asymptotic "d.c." current flowing, the input was used to clock an 8-bit counter, the output from which was used to trigger the applied polarity switch (i.e. divide the frequency by 256). Despite this, the voltage in a given direction was only applied for ~ 6 s.

As stated above, the detection limit of the amplifier was 10^{-13} A, which when considered with respect to the 10 V drive voltage and typical specimen dimensions, gave an upper resistivity limit of $< 10^{15}$ Ω cm, although values in excess of this have been reported [184]. The attainment and assessment of the lower resistivity limit required to examine the more highly conducting glass-ceramic, however, posed more difficult problems. In the first instance, the full scale measured current was decreased to a sensitivity of 10^{-8} A, whereupon the "resistance" sensitivity was changed by decreasing the drive voltage. Non-linear effects were not observed for the measured specimens, shown by later modifications to provide control over applied voltage and f.s.d. current in the intermediate current-gain region, and the initial gain of the preamp.

The criteria governing the size of the electrodes applied to the specimen followed as closely as possible the work performed by Amey and Hamburger [185]:

$$r_1/h \geq 2$$

$$(r_3 - r_2)/h \geq 2 \qquad (3.3)$$

$$D/r_0 \leq \tfrac{1}{4},$$

for the arrangement given in Figure 3.15. This leads to the analytical expression for the bulk resistance R:

$$R = \frac{h\rho}{(r_0 - \frac{2h}{\pi}\ln(\cosh\frac{\pi D}{2h}))^2} \qquad (3.4)$$

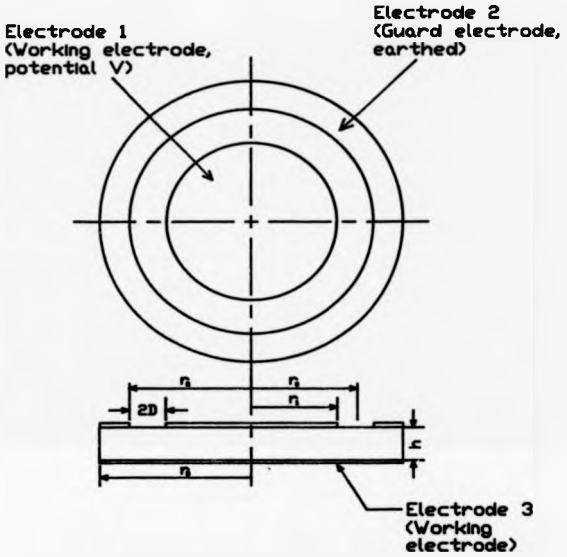

Figure 3.15.
Electrode geometry
presented by Amey &
Hamburger [185]

from which the volume resistivity ρ may be obtained. However, upon consideration of the physical characteristics of some of the specimens (i.e. the poor nucleation properties of the devitrified material), these conditions were violated by choosing large specimen thicknesses. The reason for this was that the measurements performed on the devitrified materials would be more physically meaningful if the measured current has flowed through a distance of more than one crystal (spherulite) diameter. Unfortunately the existing cell would not permit larger diameter specimens to be used to obey the criteria in equation 3.3. Therefore the specimen resistivity was calculated assuming an approximate electrode area, of the mean between drive and working electrodes,

$$\rho = \frac{\pi R(r_1 + r_2)^2}{h} \qquad (3.5)$$

The essential features of the working conductivity rig are illustrated in Figure 3.15. Although the system voltages appear to be well isolated electrically, a significant noise problem was apparent, as could be readily observed by the wild oscillations of the front panel moving coil meter, when the initial maximum gain setting ($\approx 10^{13}$) was used. This persisted, despite painstaking and time consuming efforts to eliminate this by electrostatic screening and the isolation of possibly more distant sources of noise. The most obvious source of noise, namely the furnace and controller, were found to be remarkably noise free, the furnace comprising a well-made commercial non-inductively wound element. The eventual cause was attributed to the amplifier itself, since it has a minimum input current requirement ($\sim 10^{-14}$ A), below which it will cease to operate. Therefore the maximum practical resistivity measurement was taken to be $\leq 10^{14}$ Ω cm.

To maintain consistency with earlier work, the electrodes applied to the specimen were of sputtered gold, followed by a layer of painted silver dag to reduce the mechanical surface damage sustained during loading and unloading.

Results obtained from this arrangement were compared with a "standard", taken to be Pilkington's float glass. The agreement obtained from a number of heating and cooling cycles is

shown in Figure 3.16. Encouraged by this, further experiments were performed on the previously characterised CaB_4O_7-$CaCl_2$ system of materials. For the glasses, good agreement was indeed obtained, but a systematic decrease in resistivity values for the first measured glass-ceramic was seen with each subsequent run, as shown in Figure 3.17, the material having changed colour from white to grey-white upon removal. This was attributed to silver ion diffusion along the grain boundaries but an Energy-Dispersive X-ray Analysis (EDAX) in the SEM of the sectioned specimen showed negligible silver content with increasing depth into the sample, as shown in Figure 3.18. Previous work had shown an apparently random "hysteresis" effect with successive runs [9], once again in keeping with well-documented FIC systems [20]. Unfortunately, a repeat experiment using sputtered gold only as the electrode material resulted in the absence of an exponential current decay, the current no longer attaining an asymptotic equilibrium value at long times (Figure 3.19a). This was thought to be due to the "discharge" of a second capacitive element in the equivalent circuit, and so the decision was taken to modify the existing measurement system to monitor this feature more fully, with the object of analysis using standard time-domain techniques [34].

Since the analysis of the current decay requires a Laplace transform, the decay was provisionally measured with a chart recorder, with the view to transferring to full digital acquisition in the event of sufficiently encouraging results using a BBC microcomputer with either a fast external A/D converter connected to the 1 MHz bus or its own, somewhat slower, internal A/D's. For the float glass standard, traces similar to the schematic in Figure 3.19a were obtained showing the "charging" process inferred above. Therefore, an "earth step" was introduced to the voltage sequence in an effort to discharge the capacitance, with the result shown in Figure 3.19b. This produced the expected exponential decay for the measurement stages over the working temperature range, which could be qualitatively fitted to the response of an equivalent circuit comprising two parallel R-C networks, the analysis for which is reproduced in Appendix 1. The preliminary analysis indicated in Figure 3.20 was only performed at lower temperatures since the larger "d.c." level did not permit sufficient resolution of the current decay towards higher temperatures. However, when the specimen was replaced by the "rogue" glass-ceramic sample, the previously observed "secondary capacitance discharge" was

Figure 3.16. Arrhenius plots for Pilkington's float glass (used as a standard in the "d.c." and time domain spectroscopy measurements).

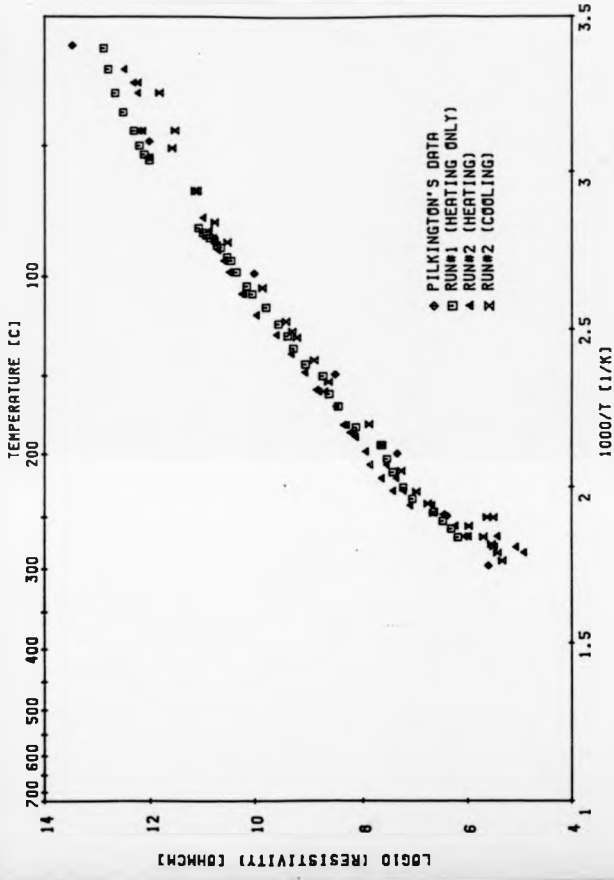

Figure 3.17. Arrhenius plots for a $90CaB_2O_7.10CaCl_2$ glass-ceramic with silver paste electrodes.

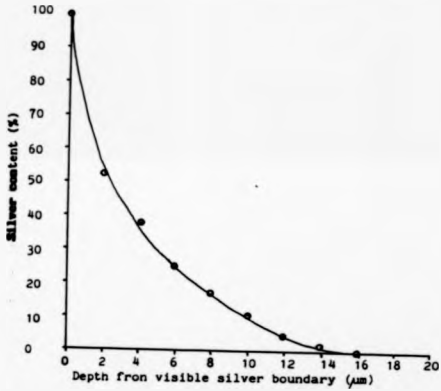

Figure 3.18. Variation of silver content with depth for a glass-ceramic specimen coated with silver paint during a series of conductivity measurements.

Figure 3.19. Schematic diagram of the measured time dependences of current flowing during a "d.c." conductivity measurement for a given applied voltage sequence.

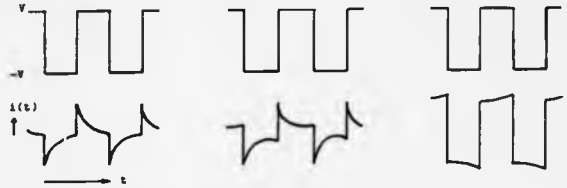

Figure 3.19a. Glass-ceramic specimen, 2 stage potential function.

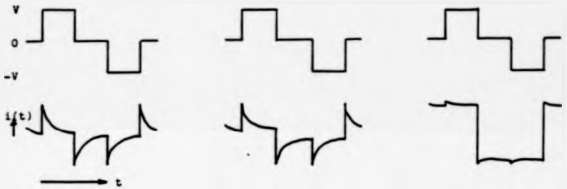

Figure 3.19b. Pilkington's float glass, 4 stage periodic potential.

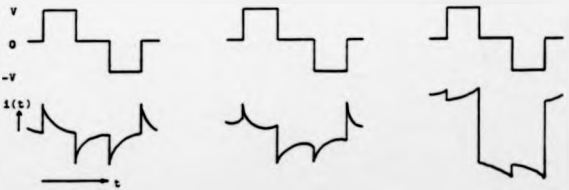

Figure 3.19c. Glass-ceramic specimen, 4 stage periodic potential.

Increasing temperature

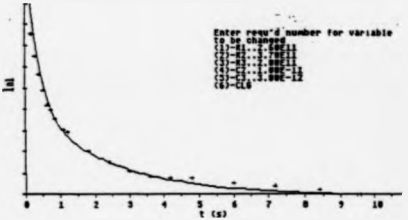

Float glass 23°C. Low frequency region fitted very well, although modifications do not lead to better overall agreement.

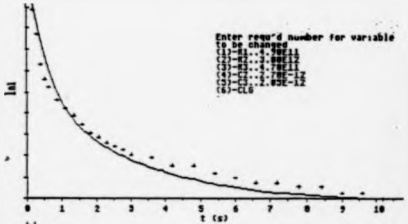

Float glass 23°C. Here, high frequency decay is fitted well, disregarding low frequency effects. Resistance and capacitance values show agreement in part with 4(a), but it is felt that a three-part equivalent circuit at least is required to obtain good overall agreement.

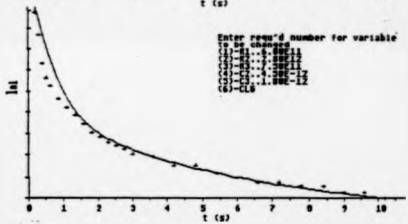

Float glass 40°C. Good overall fit, suggesting that the electrode contributions have merged. Values obtained would appear to agree with previous determinations.

Figure 3.20. Illustration of some data fitting trials from time domain studies of Pilkington's float glass.

reproduced, shown schematically in Figure 3.19c. Various modelling strategies were attempted to duplicate this phenomenon on a computer, but without success.

Two options were now apparent to further this investigation, both of which were time consuming:

1. To further modify the existing rig to a complete time-domain setup as indicated above, with a fast A-D converter and on-board RAM to obtain the response very soon after the initial voltage pulse, (since the BBC computer contains insufficient memory for the projected size of the acquired data (40 K bytes)) combined with a dedicated microprocessor for input/output and decisions regarding conversion rates (fewer measurements required at longer times). Furthermore, new software would have to be developed to model and analyze this data. It must also be realised that such an unusual response, the like of which does not appear to have been reported in the literature, may be a characteristic of the cell or the measurement system.

2. To build a completely new frequency domain oriented measurement system.

In view of the complexity required to further modify the "old" system, the decision was made to sacrifice the insight that time domain spectroscopy may offer in the attainment of "d.c." conductivity values, in favour of the easier interpretation afforded by a frequency domain system, with the intention to return to this current arrangement if the results from the new system provide a possible explanation for this anomaly and time constraints permit.

3.2.3 Frequency Domain Dielectric Spectroscopy

Prior to the design of the equipment described here, comparison was made of three conductivity measurement systems, all of which employ different aspects of the acquisition techniques embodied in the complex admittance method, and so exhibit varied cell geometry and temperature control mechanisms. This was carried out in order that the optimum features may be chosen and incorporated into the final design, where possible.

These rigs were based in active University research groups, at the Royal School of Mines, Imperial College, led by Professor B.C.H. Steele, the Department of Glasses, Ceramics and Polymers at the University of Sheffield, led by Professor J.O. Isard, and the Department of Physics at the University of Warwick, led by Dr. M.J.A. Smith.

The essential features of the arrangements are summarised briefly below:

At Imperial College, the cell is constructed entirely of recrystallised alumina (Al_2O_3), and lies on a horizontal plane. The specimen is held vertically on the supporting base of the external screening by a delicate platinum spring-loaded contact, which serves the dual purpose of the drive and measurement electrodes. After fitting the outer alumina heat shield, the assembly is fed into a horizontal tube furnace. The result is a compact cell with a low thermal mass, which would require careful estimation of the thermal gradients and accurate temperature control for measurement stability. The electrodes applied to the specimens, mainly oriented towards FICs such as zirconia (ZrO_2, an oxygen ion conductor) and zeolites, were of platinum applied as an organometallic paint and fired at ~ 500°C to leave a metallic surface layer. The screening around the lead-throughs for the connecting wires was achieved in the same way.

The conductivity was measured, displayed and preprocessed for several simple equivalent circuits by a Zilog Z80 microprocessor interfaced with a Solartron 1174 frequency response analyser, having a working frequency of 0.1 mHz to 10 MHz.

This differed from the setup adopted at Sheffield in that the emphasis placed here was upon overall thermal stability. The cell material was oxidation resistant stainless steel, with vitreous silica spacers as the electrical insulating material. Having a larger thermal mass and conductivity, temperature stability presented less of a problem. The deployment of spring-loaded contacts for the external electrode connections was again in existence, although this time a vertical cell was used. Measurements were performed by a bridge-based technique, requiring careful tuning for each reading, becoming more time-consuming at lower frequencies. However the results from this system are probably more relevant to the current work since superionic lithium phosphate-based glasses were investigated.

Finally the Warwick system, in the author's opinion one of the most versatile and accurate available [203], comprises some complexity in its current developmental state. Since the materials under investigation are mainly polymer dielectrics for the semiconductor industry, lower measurement temperatures (~ -200° C - 350° C) are required and so the main constructional material is brass. The initial in and out of phase signals ("0" and "90") are tuned using a "dummy" cell that is mechanically and electrically similar to the actual measurement cell. The output obtained from the measurement cell due to an initial "0" signal is subsequently balanced with the appropriate proportions of the "0" and "90" standards using a variable air gap capacitor to obtain a "null" at the measurement frequency.

The temperature control system is equally complex, using pure nitrogen gas (the forced boil-off from a liquid nitrogen dewar) heated to the desired temperature prior to passing through the cells, to obtain good temperature uniformity and noise reduction from furnace windings.

These and other groups were approached to perform selected readings prior to construction of the ultimate cell, but unfortunately the equipment was unavailable for various reasons.

Therefore the system had to be built without the benefit of experience with other working versions. In order to reduce "teething troubles", it was decided to attempt to optimise working efficiency with mechanical and electrical simplicity using experience gained from the construction and modification of parts of the other measurement system. As a result, the final plan was a cell of the form shown in Figure 3.21, oriented strongly towards the Sheffield system, to be driven from a second-hand Solartron 1172 frequency response analyser (frequency range 0.1 mHz - 10 kHz) connected to a BBC microcomputer to handle the large amount of data produced, which formed the basis of the setup at Imperial College. Some of the screening techniques in this plan were also incorporated from the Imperial College design.

To construct the cell, oxidation resistant stainless steel type 08468 was used for the main body, and vitreous silica, kindly donated by Heraeus Silica and Metals Ltd., for the insulating spacers. The silica cylinders were machined to size using an Elliot No. 5 centreless rotary

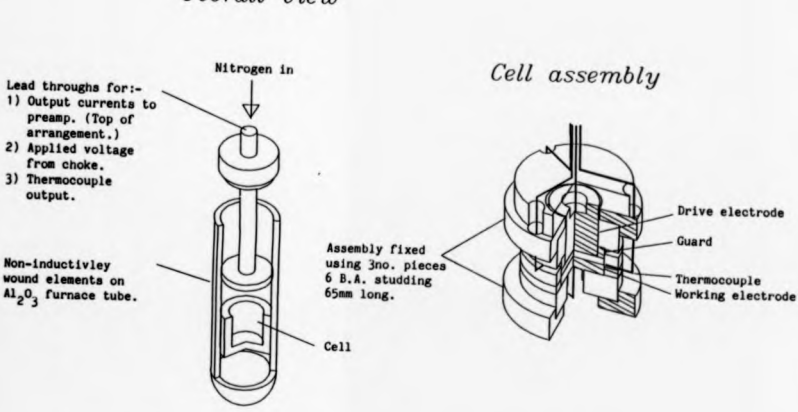

Figure 3.21. Schematic of F.R.A. apparatus.

grinder, for which a collet had to be made to hold the hollow diamond drill bits used to drill the central holes sufficiently accurately prior to internal grinding. After machining, all horizontal faces were surface ground flat to obtain well-defined electrode contact areas in the final assembly. The spring loaded contact for the drive electrode was manufactured using a nimonic steel by Springs of Coventry Ltd. and has an upper working temperature of 500°C.

Connections were made to the preamp. using 28 S.W.G. Ni-Cr wire, shielded in thermally recrystallised alumina tubing. In order to reduce noise, this was initially screened using organometallic platinum paint (donated by Engelhard Ltd. and Heraeus Silica and Metals Ltd.) as seen at Imperial College. This was later found to be unsatisfactory due to the persistance of interference from surface conductivity variations and earth loops at the tube connections. A simpler solution was to enclose the lead throughs in an earthed stainless steel tube right through to the base of the preamp. The drive voltage was supplied in a separate lead through outside the arrangement, the support for these connections supplied by the thermocouple housing, which fixed the position of the outer alumina tubes and acted to reduce the temperature gradient over the outer screened stainless steel tube.

Following the first high temperature trials, the silica spacers were found to have shattered from the stresses created by the higher expansion of the inner steel electrodes. Since the silica provided a means of centralising the electrodes as well as electrically isolating them, no compromise in radial dimension could be made. Instead, the newly machined spacers were sectioned into four equal parts to allow free expansion of the system upon heating, which may have sacrificed the upper resistance limit from increased surface conductivity.

It was also found essential to further modify the Sheffield design [45] by eliminating the thin-walled drive-guard insulating and centralising collar. This had been found to be exceptionally difficult to machine to the required tolerances and much more susceptible to fracture from the previously mentioned thermal expansion mismatch. Therefore the new sectioned spacers were modified to centre both electrodes using a recess on the lower face.

The electrical pickup in the measurement system comprised both low and high frequency components. The high frequency noise, from the 1172's internal clock, was isolated using a choke, which caused amplitude and phase changes to the "cleaned" output signal. Therefore the output was split to drive the cell, and act as a feedback input for subsequent measurement.

The low frequency mains pickup was caused by oscillation of the mains earth from nearby heavy electrical equipment, and eliminated by referencing the entire experiment to the same earth. This comprised taking all electrical power from a single 3-pin mains socket, and connecting the earth at this point to a baseplane, thereby forcing all equipment to exhibit the same in-phase disturbance and so preventing amplification of this into the processed data.

Surprisingly, perhaps, the home-made alumina tube furnace did not contribute to this noise. The central tube had been wound non-inductively with about 20 turns of 18 gauge Ni-Cr wire using twin bore mullite spacers prior to firing. "Triest" cement on the outside to fix the windings in position. This was then surrounded by a vermiculite packing in a water-cooled steel jacket, to provide a high overall thermal mass, and hence good temperature stability.

The PRA was connected to a computer in view of the number and sporadic acquisition time of the measured data points, and to optimise the measurement time in general. This could be achieved in one of two ways. The first was to computer control the entire experiment using an IEEE-488 bus system, however the cost of the interface to the machines was prohibitively high. The other alternative was to use the 1180 plotter interface supplied for measurement output, and configure the computer in a "listen only" mode. Data was obtained in this way using the internal 12-bit A-D converters in the BBC, with eight measurements taken of each data point to improve statistics. The measurement sequence can be understood by reference to the timing diagram in Figure 3.22. Absolute values were calculated from the calibration of the plotter interface performed prior to each frequency scan, and the front panel settings of the 1180 entered at the keyboard. A BASIC program was written to read data in any of the three standard formats afforded by the 1180. These "formats" are indicative of the three ways of representing a complex vector, shown in Figure 3.23. As may be readily appreciated, the

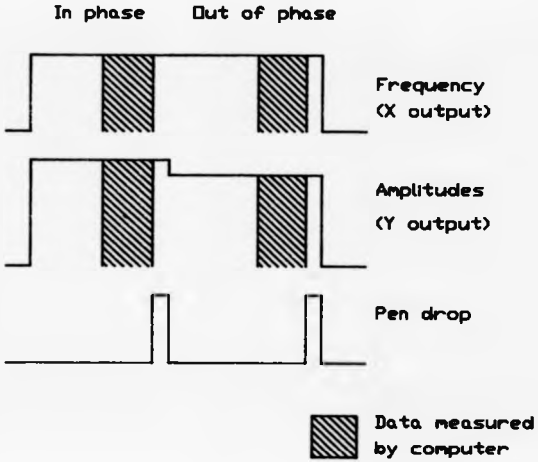

Figure 3.22.
Timing diagram indicating measurement periods for the BBC microcomputer acquiring analogue data from a Solartron 1180 plotter interface.

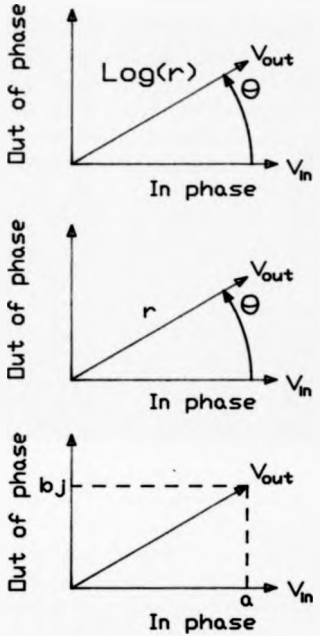

Figure 3.23.
Various representations of input and output voltages in a.c. measurements.

temperature stability of the cell during the lengthy measurement sequence must be assessed. This was accomplished by monitoring the output from a simple op-amp on a fourth input to the A-D at the start and finish of the measurement, and converted to a temperature reading via a simple BASIC algorithm. The data files generated in this manner were then plotted using a general program on a DIGI-PLOT A3 flatbed plotter, and ASCII versions generated for input to a FORTRAN77 optimisation program to produce the "best fit" equivalent circuit parameters for a selection of simple, yet physically realistic circuits illustrated in Appendix 1, along with their associated impedances. These were calculated using simple a.c. theory [91].

Interpretation of the data was based upon Cole-Cole plots. Whilst other methods (for example, evaluation of the complex modulus [43]) provide greater sensitivity towards other aspects of the equivalent circuit, these were not investigated for the time being, since results from the experiments presented here must form part of an overall equipment and data fitting appraisal. As such, more specific investigations of the relaxations present were not felt to be instructive.

The underlying reason for data processing in terms of impedance rather than permittivity is that much of the current literature appears to be perplexed by the phenomenon of depressed and distorted semicircles in complex permittivity plots. These are generally attributed to a distribution of relaxation mechanisms in the bulk sample under test. However, this analysis is felt here to be unnecessarily complicated, since it can be shown (Figure 3.24) that a simple combination of discrete passive components is capable of producing similar loci in the complex plane. The subsequent assumptions of the contact area of the electrodes and the specimen thickness can then be introduced to form the complex permittivity data necessary to compare results from different specimens.

In order to examine the practical ramifications of this hypothesis and test the performance of the equipment a test circuit comprising two parallel R-C units having different time constants was constructed. The results are shown together with the theoretical and optimised curve in Figure 3.25.

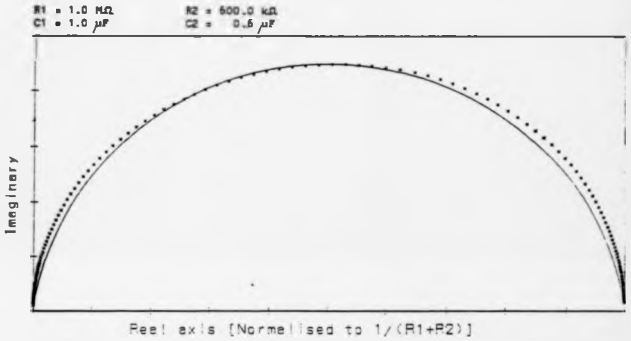

Figure 3.24. Theoretical Cole-Cole plot illustrating the phenomenon of depressed semicircles for a combination of discrete electrical components.

Figure 3.25. Cole-Cole plot for the test circuit used as a check of equipment performance. Optimised fit is shown as the dashed red line. The mismatch function is shown below as a continuous red line, offset from the fit.

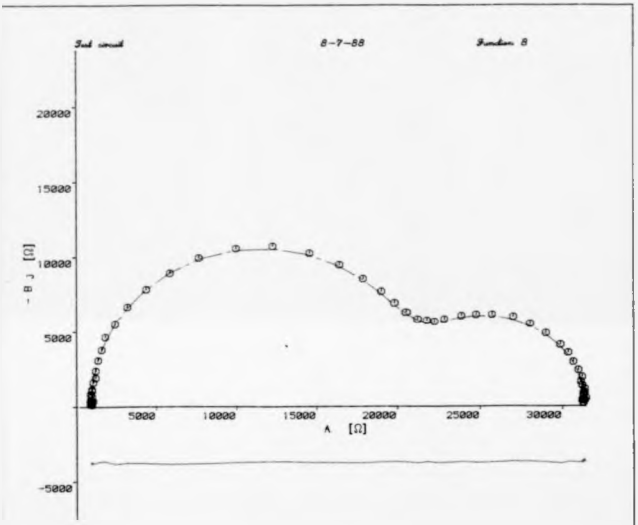

Calculated values
for function 8

Resistance		Capacitance	
10.2	kΩ	10	μF
20	kΩ	0.2	μF
890	Ω		

In order to establish that the best values had been obtained, the parameters produced by each optimisation were resubmitted to the program until the output values remained consistent. This process required only two runs in general. The initial "seed" values were obtained by fitting the data manually in the first instance, but significant savings in time were obtained for temperature varying data and compositionally similar specimens by taking the optimised values from a previous temperature/similar specimen at the same temperature, and using these as the seeds for the current analysis.

Excellent agreement between the raw data and the fit (shown as the dashed red line in the figure) can be seen, although a series resistance had to be introduced into the "black box" to obtain the observed goodness of fit*. The reason for this was that the experimental impedance values were obtained by an inferred current measurement, namely the measurement of the voltage across a standard resistor. This in turn influenced the response of the test circuit.

It should be possible to exclude the series resistance from the equivalent circuit when fitting data obtained from actual specimens, since current is converted directly into a voltage input to the 1172 by a virtual earth amplifier.

The next test of the experimental arrangement was to examine Coors alumina AD-96, a standard material used for device packaging.

The electrode material for this and all other specimens was eventually chosen to be vacuum evaporated graphite. In order to ensure clearly defined initial electrode contact areas, a series of mild steel "masks" were fabricated with appropriate aligning aids. Sputtered gold and organometallic platinum were found to diffuse into the specimen upon heating, since the coatings were no longer observable upon post measurement removal.

---

* A measure of the fit may be obtained by inspection of the low deviation of the "mismatch function" (the difference between fit and raw data, shown below the "real" axis as a solid red line) from its mean value of zero.

Good agreement between experiment and optimised fit were still in evidence, as shown by a typical example in Figure 3.26. The correlation between the two is, however, slightly worse than that obtained for the test circuit, illustrated by the increased deviation and discontinuity of the mismatch function from its mean value. It should also be pointed out that some data points having excessively high deviations from the general continuity of the data had to be removed to enable consistent data fitting. This is partially justified since the 1172 does not indicate that the input voltages may be too small to be measured; it simply produces random output. No more than 5 data points were removed from a single data set containing 50 measurements.

Examination of the component values obtained show conclusively that the "electronic resistance" and "double layer capacitance" components introduced into the equivalent circuit are far greater ($> 10^3$) than the values which describe the experimental data accurately. The optimisation routine is therefore unable to parameterise the effects of these components with any degree of certainty. This conclusion is in agreement with other experimental work, since the electronic conductivity of the alumina substrate is found to be negligible [186], and the graphite electrodes employed here should be perfectly blocking. The component values determined were then processed to obtain material parameters, namely the specimen resistivity and the relative permittivity, obtained by correcting the capacitance values for the effect of a dimensionally equivalent air gap capacitor [96]. These values are presented in Arrhenius form in Figures 3.27 and 3.28, together with Coors' data [186] for comparison. The resistivity plot contains 3 sets of data points, the values being obtained from the two "fitted" components, and their arithmetic sum. The summed values correlate well with values obtained geometrically, assuming a single relaxation mechanism, from the point at which the "semicircular" arc cuts the in phase (real) axis (i.e. the plateau in the dispersion curve, Figure 2.4). This point is concurrent with the lowest frequency data points for the specimens examined in the current work.

The permittivity data, however, is more difficult to rationalise: values obtained from a modelling strategy having the adopted "polycrystalline" ceramic equivalent circuit (Figure 2.5) can be seen to be excessively high ($\sim 10^3$), whilst a secondary calculation, based on a geometric analysis assuming a single relaxation ($\omega = 1/RC$), leads to values comparable with those of

Figure 3.26. Typical data obtained from a Coors alumina substrate, presented in Cole-Cole form. The optimised fit and mismatch function are also indicated.

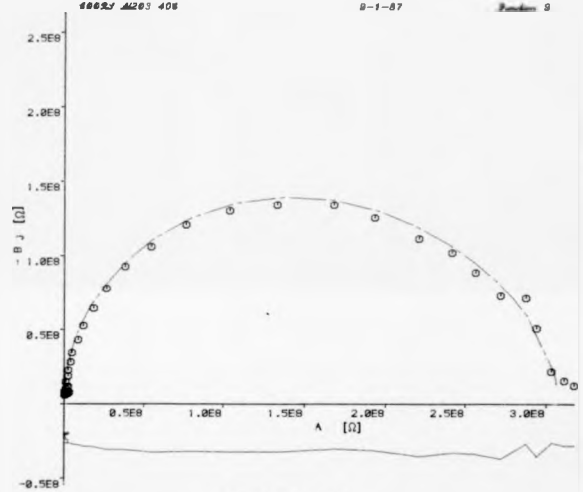

Calculated values
for function 9

Resistance		Capacitance	
58	MΩ	0.08	μF
240	MΩ	5	nF
2000	GΩ	3	nF

Figure 3.27. Arrhenius plot of resistivity of a Coors alumina ceramic substrate. (Standard to test the range and accuracy of the frequency domain measurement system.)

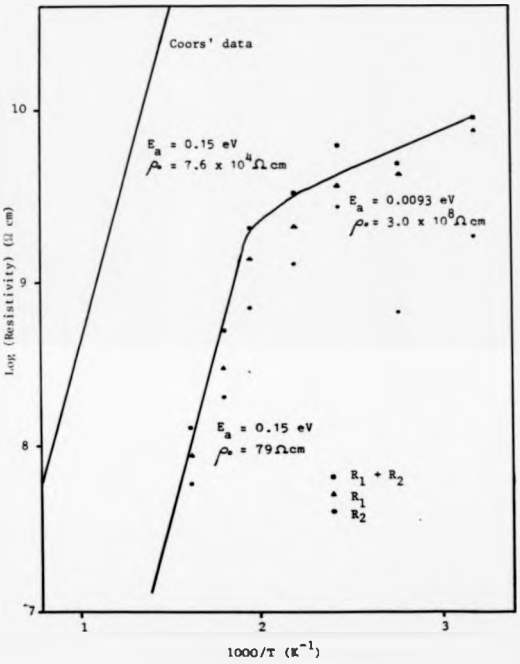

Figure 3.28. Arrhenius plot of (capacitative) permittivity of a Coors alumina ceramic substrate using an optimisation program with a modelling strategy based on two distinct relaxation mechanisms.

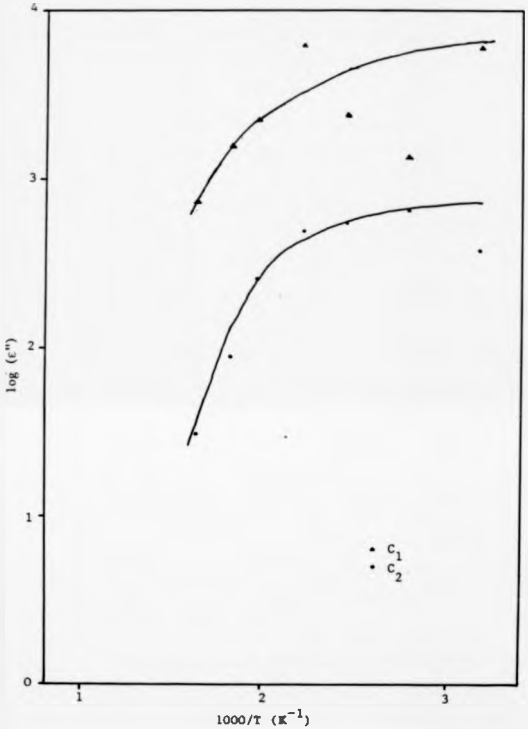

Coors' data (-1). The theoretical fit using the optimised values, however, do correlate well with the experimental data. It is difficult to assimilate these two component value determinations. Combination of the values obtained for two relaxations to derive an equivalent value for a single relaxation seems, to the author, intractable.

Even so, the values obtained here are consistently lower than Coors' data, which may be due to incomplete elimination of surface conduction or the presence of residual atmospheric moisture. If this latter hypothesis were correct, a sudden resistivity increase would be expected once the measurement temperature exceeded ~ 100°C. The low temperature tail off could indicate the upper resistivity limit of the apparatus, which would be considerably worse than the calculated limit of > 10^{13} Ω cm for this specimen.

If this result is indeed indicative of the upper limit of the measurement system, then this should not be deliterious to the specimens under investigation here, since values for similar glasses reported elsewhere indicate measurable resistivities lower than this 10^{13} Ω cm ceiling.

Additional problems were also encountered with the sodium chloride-doped glasses: the expected "semicircular" arcs were not obtained. Although the sample trace presented in Figure 3.29a converges towards the "real" axis, it is unclear how this trace could form a (depressed) semicircular arc similar to those presented in the literature. It would appear that these loci would cut the "real" axis a second time at a negative value of resistance, or form a locus with a maximum "imaginary" value greater than that for a semicircle (i.e. > R/2), both of which are contrary to accepted theories. There seems to be no simple explanation for this behaviour both from the viewpoint of a physical interpretation and of an irregular experimental measurement. Further experimental investigations are essential, but were not possible due to external demands upon the equipment.

Therefore, to obtain a "flavour" for the relaxation behaviour, the limiting impedance values (having a "plateau" in the dispersion curve) were used in the Arrhenius plots presented in Figure 3.29b.

Figure 3.29a. Cole-Cole impedance plot illustrating the anomalous loci observed for a $95Na_2B_4O_7.5NaCl$ glass, typical of the responses obtained for the glassy materials investigated in this work.

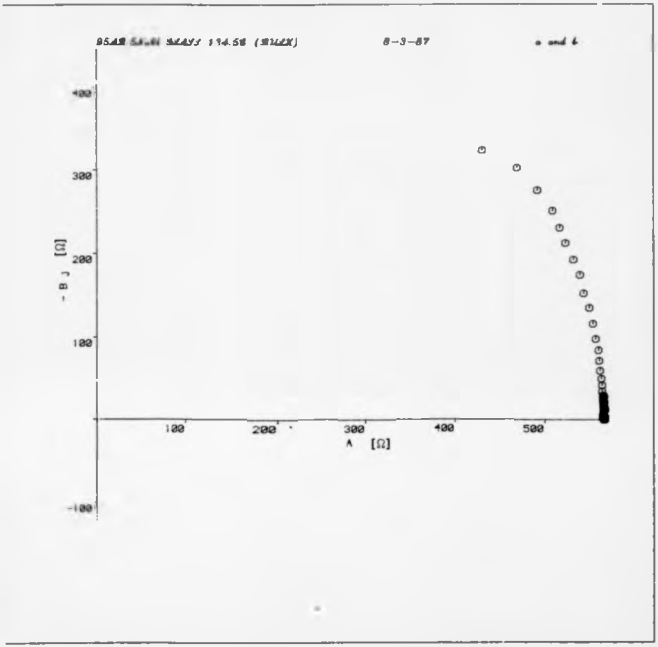

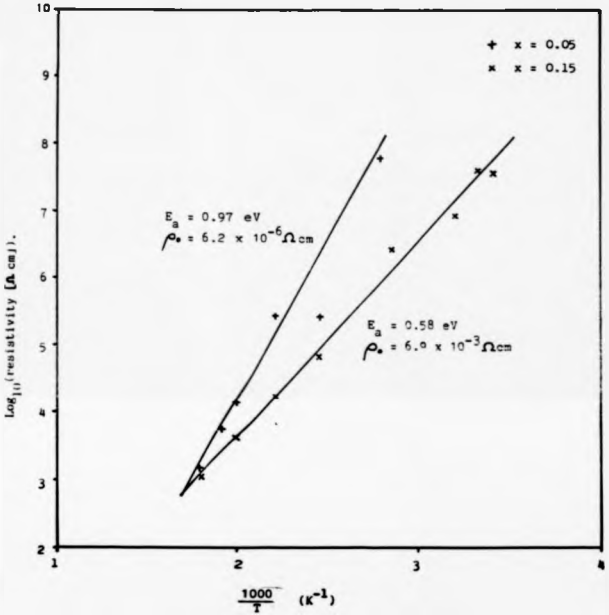

Figure 3.29b. Arrhenium plots for glassy specimens of general formula (1-x) $Na_2B_4O_7$. x NaCl.

The parameter x is a measure of the molar concentration of NaCl included in the base glass.

Figure 3.30. Cole-Cole plot for an $80Na_2B_4O_7.20NaCl$ glass-ceramic 38°C. 10V input. Run 2

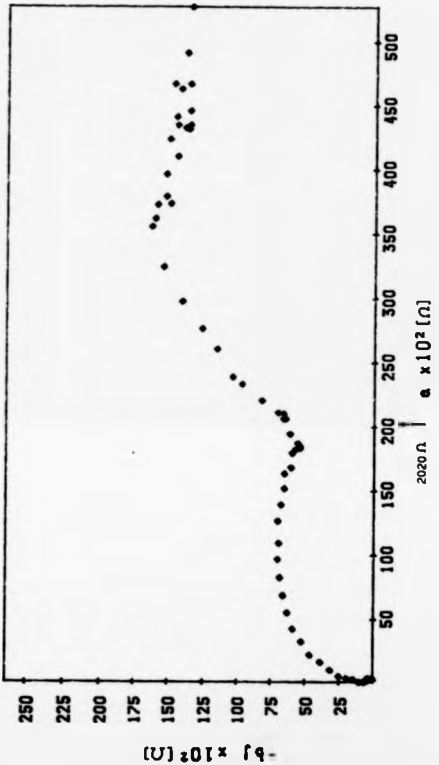

The resistivity values are lower than expected for glassy borax, but show a decrease in the intercept ρ_0 and activation energy for increasing halide content in agreement with work performed by Daniels [9].

Turning attention to the single glass-ceramic specimen investigated in this work, the base glass having a starting composition $80Na_2B_4O_7.20NaCl$, additional anomalies are revealed. In the first run, the expected "semicircular" loci were produced, as shown in Figure 3.30.

However with subsequent runs, unusual behaviour in the frequency dispersion curve was obtained, which is probably best demonstrated by reference to the Cole-Cole plots shown in Figures 3.30 - 3.32. From a "standard" distorted semicircle (Figure 3.30), a classic Warburg impedance results (Figure 3.31), which is further modified to include a "loop" as shown in Figure 3.32. A basic text on electrochemistry [187] interprets this behaviour as being indicative of electrode reactions. However the electrodes themselves are carbonised oxidation resistant stainless steel on top of the vapour deposited graphite in contact with the specimen under investigation. Although the steel above the specimen was seen to be discoloured upon dismantling the cell following measurement, the seal between the vapour deposited layer and the carbon paint was macroscopically sound, the specimen having to be separated from the steel electrodes by dissolution of the carbon paint using 1-1-1 trichloroethane in an ultrasonic bath. The reaction can only be postulated to occur beneath the surface of the specimen, possibly with water. This appears to be unlikely since the sample remained in situ throughout the measurement consistently in an oxygen-free nitrogen environment. Since the steel was discoloured, however, then this probably arose from the low oxygen level impurity within the gas, and so the specimen could have correspondingly picked up water. Further investigations on this and other materials in this system and determination of the conduction pathways are necessary before more useful definitive conclusions can be made.

Again, to obtain an indication of the material properties, resistance values were obtained geometrically using the method described in the majority of available literature, which is described briefly above. Since the Cole-Cole plots are not representative of the well-defined relaxations presented earlier, the values were obtained from the point at which an interpolated

Figure 3.31. Cole - Cole plot for an $80Na_2B_4O_7.20NaCl$ glass-ceramic 181°C.IV input. Run 2

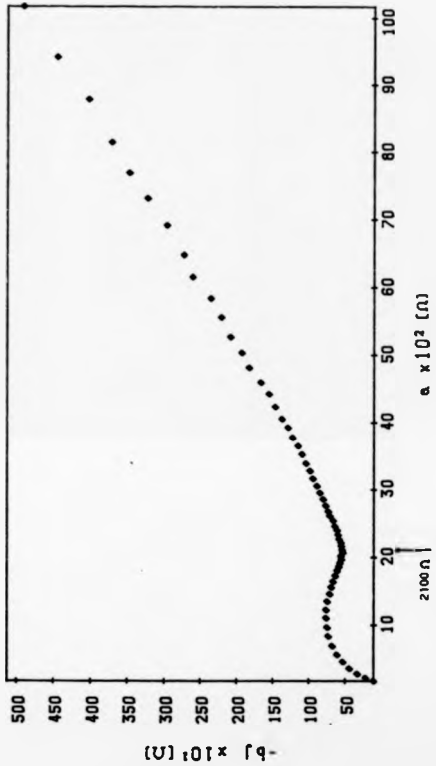

Figure 3.32. Cole - Cole plot for an $80Na_2B_4O_7.2NaCl$ glass-ceramic 139°C. IV input. Run 3

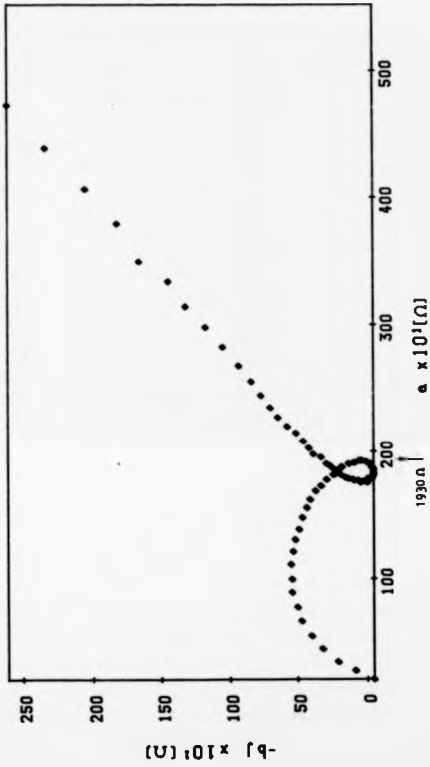

arc cuts the "real" axis, at the points indicated in Figures 3.30-3.32. The processed resistivity values are displayed in Arrhenius form in Figure 3.33. A high degree of reproducibility within experimental scatter is demonstrated. Furthermore, a previously observed "hysteresis" effect [9, 170] can be inferred by reference to the figure. However, in a more quantitative evaluation of the results, there are two possible fits available, which are shown on the figure. Fit (1) is indicative of the onset of an additional vacancy assisted conduction mechanism, for example, impurity based conduction (reference [96] p. 455). Fit (2) is reminiscent of a fast ion conductor phase transition. The quality of the data is not sufficient to isolate the most representative fit. Probably the simplest definitive measurement would be of the thermal response of the material over the transition range 200 - 400°C. The sensitivity required could probably be obtained using DSC. Once again the equipment was unavailable due to prior commitments. In any event, further electrical investigations are required to understand the ambiguity highlighted above.

3.2.4 Transport Number Measurements

Following the method described by Tubandt [188], it was hoped to measure the ease of movement of the sodium ion, and to attempt to determine if it is the sole conducting species in these materials. The technique is based upon the measurement, by weight change, chemical or energy dispersive analysis, of the number of ions transferred across a block of material under the application of a drive voltage for a given time. The "block" is constructed from a series of (thin) tablets of roughly equal weight, which may act as non-blocking electrodes, for example, in a more complex, multi-segmented experiment.

The principal requirement is to supply ions to the discs under test. Since measurements are oriented towards controlled electrical conditions (i.e. constant applied voltage), power sources are employed which supply electronic charge. This thus necessitates the introduction of an intermediate material having a high conversion rate from input electrons to ions capable of entering the specimen "stack" under investigation. In the event of an inadequate source of appropriate ions being placed at an interface, electrode polarisation effects will occur, leading to a measured current decay under application of a steady d.c. potential.

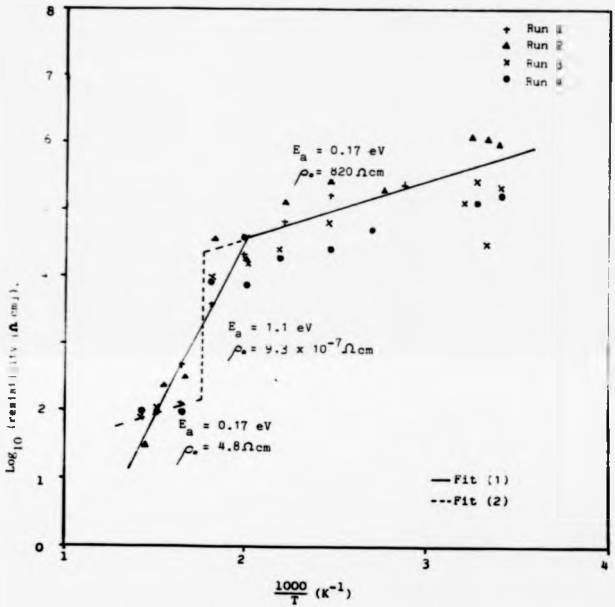

Figure 3.33. Arrhenius plot for a $80Na_2B_4O_7.20NaCl$ glass-ceramic specimen.

The majority of experiments [189] have employed solid metallic electrodes, in the form of foil or fired paint, which are readily converted into ions by a simple electrochemical reaction. The materials in most common usage are platinum and silver, although some workers have utilised more elaborate ion sources, notably a sodium-mercury amalgam [189]. However the "standard" technique for "changing" the conducting species between the components of a "stack" appears to be by the introduction of an *intermediate* block of a pressed alkali halide [188,189]. A high proportion of bulk conduction is ensured in these materials since pressing causes the small crystals added to the die to meld together by virtue of their cold flow properties, thereby leading to more efficient charge carrier conversion.

At interfaces between compounds having different cationic species as their majority carriers, the net flow of charge between the electrodes exports the "previous" majority ion into the following block, which upon reduction to create the "new" mobile carrier, leaves a metallic deposit in the form of thin filaments, which bonds the two blocks and leads to the possibility of creating a short circuit. For this reason, so-called "protective electrolytes", which form no such threads under electrolysis, are introduced [188] to a "stack" to prevent the possibility of shorting. In the case of anionic conductors, the ions may combine to evolve gaseous material (e.g. in chlorine or oxygen ion conductors) which is not so damaging to the results of a long-term experiment, although the net stoichiometry of the system is affected.

In the author's opinion, a further complication exists when systems undergoing changes in the ionically conducting species are considered: the ability of the host structure to conduct a "foreign" ion is being measured, and not the conductivity of the "normal" host species.

The ramifications of this problem are that the "foreign" ion may not follow the same conduction pathways as the "normal" ion. In the light of experience gained in the current work, where silver paste electrodes appear to have been depleted during the course of "d.c." conductivity measurements on glass-ceramic specimens, presumably forming a thin coating upon individual grain boundaries (i.e. producing a grey coloration throughout the specimen, the chemical cause of which is not measurable using EDAX methods - see section 3.2.2), it was

decided to reject conventionally accepted arrangements. Instead, the electronic current was to be applied directly to a good solid state source of sodium ions (sodium β" alumina), which would then provide sodium ions to the material under test. Obviously from the problems outlined earlier in this section, electrode polarisation effects will occur since β" alumina has been shown to exhibit negligible electronic conductivity [186], and hence the build up of ion depleted regions will manifest, thus reducing the current passed considerably. It is argued here that ion conduction effects, although greatly reduced, will be measurable if the experiment is conducted over a much longer time. The electrode polarisation should rapidly attain an equilibrium condition where a small number of the electrons supplied will neutralise some of the polarisation and thus provide a nominal leakage current. By monitoring the current flow through the 'stack' and using Faraday's law, the concentration difference between the two outermost blocks should, in principle, be able to be equated to the number of (positive and negative) ions taking part in the conduction process. This in turn may prove the existence of oxygen ion conduction in these materials, inferred by analogy from the postulate presented by Owen [171] for calcium aluminoborate glasses. Hagel and MacKenzie [172] did not agree with this conduction mechanism from ^{17}O diffusion measurements, but did not present a specific alternative.

The fundamental assumption with this proposed arrangement of a stack of the material under test sandwiched between β" alumina blocks is that the rate of sodium ion transfer through the β" alumina is far higher than that through the test material. This should provide a check of the measured bulk "d.c." conductivity of the specimen under test.

One further modification to the accepted experiment was also made, to examine the possibility of surface conduction along the sides of the material. The radial surface of the central disc was earthed as indicated in Figure 3.34, which should have the effects of neutralising any changes in the immediate vicinity thus resulting in an increase of the mass of the central disc. Similar calculations to those involved to determine the bulk transport can be performed to obtain the d.c. surface conductivity of the specimen, and a correction subsequently made if necessary for neutralisation of ions within the bulk, taking guidance from electric field

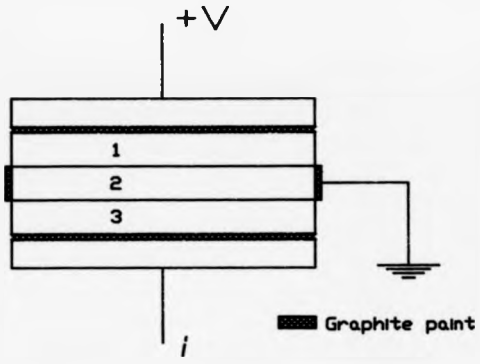

Figure 3.34.
Arrangement of disc specimens in Tubandt apparatus. At sufficiently high temperatures, positive ions will migrate from disc 1 to disc 3, which is recorded as a change in mass. The measured current *I* can be processed to obtain the transport number by Faraday's law.

calculations based on the measured bulk conductance. The introduction of this additional electrode was felt necessary due to the previous observation of high surface conductance in the glass-ceramic specimens under investigation in the current work [9].

In order to categorise the operational efficiency of this alternative experimental arrangement, an introductory experiment using a stack comprising 3 blocks of sodium β'' alumina was performed under conditions equivalent to those envisaged in operation with the haloborate glass and glass-ceramic specimens to be tested.

So far, only one sample, sodium β-alumina, has been investigated. The β-alumina was made from sodium aluminate and α-alumina following the method described by Hind [190]. The criterion described by Fletcher et al. [191] (namely crushing, performing X-ray diffraction, re-compacting and sintering until the diffraction patterns for two successive sinters were seen to be the same) was employed to determine the end of reaction.

At the onset of the experiment, the discs are weighed. These flat, parallel, highly polished (6 μm diamond paste) specimens were then clamped tightly together following the application of graphite drive, guard and working electrodes, and placed in an inert atmosphere (nominal purity nitrogen, containing typically 25 ppm water) at 350°C (T_g - 100°C) for a long (~ weeks) time under an applied voltage of 15 V. The results obtained using windowless EDAX analysis in the SEM are shown below.

Specimen Position	Element	Ratio of Peak Height to Aluminium (%)
driven surface (+15 V applied)	Na	1.87
	O	22.67
working surface current measured: virtual earth)	Na	5.28
	O	22.69

The crude measurement technique of measuring peak heights only was adopted since quantitative windowless analysis is as yet unavailable.

The results show a measurable difference in the sodium ion concentration. The consistency of the "immobile" oxygen ion concentration shows good reproducibility, although a further check of the technique, namely calculation of the transport number, has yet to be performed. This was not possible since the record of current passed during the experiment was destroyed.

3.3 STRUCTURE

3.3.1 X-Ray Diffraction (XRD)

This was the principal "direct" structural tool used in the current work. It was hoped to infer the structure of these materials by "fingerprinting" with spectra of well-categorised compounds. Any differences in local microscopic arrangement would be anticipated to be shown from the indirect techniques described in the next section.

Spectra were obtained using a Philips PW1380 goniometer and copper K_α radiation under ambient conditions. The optimum resolution of this instrument was 0.01° 2θ. The zero angle position was checked and reset perodically during this work and found to vary by as much as 0.5° 2θ.

For ease of data acquisition and presentation, a Commodore PET microcomputer was included in this arrangement, but was later removed following an uncorrected hardware fault. Work was carried out to replace this facility using a Perkin-Elmer 9600 data station, which was intended to form the basis of primary storage and analysis of higher resolution data to be obtained from an equipment upgrade. The principal enhancement was to be from the introduction of a single crystal monochromator and analyser to the current set up. Unfortunately this modification has not been carried out yet due to lack of funding. A research proposal to the SERC is to be submitted to examine crystal structures by a combination of MAS NMR, high-resolution XRD and neutron scattering, using data from neutron scattering experiments to be performed on a selection of doped borax-based glass-ceramics by Dr. W.I.F. David at the Rutherford-Appleton Laboratory. The incentive for this work is based upon the large spectral

discrepancies obtained using the current XRD apparatus shown in Figures 3.35 - 3.38. The additional peaks extra to the JCPDS standard [191] cannot be identified with any phase within the JCPDS powder diffraction files. Moreover, the data presented here is not of sufficient quality to perform a structure refinement [52]. An anomaly is also inherent in this system since a high resolution X-ray diffraction study performed at Harwell by Dr. R. Bellamy did not exhibit similar features, as shown in Figure 3.39. The discrepancies within the diffraction patterns can best be expressed as a reversal in trends. By comparing Figures 3.35 and 3.39, the anhydrous borax (AB) material shows intensity variations between the two measurements. This can be seen more clearly by reference to Figure 3.40, which displays the two spectra on similar scales. The differences in peak positions are within the acceptable limits outlined by the JCPDS for "fingerprint" structure determinations. The intensities, however, do exhibit changes greater than the proposed 5% "window". This is best illustrated by reference to Figure 3.40 at 2θ values of ~ 13.6, 33.5 and 36.5 degrees. It is for the sodium chloride doped material that the "reversal in trends" indicated above occurs. In the "Warwick data", additional peaks are obtained, whilst the number of peaks obtained from the "Harwell data" is reduced compared to the "standard" $Na_2B_4O_7$ spectra. A comparison between the two diffraction patterns is made in Figure 3.41. Some of the absences in the Harwell data can be derived from the differences observed when compared against its "parent" phase in Figure 3.39, but the other extra peaks between the two 10% NaCl doped phases cannot be simply parameterised. It is doubtful that the cause of this discrepancy lies in sample preparation, since both samples were obtained from the same block of the parent glass, the only difference being that the samples sent to Harwell were dried in a furnace at 200 °C after crushing prior to sealing in glass ampoules for ease of packaging.

High isotropic ^{11}B purity is required to perform neutron diffraction experiments due to the high collision cross-section of ^{10}B (~ 10^4 times that of the other constituent elements [69]). Although only 20% abundant in nature, the elimination of ^{10}B from th bulk material is presumed difficult by the lack of supplies of high-purity materials (95-97% ^{11}B appears to be the highest purity that is commercially available).

Figure 1.35. X-ray diffraction data for NaCl-doped specimens.

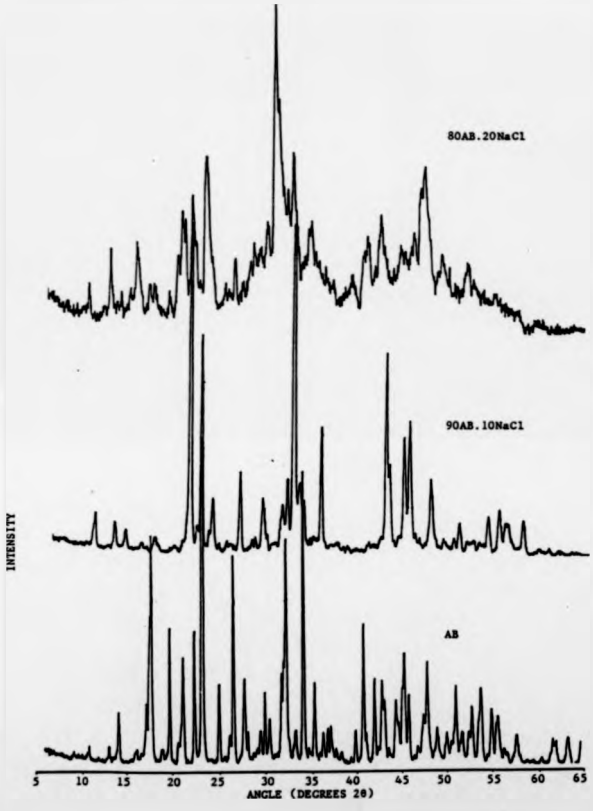

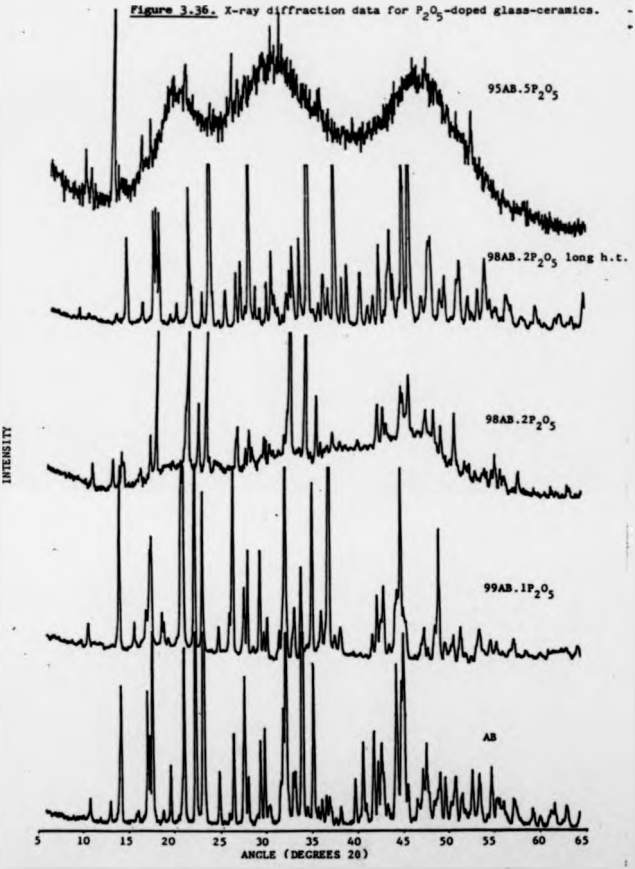

Figure 3.36. X-ray diffraction data for P_2O_5-doped glass-ceramics.

Figure 3.27. X-ray diffraction data for TiO_2-doped glass-ceramics.

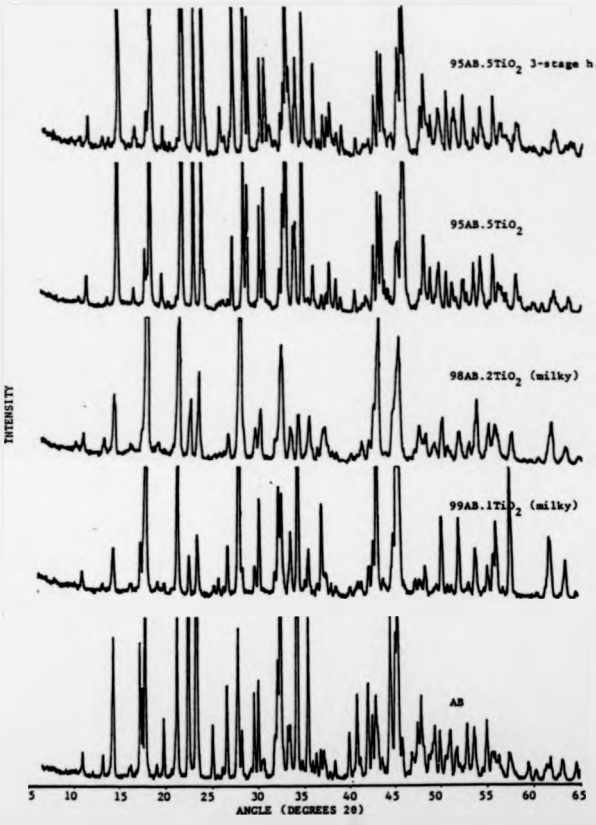

Figure 3.38. X-ray diffraction data for TiO_2-doped glass-ceramic specimens formed in a 3-stage heat-treatment.

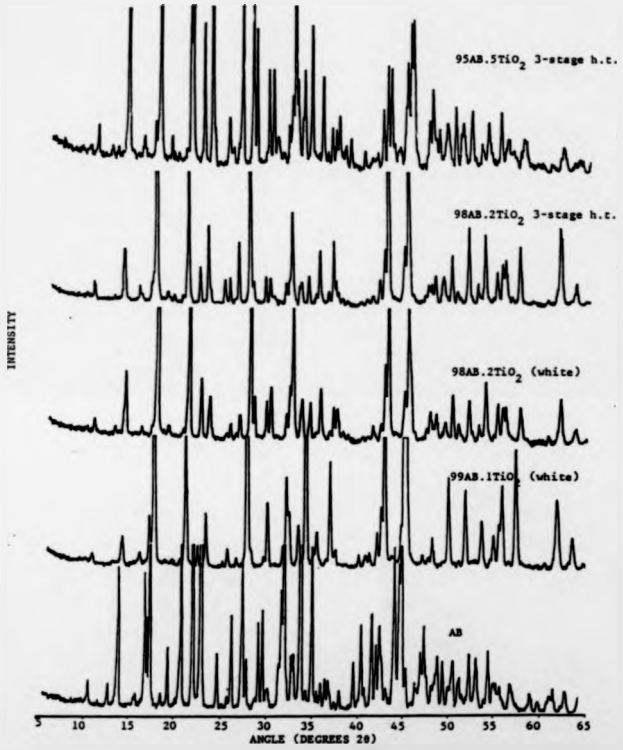

Figure 3.39. X-ray diffraction data obtained at Harwell.

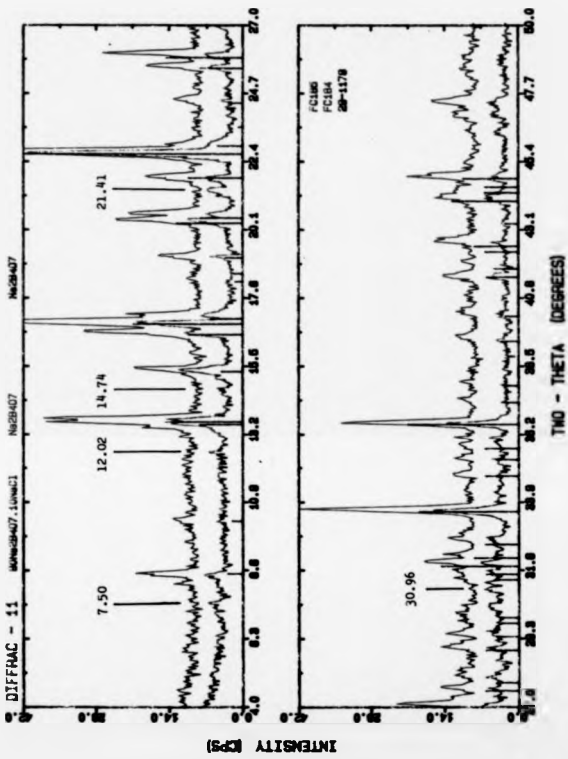

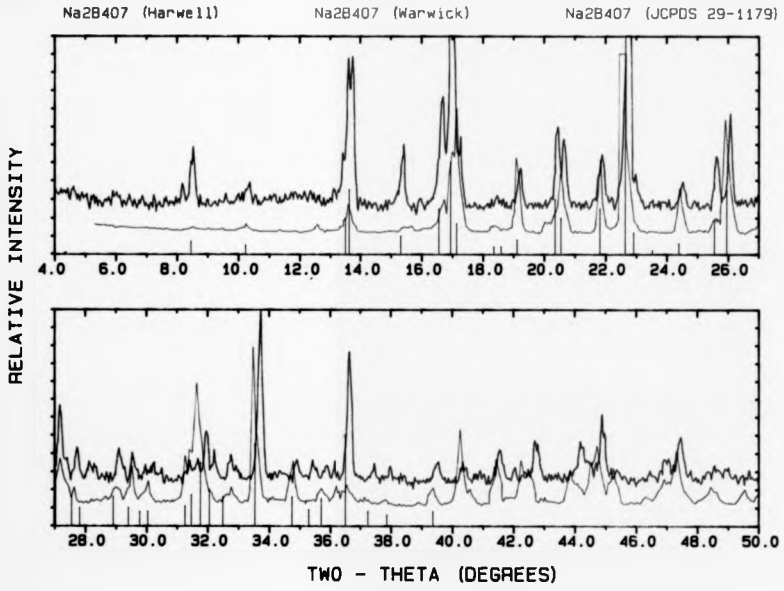

Figure 3.4a. Comparison of X-ray diffraction spectra for a devitrified $Na_2B_4O_7$ specimen.

Figure 3.41. Comparison of X-ray diffraction spectra for a devitrified $90Na_2B_4O_7.10NaCl$ specimen.

3.3.2 Spectroscopic Investigations

3.3.2.1 Infra-red Studies

The infra-red spectra presented here were obtained using a Perkin-Elmer PE983 double beam spectrophotometer interfaced to a 9600 data station, having a working frequency range of 5000 - 180 cm^{-1}. However, the spectral absorption in the range 5000 - 4000 cm^{-1} is featureless for the majority of glass systems, and so the upper frequency limit was taken as 4000 cm^{-1}. Similarly, the low frequency limit was increased to 200 cm^{-1} by the onset of significant absorptions within both the KBr used as a suspension medium for some of the measurements and the instrument itself, as shown by experiments using alkali halides with lower frequency absorptions. Spectra were collected from a variety of preparation techniques. Transmittance measurements were performed upon blown films (glasses only), and pressed pellets using dry KBr as the dispersion medium. Some controversy has previously surrounded the use of alkali halides for this purpose due to the possibility of ion exchange [33], but work by Krogh-Moe [70] has shown this objection to have no experimental validity in borate glasses. An alternative technique was to examine the crushed powder in a Nujol (spectroscopic grade liquid paraffin) mull between silver iodide plates, but this was found to be unsatisfactory and not pursued further in this work. Reflectance measurements were also carried out, using a Beckmann-RIIC TR9 prism fabricated from a KRS-5 crystal. A schematic of this latter arrangement is shown in Figure 3.42.

A facility present in the applications software for the 9600 data station allowed a "difference" spectrum to be created interactively. This means that spectra could be "massaged" to remove the absorption bands of the materials used in the data acquisition process (e.g. water and KBr from the pressed pellet, AgI from the liquid cell geometry, or the KRS-5 crystal from reflection spectra) by first scanning the "blank". The underlying assumption is of no physical or chemical interaction between the two media (i.e. linear superposition of the respective spectra). The use of this software was felt to be necessary and valid only in the case of the reflectance spectra.

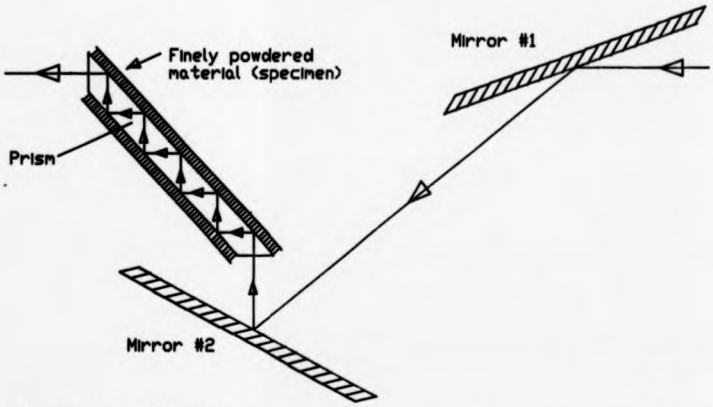

Figure 3.42.
Ray diagram of Multiple Attenuated Total Reflection (MATR) arrangement.

Typical results from these techniques are shown in Figure 3.43 for comparison. Spectra obtained from a glass-ceramic and its parent glass show the same essential features but for the sharpening of the absorption bands in the crystalline compound via a more ordered local environment, as shown in Figure 3.42.

The primary purpose of the spectroscopic measurements was to look for any localised structural variations in the glassy and crystalline phases that may be associated with the various dopants employed in this work. The glasses exhibited no obvious changes with dopant addition. The sharpening of the absorption bands caused by the increased ordering characteristic of the crystalline process highlights a series of subtle changes in the spectra reproduced in Figure 3.44, which is shown in more detail by the difference spectrum (which should only be used as a guide) in Figure 3.45. However interpretation of the spectra to identify the fundamental structural groupings is hampered by the limited database of known molecular vibrations. The most recent work is by Konijnendijk [72], who discussed the initial infra-red and Raman work in terms of 3- and 4-coordinated boron atoms, and concluded that the absorption bands can only be interpreted using the larger structural groups shown in Figure 2.10. However, by ascribing the absorption bands in the frequency range 900 - 1100 cm^{-1} to BO_4 groups and the absorption bands in the range 1250 - 1350 cm^{-1} to BO_3 groups, Minami et al. [33] successfully related the relative intensities to composition, which formed the basis of their postulate of B-X and B-O-X bonding in the AgX-$A_{g2}O$-B_2O_3 ternary system.

A summary of the characteristics vibrations together with the positions of the absorption bands is reproduced in Table 3.3. Therefore much of the information contained in the spectra shown in Figure 3.44 cannot be usefully processed.

However, by examination of the bands at ~ 950 cm^{-1} and 1300 - 1400 cm^{-1}, several observations can be made. For increasing NaCl concentrations, the absorption band at ~ 1400 cm^{-1} shows an increase which may be interpreted by extending the validity of the boroxol ring "fingerprint" to rings containing 3-coordinated boron atoms i.e. ring-type metaborate groups. This would appear consistent with the decrease in the amplitudes of the B-O bond stretching absorption at ~ 1260 cm^{-1} and the "breathing" motion of 6-membered rings containing four-fold

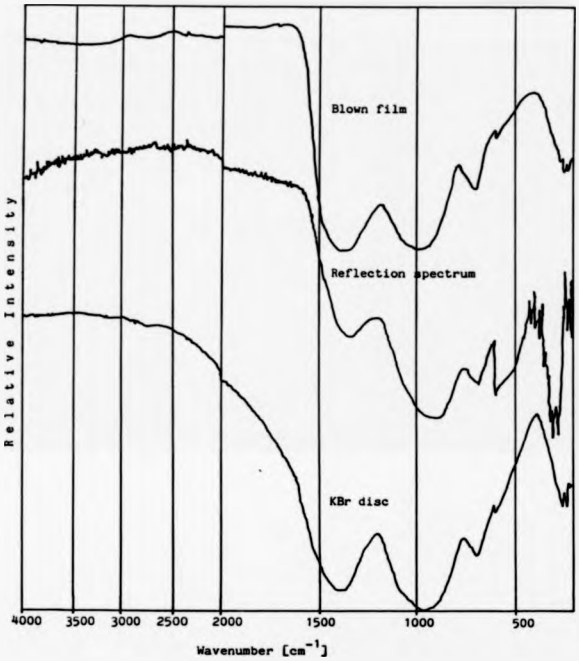

Figure 3.43. Comparison of infra-red spectra obtained by different methods.

Figure 3.44. Infra-red transmittance spectra obtained from a series of devitrified glasses of general formula $(1-x)Na_2B_4O_7.xNaCl$ using the KBr briquet technique.

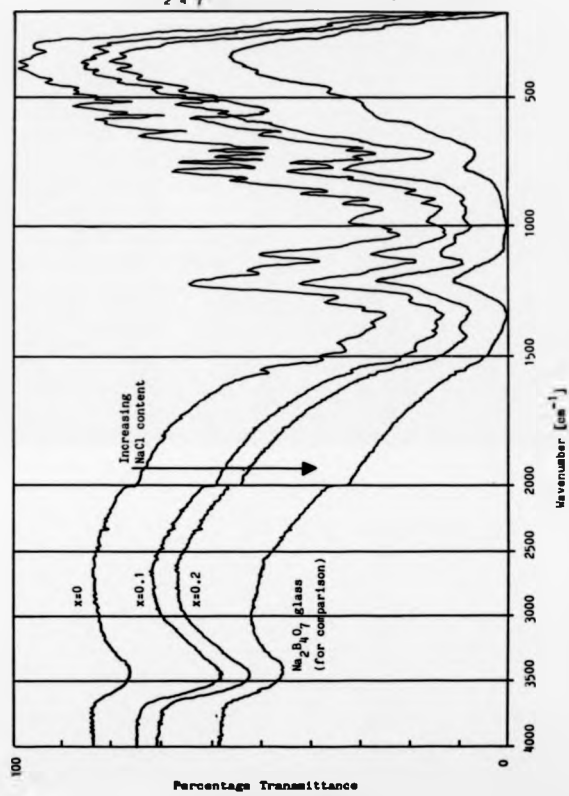

Figure 3.45. Example difference spectrum from two devitrified halobarate glasses.

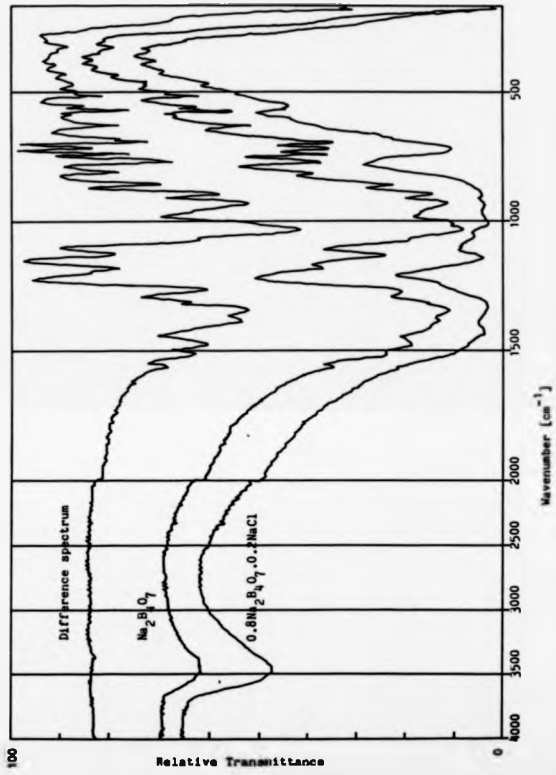

Table 3.3 Standard Infra-Red Absorption Bands.

Wavenumber (cm^{-1})	Group Motion.
720	B-O-B bending in B_2O_3 [72]
780	6-membered ring stretch [82]
950	4-coordinated boron-oxygen stretch [72]
1400	boroxol ring stretch in B_2O_3 [72]
960, 1200 1380, 1910	BCl_3 [193]
710, 1640 2120, 3400	H_2O [194]

coordinated boron atoms (e.g. the triborate group) at ~ 980 cm^{-1}. This would imply the production of more non-bridging oxygens, and could be interpreted as the formation of boron-chlorine bonds. An alternative interpretation could be the production of non-briding B-O bonds via an increased oxygen concentration, absorbed into the melt as a consequence of chlorine loss during fusion. The chloride loss is readily verified by reference to section 3.1.1.

In the event of the formation of a boron-chlorine bond, the appearance of a new absorption band may be expected, possibly occurring in a similar position to the bands observed in BCl_3 vapour [193]. One possibility could exist for this hypothesis since the peak at ~ 1200 cm^{-1} exhibits a slight increase for higher NaCl concentrations. However there are no similar changes at the frequencies corresponding to the other standard peaks. This argument cannot be contradicted since no structural assignments to the absorption bands have been made.

The amplitudes of other absorption bands can also be seen to change with increased dopant concentration (for example, the most notable variation is in the decrease of the 1120 cm^{-1} band) but unfortunately cannot be linked to any structural groups. The presence of the primary water band in the spectra at ~ 3420 cm^{-1} [194] was attributed to incomplete drying of the KBr by scanning the blank.

Therefore, the conclusions that can be drawn from infra-red investigations are quite tentative, although systematic structural variations are in evidence for NaCl-doped materials. Similar examinations of the P_2O_5, TiO_2 and Pt doped specimens did not appear to show such visible changes.

3.3.2.2 Raman Spectroscopy

Since the necessary apparatus was not present at Warwick, the facility at the Chemistry department, under the general guidance of Dr. D.N. Waters, Bristol University, was made available by Borax Research Ltd.

The primary excitation was provided by the blue 488.0 nm line from a CW argon/krypton ion laser with a beam intensity of ~ 550 mW. The raw data was obtained using a

SPEX Ramalab spectrometer in an unpolarised form, and therefore the following data analysis is partially limited by this. The spectrometer itself was calibrated using the strong 314 cm^{-1} Stokes line of CCl_4 as a standard. A modified solid sample holder allowed finely powdered materials to be examined. Results are shown in Figures 3.46 and 3.47.

In the ensuing analysis, a "fingerprinting" technique similar to that carried out for the infra-red spectroscopy was attempted. The characteristic vibrations reviewed by Konijnendijk are reproduced in Table 3.4. The first observation that can be made by comparison of Figures 3.46 and 3.47 is that there are fewer, more widely separated peaks than for the complex infra-red spectra presented in the previous section. Furthermore the large decrease in the peak widths previously obtained for the infra-red upon comparison of the glasses and glass-ceramics respectively has been greatly reduced. The combination of these two observations permits an easier and more justifiable comparison between the glassy and crystalline phases of each material.

Similar conclusions are drawn to those obtained from infra-red spectroscopy. By reference to Table 3.4, it can be seen that the peak at 647 cm^{-1} characteristic of the ring-type metaborate group increases with increasing NaCl concentration, implying the formation of non-bridging oxygens within the structure, but little change in the 6-membered breathing mode at ~ 760 cm^{-1} accompanies this, unlike the observations from the infra-red. The indication of a boron-chlorine bond is again evident, by the existence of a shoulder on the steep background at ~ 475 cm^{-1}. However the detail is masked by the fluorescence from the laser in the frequency range ~ 400 cm^{-1} - 650 cm^{-1}, and so no definite inference can be made. The fluorescence arising from the devitrified 15% NaCl doped sample cannot be explained, since the presence of atmospheric moisture was not found to change the behaviour of this or any other sample investigated. Once again no discernible difference was obtained in the spectra of the "classically" nucleated samples.

Figure 3.46. Raman spectra of NaCl-doped glasses.

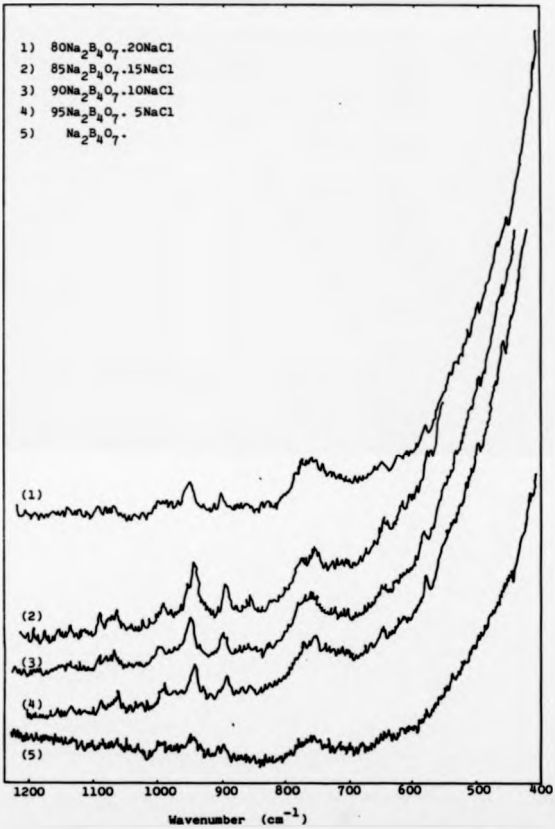

Figure 3.47. Raman spectra of NaCl-doped glass-ceramics.

Table 3.4 Summary of Standard Raman Peaks.

Wavenumber (cm^{-1})	Group Motion.
473,469 466,257	BCl_3 [195]
610 - 630	Ring-type metaborate group "breathing" [82]
700	General 6-membered ring "breathing" [72]
806	Boroxol ring deformation [72]
820 - 850) 920 - 930)	BO_3^{3-} symmetric
)	B-O bond stretching [72]
1250	Possible pyroborate group [72] characteristic motion
1500	Symmetric non-bridging oxygen stretching of ring-type metaborate group [72]

3.3.3 Thermal Expansion Coefficient

The measurement apparatus comprised a water-cooled vertical vitreous silica dilatometer, the working part of which was heated at a rate of 1.73°C min^{-1} in a muffle furnace. The displacement of the push rod in contact with the specimen was measured using the voltage output from an inductive LVDT (Linear Variable Differential Transducer). Conversion of this measurement into length was made via periodic calibration of the arrangement using a platinum standard. Results for a series of glasses and glass-ceramics are presented in Table 3.5. Due to the high expansion coefficients measured, the "silica correction" has not been made. Moreover the expansivity data is presented in polynomial form following the extensive work summarised by Krishnan et al. [88].

3.3.4 Thermal Properties

The thermal evaluations performed in the current study were principally oriented towards an operational knowledge of the glass forming process, and so no thermal property measurements and investigations of the annealing and crystallisation behaviour were undertaken. In light of these semiquantitative requirements, only D.T.A. was performed. The apparatus was a home built arrangement with thermally recrystallised alumina as the principal constructional material, and a helical crusilite rod as the furnace element. The essential features of the apparatus are reproduced in Figure 3.4B.

Due to the low e.m.f.s produced for a unit temperature change for the Pt/Pt-Rh differential thermocouple used, the elimination of noise became a significant problem at a vital stage in the work. This was reduced by the application and subsequent firing in situ of an organoplatinum paint to the surface of the alumina specimen holder to form an earthed screen for the output signal. The thermocouple junctions were also coated with a thin layer of Saucreisen electrotemp cement no. 8 to electrically isolate them from the crucibles and attempt to reduce r.f. pickup from the furnace. This necessitated the introduction of the Pt-Rh dishes shown in Figure 3.4B, to reduce abrasion of this coating during specimen loading.

Table 3.5 Summary of Thermal Expansion Data

Following the format presented by Krishnan et al. [86], the data is presented in the form of the premultiplier factors A, B and C, where thermal expansion coefficient α at temperature T (in ^{o}C) is given by

$$\alpha = A + BT + CT^2$$

Specimen	$A(x10^{-7})$	$B(x10^{-7})$	$C(x10^{-7})$	$T_g(^{o}C)$
AB glass	315	-2.9	$1x10^{-2}$	447
AB cryst.	39.2	0	0	520
90AB.10NaCl glass	85.3	0.30	$-3.9x10^{-4}$	414
90AB.10NaCl cryst.	85.3	0.66	$-1.3x10^{-3}$	437
80AB.20NaCl glass	160	0	0	410
80AB.20NaCl cryst.	139	0	0	535
99AB.$1P_2O_5$ glass	377	-3.0	$1x10^{-2}$	420
99AB.$1P_2O_5$ cryst.	98	-0.3	$1.2x10^{-3}$	565
98AB.$2P_2O_5$ glass	117	$-2x10^{-2}$	0	445
98AB.$2P_2O_5$ long h.t.	206	-1.7	$6.8x10^{-3}$	575
95AB.$5P_2O_5$ glass	185	-1.11	$3.8x10^{-3}$	450
95AB.$5P_2O_5$ h.t.	170	-0.74	$2.8x10^{-3}$	440
99AB.$1TiO_2$ glass	196	-1.02	$3.6x10^{-3}$	440
99AB.$1TiO_2$ cryst.	245	-1.89	$6.6x10^{-3}$	530
98AB.$2TiO_2$ glass	283	-2.44	$8x10^{-3}$	450
98AB.$2TiO_2$ cryst.	242	-1.95	$7x10^{-3}$	615
98AB.$2TiO_2$ 3-st.h.t.	313	-2.45	$8.6x10^{-3}$	430
95AB.$5TiO_2$ glass	164	-0.95	$3x10^{-3}$	440
95AB.$5TiO_2$ cryst.	275	-2.16	$7.6x10^{-3}$	450
AB + 10^{-4}%Pt glass	193	-1.31	$5x10^{-3}$	450
AB + 10^{-4}%Pt cryst.	412	-5.39	$2x10^{-3}$	430
AB + 10^{-3}%Pt glass	155	-0.65	$2.6x10^{-3}$	455
AB + 10^{-3}%Pt cryst.	146	-1.23	$4.3x10^{-3}$	480
AB + 10^{-2}%Pt glass	185	-1.09	$4.2x10^{-3}$	450
AB + 10^{-2}%Pt cryst.	43	0.94	$-2.8x10^{-3}$	425

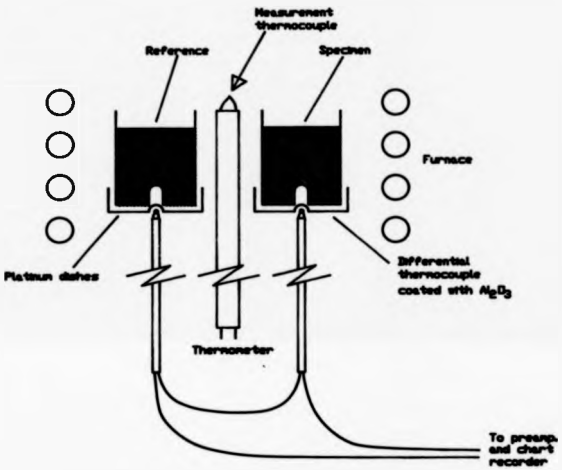

Figure 3.48.
Schematic D.T.A. arrangement.

Furthermore, since small temperature changes were being measured, the temperature uniformity of the measurement cell over the working temperature range (room temperature to 1200° C) was an important consideration, since "dummy runs" having alumina powder (the standard reference material in these experiments) in both crucibles produced drift in the signal which increased with increasing temperature, and depended on the rotational orientation of the cell with respect to the furnace. Attempts to "smooth out" these differences using an oxidation resistant stainless steel hood to equalise the temperature, and a biased differential thermocouple output were unsuccessful.

A typical D.T.A. trace for a borax-based glass is shown in Figure 3.49. The flat baseline is due to the compensation of the signal drift by the thermal diffusivity differences of the specimen with respect to the alumina standard. Values for a limited selection of materials are presented in Table 3.6.

3.3.5 Density

The densities of the materials examined were determined using picnometry with Nujol as the immersion medium using the equation

$$\rho_s = \rho_f \left(\frac{m_{air}}{m_{air} - m_f}\right) \qquad (3.6)$$

where ρ_s = specimen density

ρ_f = fluid density (880 kgm^{-3} at 20°C)

m_{air} = in air

m_f = mass of specimen in fluid.

The results are summarised in Table 3.7.

Figure 3.49. D.T.A. trace for a $90(Li_2O.2B_2O_3).10LiCl$ glass, typical of all results obtained in this work.

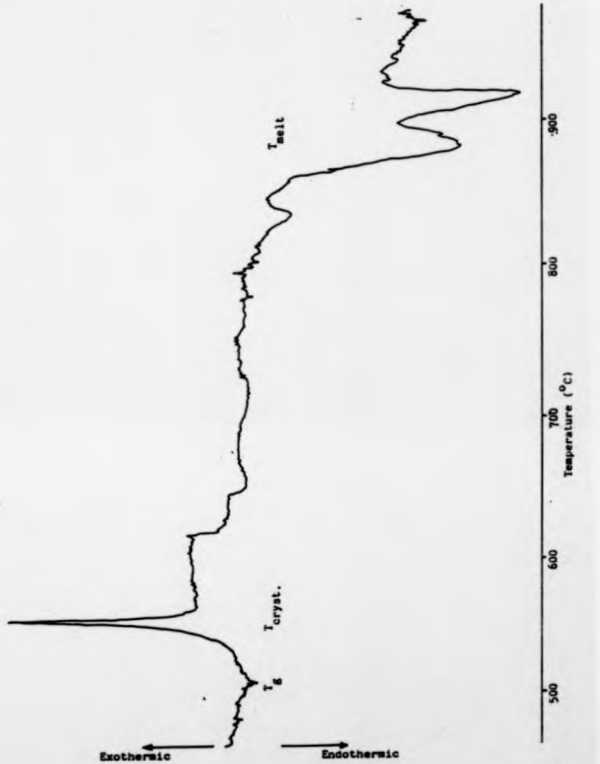

Table 3.6 D.T.A. Summary

Glass	T_g (°C)	T_{cryst} (°C)	T_{melt} (°C)
$Na_2B_4O_7$	435	545	900
$90Na_2B_4O_7.10NaCl$	470	530	920
$70Na_2B_4O_7.30NaCl$	470	690,715	820
$Li_2O.3B_2O_3$	510	830	1000
$90Li_2B_4O_7.10LiCl$	520	830,880,910	1000
$K_2B_4O_7$	430	790	950
$90CaB_4O_7.10CaCl_2$	430	710,740,765	920

Table 3.7 Mechanical Properties of Some Materials Based on Anhydrous Borax (AB)

Table 3.7a Borax-based glasses

Specimen	K_{1_c} ($\times 10^5$ $Pam^{\frac{1}{2}}$)	Young's Modulus (GPa)	Hardness (GPa)	Density (kgm^{-3})
AB	2.93±0.07	3.68±0.09	3.69±0.26	2367
90AB.10NaCl	2.92±0.09	4.32±0.70	3.98±0.19	2384
80AB.20NaCl	2.70±0.02	2.44±0.17	3.95±0.31	2386
AB	4.38±0.12	5.55±0.27	4.18±0.61	2367
$99AB.1P_2O_5$	4.25±0.13	5.75±0.36	4.79±0.26	2375
$98AB.2P_2O_5$	4.49±0.12	5.98±0.07	3.41±0.46	2363
$95AB.5P_2O_5$	4.28±0.09	6.31±0.23	4.42±0.48	2367
$99AB.1TiO_2$	4.89±0.12	5.89±0.28	2.00±0.07	2362
$98AB.2TiO_2$	4.78±0.09	5.40±0.32	3.85±0.19	2364
$95AB.5TiO_2$	4.26±0.16	6.03±0.51	3.49±0.40	2362
AB + 10^{-4} %Pt	3.13±0.15	1.52±0.07	3.23±0.19	2356
AB + 10^{-3} %Pt	3.14±0.15	1.36±0.04	2.94±0.28	2361
AB + 10^{-2} %Pt	2.97±0.17	1.91±0.08	3.30±0.34	2357
95AB.5NaCl	3.15±0.05			
85AB.15NaCl	2.88±0.06			

Table 3.7b Devitrified borax-based glasses

Specimen	K_{1c} ($\times 10^5$ Pam$^{\frac{1}{2}}$)	Young's Modulus (GPa)	Hardness (GPa)	Density (kgm^{-3})
AB	0.65±0.09	2.04±0.37	1.49±0.31	2444
90AB.10NaCl	1.68±0.12	3.18±0.59	2.00±0.14	2428
80AB.20NaCl	4.17±0.37	4.32±0.50	1.41±0.05	2395
AB	0.75±0.13	1.92±0.13	2.74±0.15	2444
99AB.1P_2O_5	0.62±0.08	2.11±0.28	2.67±0.40	2640
98AB.2P_2O_5	3.75±0.17		1.86±0.20	2385
98AB.2P_2O_5 (long h.t.)	0.51±0.13	3.13±1.07	1.52±0.24	2494
95AB.5P_2O_5	4.06±0.10	2.42±0.61	3.19±0.32	2363
99AB.1TiO_2 milky	-	0.53	2.87±0.17	2440
white	1.03±0.19	1.78±0.07	2.47±0.23	
98AB.2TiO_2 milky	-	0.95	2.51±0.41	2422
white	*	1.81±0.12	2.10±0.15	
98AB.2TiO_2 3-stage h.t.	1.74	4.62±0.55	1.58±0.12	2448
95AB.5TiO_2	0.69	1.88	1.62±0.00	2418
95AB.5TiO_2 3-stage h.t.	0.99	1.72±0.39	3.11±0.17	2437
AB + 10^{-4}%Pt	-	1.22	2.00±0.21	2493
AB + 10^{-3}%Pt	-	-	-	2433
AB + 10^{-2}%Pt	-	3.81	2.21±0.36	2416
95AB.5NaCl	1.07±0.36			
85AB.15NaCl	3.87±0.56			

* Fractured on loading: top loader force = 2.1 N.

3.4 MECHANICAL PROPERTIES

3.4.1 Young's Modulus

Rectangular bar specimens machined in the manner described in section 3.1 were subjected to 4-point loading using an Instron 1122 strength testing machine with a miniature loading jig [196] having spans of 10 mm for the outer and 2 mm for the inner. The 1122 is a displacement oriented machine which moves the crosshead in a given direction to supply the load, which is then measured with a load cell of variable sensitivity and subsequently displayed as the abscissa on a Y-t chart recorder. From a knowledge of the crosshead and chart speeds, the displacement may then be readily calculated. To obtain maximum sensitivity, the lowest standard crosshead speed (0.05 mm min^{-1}) was employed at all times. The data from the load-displacement graph was then processed in the linear region via a simple computer program to give values for Young's Modulus E using equation 2.19. These results are presented in Table 3.7.

3.4.2 Hardness

Vickers hardness values were obtained for a series of glasses and glass-ceramics in the manner described in section 2.2.3.3.1. A load of 1.96 N applied for 10 s, was used to make the indents. The hardness value was obtained from the diagonal length a of the observed impression formed using load P via the equation

$$H = \frac{0.4635P}{a^2}. \qquad (3.7)$$

where the premultiplier constant was obtained for the total contact area between specimen and indenter (apex angle = 148.1°). The results obtained are summarised in Table 3.7.

3.4.3 Fracture Toughness, K_{1c}

Test bars prepared in the manner described in section 3.1 were notched using the saw described in section 3.1.3. "Neatcut" oil [179] was used as both lubricant and inert medium for the ensuing fracture. Due to the brittle and fragile nature of these specimens, the existing vice used to support the bars during notching was unsatisfactory, frequently crushing or spalling the

surface during clamping. Therefore a new vice, using compressed cork-lined jaws was constructed. A drawing is shown in Figure 3.50. The specimens were then left in air for a standard 2 hours in order to standardise on the relief of any residual stresses introduced during this final machining prior to controlled fracture using a 4-point bend using the 1122 strength testing machine described above, again with a crosshead speed of 0.05 mm min^{-1}. Due to the lack of an existing jig satisfying the dimensional requirements necessary for a valid K_{1c} measurement (section 2.2.3.1.2) a 4-point bend apparatus similar in design to existing versions but of correct dimension was constructed. The plan is reproduced in Figure 3.51. Observation of the load-displacement curves for each specimen highlighted two problems: firstly, the load-displacement curve was continuous at low loads. Ideally this should be discontinuous at the onset of loading. This was attributed to the elastic properties of the support materials in the Instron since the effect was present for a variety of specimens, bend apparatus and test geometries [197], but may still lead to spurious results. Secondly, and perhaps more importantly, the glass-ceramic specimens showed a significant deviation from linearity towards the critical load, as shown in Figure 3.52, together with the traces of the parent glasses for comparison. Fortunately, by examination of the criteria presented by Knott and Elliott [135] for a valid K_{1c} the effective toughness K_{1Q} (obtained from the maximum sustained load) could be equated to the critical toughness value. The processed data is shown in Table 3.7.

A limited study using the now popular indentation method of crack initiation [148,149,167,198] was also made on glassy borax. The indent was produced using a load of 4N for a period of 10 s (± 0.2 s) in a silicon oil environment at a loading/unloading rate of 0.5 mm min^{-1} (found to be the optimum by trial) on bars having a 0.25 μm surface finish, the other 3 sides being polished to a 14 μm finish with diamond paste. The edges of the bar were bevelled slightly to a 14 μm finish to eliminate spurious results. After standing in a desiccator for 5 hours, the bars were broken in 4-point flexure using the standard loading rate. Results are presented in Table 3.8 for comparison. The SENB (single edge notched beam) value is seen to be higher than those obtained for the indentation technique, in keeping with other work, but the observed lower spread of values for the SENB seems to be anomalous (Figure 2.21). The indentation method of toughness measurement was not pursued further in this work.

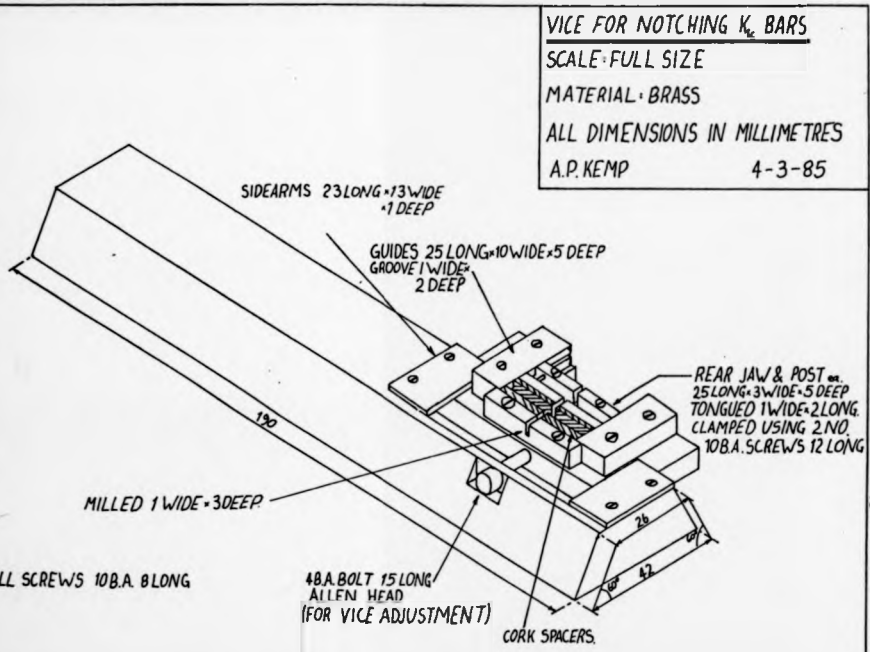

Figure 3.50. Drawing of notching vice used to prepare SENB K_{Ic} specimens.

Figure 3.51. Drawing of 4-point bend jig constructed to perform valid fracture toughness tests.

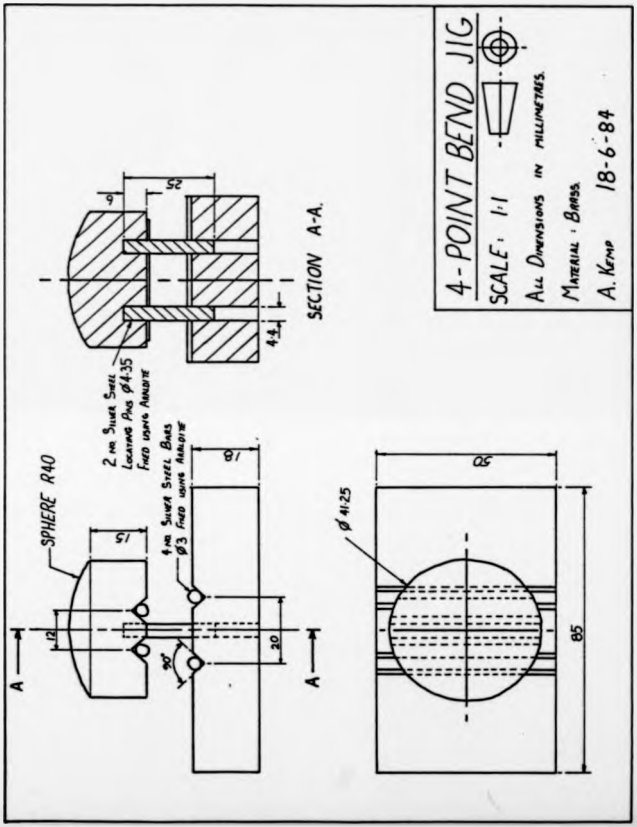

Table 3.8 Comparison of Fracture Toughness Values for Glassy Borax (AB) Using a Saw Notch and a Vickers Indent as the Source of the Critical Flaw

Method of Crack Introduction	Value ($\times 10^5$ Pa $m^{\frac{1}{2}}$)
Notched beam, equations 2.6 and 2.7	2.93 ± 0.01
Indentation, equation 2.11	0.31 ± 0.02
Indentation, equation 2.12	0.78 ± 0.01

3.4.4 Fractographic Analyses

In an attempt to understand the fracture processes occurring in these materials, the fracture surfaces were examined in a Scanning Electron Microscope (SEM). A selection of the photographs taken are shown in Figures 3.53 - 3.60 to provide a flavour for the observed microstructures.

In all cases for the parent glasses, "fast" fracture was seen, characterised by the "clean" smooth fracture surface indicated in Figure 3.53, together with views of the damage produced during notching and cracks formed at the notch tip that were not responsible for the ultimate failure of the specimen [199], thereby providing a lower limit for the size of the critical flaw.

For the devitrified borax specimens, to which all comparisons here will be made, the effects of surface nucleation are readily apparent by reference to Figure 3.54. More detailed examinations of different aspects of the fracture surface are presented in this and other examinations. The general view (Figure 3.54a) serves to provide an overall view of the fracture, and to indicate the locations of these additional regions. Grain sizes are $\geq$ 0.5 mm, and the production of a "pipe" in the upper half of the fractured surface between the top corners indicates a "depletion region" created by the interpenetrating crystal growth near the centre of the bar. The large crystallites mask the effect of surface damage introduced during notching, and the weak bonding between them indicates a high degree of intergranular fracture, with associated "pullout", the surface containing the majority of a given grain extracting the remainder from the opposite side, as evidenced by Figure 3.54b, and the slowly-varying contours of the fracture surface in Figure 3.54a. Extraction of fibrils from a spherulite can occur in a similar manner if the crystal is oriented centrally with respect to the fracture path. This is demonstrated in Figure 3.54c.

3.4.4.1 Sodium Chloride Doped Glass-Ceramics

Spherulitic growth is again in evidence for NaCl dopants, the degree of which is reduced for increased NaCl concentrations. The fracture surface for the 10% NaCl doped devitrified material is shown in Figure 3.55. An increased tendancy towards transgranular fracture is demonstrated by the sharper flatter fracture surface (Figure 3.55a), and the stepping thought to show the fibrils within a spherulite in Figure 3.55b. The nucleation properties appear

Figure 3.52. Load-displacement curves obtained during strength tests of glassy and devitrified NaCl-doped materials.

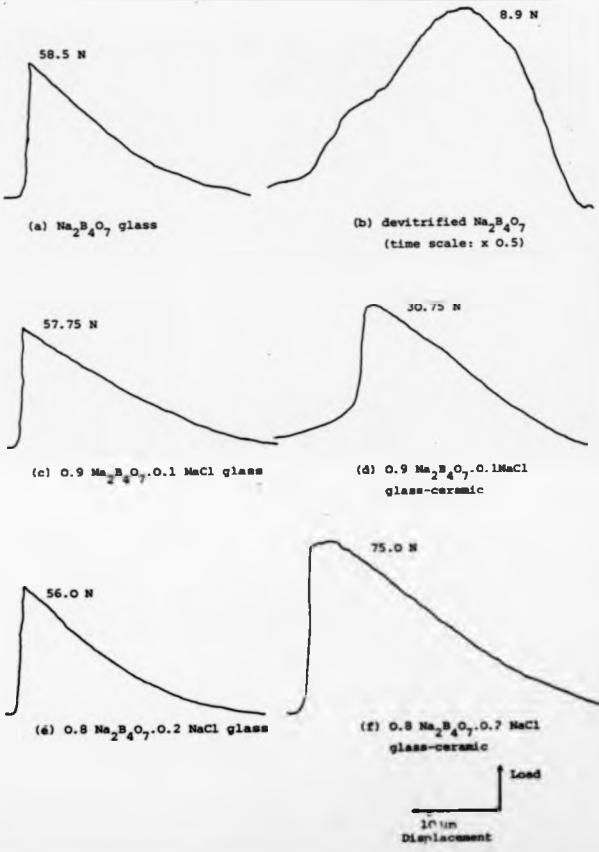

Figure 3.53. Typical fracture surface of a $99Na_2B_4O_7.1P_2O_5$ glass K_{1c} specimen.

Figure 3.53a. General view, showing "clean" fracture surface.

Figure 3.53b. Close-up of notch root showing sub-critical flaw 50 μm long.

Figure 3.54. Fractographic analysis of a devitrified $Na_2B_4O_7$ glass.

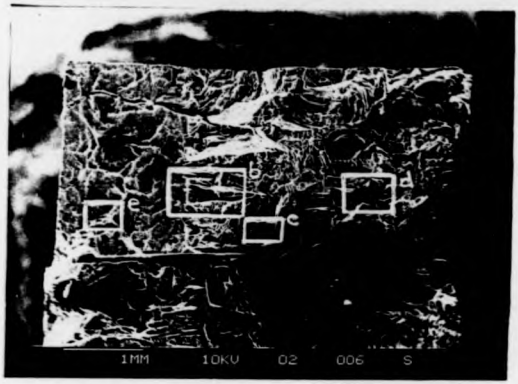

Figure 3.54a.

General view. Irregular surface implies that intergranular fracture is occurring along the boundaries between spherulites.

Figure 3.54b.

Notch root, showing grain pullout.

Figure 3.54c.

Fracture surface showing extraction of fibrils from within an individual spherulite.

Figure 3.54d.

Fracture surface implying intergranular fracture around spherulites.

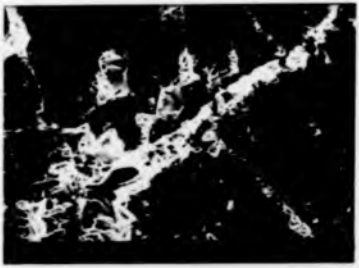

Figure 3.54e.

Notched area. Damage from the saw cut has been masked by the large crystallite sizes.

Figure 3.55. Fractographs of a $90Na_2B_4O_7.10NaCl$ glass-ceramic.

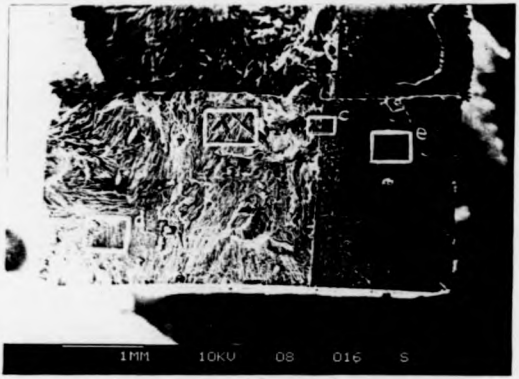

Figure 3.55a. General view. Lack of large scale topography implies transgranular fracture.

Figure 3.55b. Fracture surface. The stepping is thought to be due to crack branching within a spherulite.

Figure 3.55c.

Notch root. The stepped effect is again probably due to cracking within a spherulite.

Figure 3.55d.

Fracture surface showing interpenetration of fibrils from spherulites.

Figure 3.55e.

Notched region. Damage from the saw is again not visible. The fibrillar patterns are nominally the same size as abrasion from the saw blade.

to have been enhanced since a finer grained microstructure is observable on the notch surface (Figure 3.55c), however there are no cracks visible emanating from the notch.

Estimates for the critical flaw size cannot be obtained for the 20% NaCl-doped glass-ceramics either, even though a microscopic distribution of small crystallites may be observed (mean crystallite size ~ 40 μm). On a more macroscopic level, a high quantity of residual glass was in evidence. The thermal expansion mismatch was presumably responsible for the cracking within the glass (Figure 3.56b), and the corresponding compressive stresses from the glass on the crystal that has significantly increased the toughness, in an analogous manner to zirconia toughening in alumina ceramics [200,201]. The incomplete crystallisation is an extension of the multiple phase glass argument presented in section 3.1.1. The presence of spherulites, although greatly reduced, is still in evidence by reference to Figure 3.56c.

3.4.4.2 P_2O_5-Doped Materials

Extensive porosity (~ 1 mm ϕ) is observable in the fracture surfaces of lightly-doped specimens (Figure 3.57), which appears to reduce in both size and distribution for higher P_2O_5 concentrations. This is coupled with an increased stability in the glass phase. Therefore one may postulate that the pores arise from P_2O_5 volatilisation at low concentrations during devitrification in an attempt to form a stable crystalline phase. If this explanation is valid, then the inside of the pores should be phosphorus rich when subjected to energy dispersive analysis of the characteristic X-rays (EDAX) in the SEM. This was not found, however no alternative explanation can be presented for this behaviour.

3.4.4.3 TiO_2-Doped Materials

At low TiO_2 concentrations, a material containing a high density of small cigar-shaped pipes (~ 1.5 μm long, areal fraction $A_A \approx 10\%$ [157]) within a fine microstructure was obtained, with what appears to be large regions of residual glass remaining at higher concentrations. For increasing TiO_2 content, the pipes appear to coalesce to form voids, which may be the cause of the deleterious effect on mechanical strength.

Figure 3.56. Fractographs of an $80Na_2B_4O_7.20NaCl$ glass-ceramic.

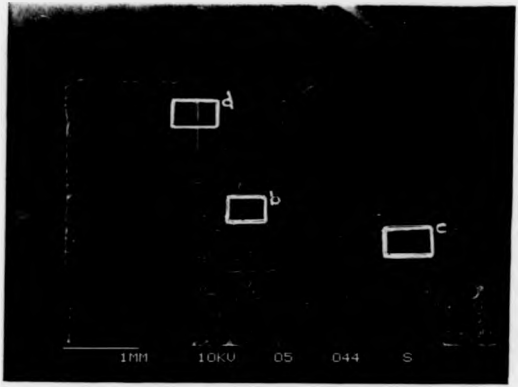

Figure 3.56a. General view. Striations occur from a presumed compositional inhomogeneity in the parent glass. The macroscopically flat surface is indicative of a high degree of transgranular fracture.

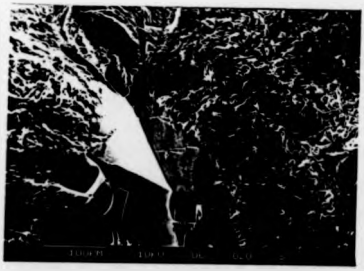

Figure 3.56b. Fracture surface, showing distinct boundary between glass and glass-ceramic. Glassy region is cracked at the interface, reinforcing the argument of compressive pre-stressing via the thermal expansion mismatch.

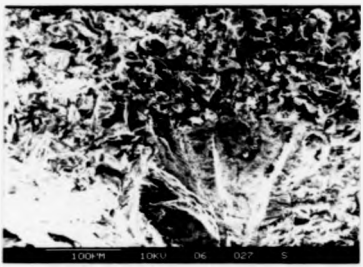

Figure 3.56c. Fracture surface, showing presence of limited spherulitic growth. The microscopic grain pullout again implies a degree of slow fracture.

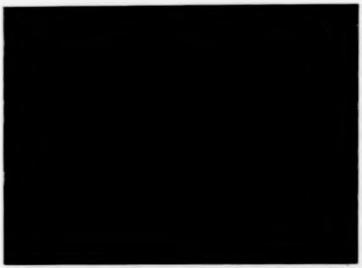

Figure 3.56d. Notch root, showing damage from saw on top of a fine-grained microstructure. Sub-critical flaws are again absent, presumably being masked by the cracks present along glass-crystal interfaces.

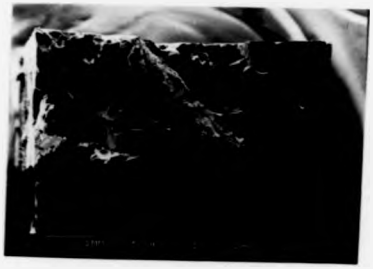

Figure 3.57.

Fracture surface of a devitrified $99Na_2B_4O_7 \cdot 1P_2O_5$ fracture toughness specimen. Extensive porosity is apparent.

At the 2% dopant level, the 2-stage heat treated material still contained a residual glass "core" (Figure 3.58), which was replaced by a finer microstructure and a nominal degree of piping using the 3-stage heat treatment.

For the 5% dopant level, the residual glass was also manifest in the form of a series of sheets sandwiched between the crystalline layers, the reason for which is not obvious. Large scale cracking within the specimens was present throughout.

3.4.4.4 Platinum Nucleated Materials

Unfortunately, all specimens fractured beneath the minor span loading points and not at the notch, which when combined with the larger than usual crystallite dimensions (> 2 mm) and the excessive piping (Figure 3.59) make fractographic examinations pointless. These considerations are certainly responsible for the large "natural" flaws and hence the poor toughness values.

3.4.5 Sodium β" alumina

In an attempt to assess the improvement in mechanical properties for the haloborate glasses and glass-ceramics examined in this work, specimens were prepared from a commercial β"- alumina ceramic so that intrinsic property comparisons can be made.

It has been established that the measured mechanical properties are dependent upon sample preparation (section 3.4.6.2). Therefore, until corrections can be made for the effect of surface damage, physical property comparisons must be made on an intrinsic basis, i.e. all specimens subjected to a similar machining process.

To this end, samples of a commercial β"-alumina ceramic were prepared in the manner outlined in section 3.1.3 from a HIPed solid electrolyte tube manufactured by Chloride Silent Power Ltd. for degradation studies. The wall thickness led to a reduction in width B below the 2.5 mm normally used. Results obtained are summarised in Table 3.9. A fractographic examination (Figure 3.60) showed a uniformly distributed microstructure containing fine (< 20

Figure 3.58.

Fracture surface of a devitrified $98Na_2B_4O_7.2TiO_2$ fracture toughness specimen. Incomplete crystallisation is demonstrated by the residual glass "core". The difference in thermal expansion coefficients is responsible for the cracks nucleating from the interfacial boundary.

Figure 3.59.

Fracture surface of a devitrified $Na_2B_4O_7$ + 10^{-4} mol% Pt fracture toughness specimen. Poor nucleation is indicated by the appearance of large crystallites and extensive piping.

Figure 3.60. Fractographic analysis of a commercial β'' - Al_2O_3 ceramic.

Figure 3.60a.

General view of fracture surface. Transgranular fracture is implied by the macroscopically flat surface.

Figure 3.60b.

Close-up of notch root, showing a sub-critical crack of length ~400 μm, in a manner analagous to those previously observed in glassy specimens.

Figure 3.60c.

Fracture surface, indicating transgranular fracture in a two- or more phase microscopic material.

Table 3.9 Summary of Material Properties Determined for a Commercial β''-Al_2O_3 Ceramic

K_{I_c} = (0.762 ± 0.026) MPa $m^{\frac{1}{2}}$

E = (4.9 ± 0.2) GPa

H = (6.6 ± 0.4) GPa

ρ = 1770 kg m^{-3}

α = 77.0 K^{-1}

μm) crystallites (Figure 3.60c), with sub-critical flaws being readily visible at the notched root (Figure 3.60b).

3.4.6 Interpretation of Mechanical Property Measurements

3.4.6.1. Overview

A precursory examination of the K_{1c} values presented in Table 3.7 indicates a high degree of accuracy in the measurements in the majority of cases. For the glassy samples, an error of < 3% is reported in all cases, whilst an increased scatter, generally < 7%, is present for the devitrified materials. The larger errors, ~15%, are obtained for the conventionally polished (5 and 15 mol% NaCl dopant) and very poorly nucleated (P_2O_5 doped AB and AB itself) devitrified materials. The K_{1c} values for the poorly nucleated specimens may be more widely varying due to the increased population of large flaws which may interact more easily with the stresses experienced during measurement. The "conventionally polished" specimens however exhibit comparitively good nucleation characteristics and therefore these measurements may be a partial justification for the polishing criterion postulated and employed during this work. The reason for the low deviation in K_{1c} values for the glassy materials is not understood. However it would appear from this result that the effect of surface prestressing via polishing is reduced for glassy materials.

As a check of the overall continuity of the mechanical property data, AB bars, in both devitrified and glassy states, were prepared with each batch of specimens as a control. Whilst the crystalline material produces comparable values within experimental error, probably being a result of the large flaws created during the crystallisation process as indicated above, the glassy specimens show a marked difference, being ~1/3 higher for the second "set" of measurements designed to investigate the properties of "classically" nucleated materials. This may be due to improvements in the preparation techniques gained by experience obtained during prepatation of the NaCl - doped specimens.

The Young's modulus values follow a similar trend to that of the K_{1c} for the glassy specimens, being lower for the NaCl - doped materials than for the "conventionally nucleated"

glasses, with the notable exception of the Pt - nucleated bars. It is postulated in the accepted description of classical nucleating agents that platinum enters the network as metallic grains and plays no active structural role. However, the more elastic behavior of this "family" of glasses would seem to indicate that this explanation is highly inaccurate for sodium borate systems, although quantitive inferences cannot be made since there is no correlation of elastic modulus with added platinum content.

Examination of the data obtained for the devitrified specimens, which should provide a quantitative measure of the characteristics of the crystal phases present, is complicated by the extreme differences in crystallite size and volume fraction. Qualitatively the "classical" nucleating agents yield essentially constant values, ~1.8 - 1.9 GPa, a decrease by a factor ~2.5 compared to values for the parent glass, although there are significant chemical and concentration-related deviations from this generalisation.

Comparisons of the Pt - nucleated specimens to trends observed in their glassy analogues are not possible since the crystallized bars were too fragile to permit reliable experiments to be performed. The physical property enhancement obtained for devitrified NaCl - doped materials is once again demonstrated, the values consistently increasing with increasing NaCl concentration.

Turning attention now to the hardness values, further justification of the adopted polishing criterion might be expected, with the 'conventionally polished' specimens providing higher values due to the postulated increse in surface stresses. This is not observed, however, values being essentially constant for both glassy and crystalline states, approximately equal to 3.5 GPa and 1.5-2.0 GPa respectively with effects due to the individual nucleating agents superposed on the individual specimen groups, generally producing reduced hardness values for increased dopant concentration. The properties of the crystalline material are once again shown to be inferior to those of the glass, with the exception of the NaCl - doped specimens, where increasing NaCl content leads to an increased resilience of the material to withstand applied stress, by reference to K_{1c} and Young's modulus values.

It has been shown previously [197] that hardness is a relatively insensitive probe of surface prestressing in ceramics; therefore the inferences presented from this aspect of the work do not directly contradict the newly-adapted polishing criterion.

The differences in property measurements with changing dopant concentrations will be discussed in more detail for each additive in the following sections.

3.4.6.2 NaCl

As shown in Table 3.7, the addition of chloride slightly decreases the K_{1c} value of the base glass, but increases the toughness of the devitrified material quite dramatically, exceeding that of the glass at the 20% NaCl level. If the K_{1c} deterioration presented by Lawn et al. [127] is extended from the introduction of the critical flaw using a Vickers indent to a saw cut in a 4-point bend, then the $(P/C_o^{3/2})$ term in equation (2.23) can be considered to be a measure of the elastic-plastic deformation zone. By reference to Young's modulus, fracture toughness and hardness values (Table 3.7), the deformation zone may be seen to decrease with NaCl concentration for the glass-ceramic. The implication of this hypothesis for the glass is of an essentially constant elastic-plastic deformation zone, hence the length of the critical flaw remains constant. This is verified by the sub-critical flaw lengths measured in the SEM.

The trends in mechanical property measurements summarised above may also be explained by the observed changes in the microstructures of these devitrified glasses with increasing NaCl content.

One further point of note is a partial justification of the polishing criteria outlined in section 2.3.4. One preparation of notched samples for 5 and 15% NaCl materials using the conventionally adopted criteria was made, producing the results shown at the bottom of Table 3.7. As can be readily observed by comparison with data obtained for 10 and 20% NaCl samples, significantly increased toughness values were obtained having a higher percentage scatter. This may be consistent with the hypothesis of incomplete surface stress relief during polishing (section 2.3.4), although it seems somewhat surprising to the author that such a large increase in

toughness may be solely due to a compressive stress at the sides of the specimen. If this were so, crack propagation might be expected to show large differences from surface to bulk on examination of the fracture surfaces. However, there is no discernable experimental evidence from examination of the fractographs discussed in section 3.4.4 to support this.

3.4.6.3 P_2O_5

In this instance, P_2O_5 addition appears to marginally increase the toughness of the glass, indicated by reference to Table 3.7. However, the toughness can be seen to linearly decrease for the materials that would devitrify throughout the bulk. This observation would appear to be consistent with the P_2O_5 nucleation mechanism(s) [12,163], namely that P_2O_5 enters the glass matrix (and in this instance, appears to stabilise it in low concentrations), and then aids nucleation either by undergoing microscopic phase separation on heat treatment (perhaps giving rise to a change in the optical characteristics, such as the 'colourless-dark' transition in Figure 3.5) or perhaps on addition of excess quantities, sites of stress concentration are created [13]. These phase separated regions may re-distribute upon heat treatment either to give sites of sufficient size to be stable to crystallisation or, if the upper consulate temperature is surpassed, a single stable phase [12]. Therefore, if the first interpretation is correct, then the number density of these droplets (assuming the size remains constant) will increase - linearly with P_2O_5 content, which would explain the trend in strength values of the heat treated material if the second phase is mechanically weaker than the crystal phase(s) formed in the absence of a nucleating agent.

Here, unlike the case of sodium chloride, the trends exhibited for the crack lengths and the mechanical properties are borne out by trends in E and H for both glassy and heat-treated samples.

3.4.6.4 TiO_2

Out of the nucleating agents examined in the present work, TiO_2 is the most anomalous. At low dopant levels, two types of heat treated material were obtained: a 'translucent' form,

having very poor microstructure and very little mechanical stability, and a white polycrystalline form containing < 25% glass which was processed to obtain the presented data.

Dilatometric information implied the production of a second crystal phase, culminating at ~ 580°C, and so the three stage heat treatment already discussed was employed to examine its properties, the final product being a crystalline material containing striations of what appeared to be a second crystal phase. This observation is consistent with the concept of chemical phase separation presented in section 3.1.1. Interestingly, the enhanced mechanical properties afforded by the three stage schedule show an opposite trend to the two stage heat treatment, decreasing with increasing TiO_2 content. The high toughness values obtained for the 2% TiO_2 material subjected to the three-stage heat treatment could not be seen to be improved further by investigation of lower TiO_2 dopant concentrations due to the uncontrolled devitrification observed at the 1% dopant level.

3.4.6.5 Platinum

Unfortunately, upon crystallisation of the 10^{-3} mol % Pt-doped glass, a series of open intergranular cracks developed, thereby making machining very difficult and certainly unproductive. Therefore, a justifiable comparison of properties is difficult, and trends cannot be inferred.

Again, a broad maximum exists for K_{1c} as a function of concentration for the glass, which subsequently takes the form of a minimum in the devitrified material (taking the 10^{-3} mol % doped samples to have a toughness of effectively zero); both sets of values becoming poor, even when compared to the other doped glasses. Hardness and Young's modulus values are comparable with the other materials investigated in the present work.

CHAPTER FOUR

DISCUSSION

This and other work has demonstrated an increase of about 3 orders of magnitude in measured ionic conductivity values under ambient conditions in haloborate glasses upon conversion to the glass-ceramic. Comparable conductivity values at the proposed operating temperature of the sodium-sulphur cell (~ 350°C) were obtained, but the low T_g values of the glassy materials would seem to preclude their commercial exploitation. There are three explanations possible for this increase, namely the formation of a highly conducting crystalline phase, grain boundary conduction or the rejection of halide, cation or both into the residual glass to form a more highly conducting glass matrix.

It is the first which is most favoured following the early work by Daniels [9], who has shown the crystal phase to be more highly electronically conducting from charging experiments in the SEM. However, it is unclear to the author what microscopic details in any of these models would account for the observed behaviour, namely higher measured conductivities in the glass-ceramic at lower temperatures, with approximately equal conductivities at elevated temperatures. It may be expected that the higher conductivities would continue to be observed for the devitrified materials at a rate equal to or exceeding those of the parent glass with increasing measurement temperature. The fundamental question of the difference between the two states responsible for this discrepancy remains.

Infra-red and Raman studies have shown little difference in this respect, apart from the sharpening of the spectra in the crystalline state associated with a net increase in local periodicity. In all previously reported cases this argument results in a decrease in measured conductivity [9], or at most, a comparable value. Irion et al. [106] measured the conductivity of a lithium chloroborate mineral, boracite, and found a factor of ~ 5 increase in the conductivity compared with a glass of an equivalent stoichiometric composition.

Previous work [9] has shown the presence of the added halide to play a significant role in this conductivity anomaly observed in the sodium, alkali earth and mixed cation haloborate systems, and postulated a subtle unspecified structural reorganisation as the underlying cause. It was proposed that this reorganisation caused a reduction in both electrostatic and lattice strain energy barriers from the viewpoint of the Anderson-Stuart model.

One possible explanation of the observed conductivity enhancement in the polycrystalline materials may be inferred from infra-red spectroscopic results. Here, the presence of direct B-Cl bonding is postulated, which may form a more open host network due to the chlorine atom being directly bonded into the structure.

If B-Cl bonding is in evidence, then there will be an increased number of non-bridging oxygens in the network, which would result in a decrease in "flow" related properties with increasing halide content. Such measurements are difficult to perform on the isolated crystal phase from the viewpoint taken in this work.

A converse argument, of the halide 'stuffing' the crystal structure, hence increasing the overall rigidity and consequently the viscosity would imply the occurrence of a conductivity minimum with increasing halide content. This idea may be visualised as the structure being opened by the halide at low dopant concentrations to increase the number and size of the conducting channels. However with increasing dopant content, the channels will now become blocked, thus increasing the conductivity once more. This phenomenon has been observed in the $Na_2B_4O_7$-$MnCl_2$ system. Unfortunately T_g or viscosity values do not exist to provide support for the presented hypothesis.

The final point regarding conductivity data concerns the brief investigation of a haloborate glass-ceramic. The results obtained from using frequency response analysis showed an apparently progressive electrode dissolution reaction to be in evidence. Predictions for the corresponding time-domain response from this behaviour compare well with the experimentally determined increase in the "d.c." current with increasing voltage application time.

Previous work has indicated an apparently non-systematic hysteresis effect in the conductivity values of glass-ceramic specimens for subsequent temperature scans. Comparable behaviour may be inferred from this work, although a phase transition not reported previously at ~280°C was also in evidence. Later attempts to determine optimum values in a more comprehensive analysis will be hampered by the lack of an appropriate equivalent circuit.

A recent Magic Angle Spinning (MAS) NMR study (Appendix 3) on the $Na_2B_4O_7$-NaCl system of materials has shown crystalline borax contain 4 crystallographically distinct sodium sites, an observation which is borne out by an early X-ray structure determination [199]. The spectrum of highly-doped chloride-containing crystalline compounds shows only 3 sites, in different concentrations to those in the more complex spectrum of the base material. Comparison of this spectrum with those from pure oxide-containing systems having equivalent anion and cation concentrations (i.e. not showing the above mentioned conductivity anomaly) indicate that conduction occurs from one or two of these sites. It is the third (eliminated) site that is observed in the poorly conducting analogues.

This may be consistent with the X-ray diffraction experiments performed in this work, since changes in the diffraction patterns for crystalline AB and the halogen-doped analogues were observed. However, these changes varied for diffraction patterns obtained from different instruments. Further investigations are required to understand this discrepancy. More specific information may be obtained from high temperature diffraction studies. Unsuccessful efforts were made during the course of this work to commission such equipment.

Optical (Infra-Red and Raman) spectroscopy which should be sensitive to changes in local environment, also showed some variations in the materials with increasing halide content, although no inferences regarding the changes in structure responsible for the enhanced conductivities from the glassy to crystalline states could be made. This is surprising, since thermal expansion data, which also reflects effects of molecular motion, changes quite significantly (by a factor ~3) for the base material, $Na_2B_4O_7$, for the glass and its heat treated analogue.

It is hoped that the situation may be investigated further by examination of mixed alkali compounds. This examination would comprise low frequency conductivity, Tubandt measurements and MAS NMR. If the concentration of each conducting ion is identified from Tubandt measurements, and the characteristics of the conduction path deduced from conductivity measurements, then this could be related to the concentration of ions at each site determined via NMR.

This investigation may complement the forthcoming structure determination of the crystalline sodium chloroborates by neutron diffraction, where the conduction path may be inferred by the size of the "gaps" within the crystal structure.

It is hoped that the conclusions of this investigation will enable the conduction process to be determined and understood. The properties of this material may then be optimised in terms of the ionic conductivity and chemical stability that may be expected in service in a [illegible] environment.

To obtain a high quality material from the viewpoint of controlled nucleation and crystallisation, combined with good mechanical properties and high measured conductivities, it would seem that future efforts should be concentrated on materials doped with both NaCl and TiO_2. Results obtained during the course of this work show NaCl-doped materials to have high mechanical strength and good conductivity but poor nucleation characteristics compared to samples doped with TiO_2. However the addition of TiO_2 appears to have a deliterious effect upon toughness. Conversely artificially high toughness values, not indicative of the crystal phase, may have been obtained for the NaCl-coped test specimens via the thermal expansion mismatch between the glass and crystal phases [13].

Finally, it would appear that the B_2O_3-NaCl binary system was provide both structural insight and high conductivities in the light of previous arguments. Early work by Dimicz and Scheidt [175] has shown the formation of a single phase material in this system is not possible. A series of repeat experiments were performed in this work to attempt to gain comparative I-R and conductivity specimens, but also proved unsuccessful. At the highest NaCl concentrations, a

two-phase product was obtained: a soft green crystalline material identified as NaCl by XRD, and a colourless glass which exhibited the rapid hydrolysis characteristics of B_2O_3. It is therefore concluded that structural information must be obtained by appropriate experiments on ternary glasses.

CHAPTER FIVE
CONCLUSION

Due to the unavailability of an early conductivity measurement apparatus [9], a series of new experimental techniques have been employed and appropriate equipment constructed to investigate the ionic conductivities of chloroborate glasses and glass-ceramics. The final apparatus, using frequency response analysis, appears to be the most promising in the attempt to perform valid measurements of ionic conductivity and model the conduction paths in these materials. A computer program to perform analyses of this data in terms of discrete electrical components and determine their optimum values has been written, and the initial trials of its generality and accuracy appear to be promising. Results from the analyses performed here on data acquired for a standard specimen, Coors alumina, indicate an apparent irreconcilable difference between permittivity values deduced from base equivalent circuit parameters obtained using models based on one and two distinct relaxation mechanisms.

A previously observed "hysteresis" effect in the crystalline halogen doped specimens has been observed, together with a previously undocumented "phase change" at ~ 280°C. In the runs performed to observe this phenomenon, behaviour consistent with electrode dissolution reactions was also observed. No explanation has been presented to account for this behaviour. The anomalous responses observed with the glass-ceramic specimen appears to be qualitatively consistent with the observations which led to the cessation of earlier measurements employing a time domain technique.

A new apparatus employing a modification of standard transport number measurements has been constructed to determine the transport number of each conducting species present in these materials. Measurements performed on a β-Al_2O_3 ceramic specimen appear to yield measurable differences in ion concentration at the extremities of the specimens tested. The calculation of transport numbers, has however, yet to be performed. Since this alternative technique employs a different working viewpoint from methods in current usage (i.e. the

measurement of ion "flow" from a good source of the primary conducting ion to an equally good sink) then a revised analytical method is required.

A new process for converting surface nucleating glasses into fine-grained glass-ceramics has been developed and successfully used in the production of haloborate glass-ceramic tubes for degradation studies. Simple experiments have shown the particle size and chemical species of the surrounding particulate medium to have a pronounced effect upon the general appearance of the finished product.

For the "conventionally" prepared glass-ceramic specimens used in mechanical strength testing, control over the nucleation and growth process has not been attained, with the production of voids, pipes and small cracks producing the deliterious effects on measured toughness values. In an effort to rectify this situation, an extensive study has been performed to attempt to determine an optimum heat treatment schedule. This investigation proved unsuccessful.

A complementary series of experiments which examined the effects of concentration of a selection of the most common nucleating agents on the crystallisation properties has also been performed. The greatest control over the crystal growth kinetics was found for low (~ 2 mol %) concentrations of TiO_2. The effects of metallic platinum as a nucleating agent were seen to have detrimental effects upon the mechanical properties of both the glass and the converted glass-ceramic.

For the poorly nucleating materials, significant problems in machining the highly brittle yet fragile specimens were encountered. New techniques have been developed and appropriate equipment constructed to overcome these difficulties.

The optimum toughness values obtained, for the 20 mol % NaCl doped glass-ceramic specimens, have been found to exceed one half the value measured for a commercial sodium β''-alumina ceramic. For such a poorly nucleating simple glass system this result is felt to be most encouraging, since other more complex base glasses will undoubtedly increase this value substantially with the production of tougher crystalline phases and associated control over

nucleation behaviour almost certainly obtained. The postulated solution to the engineering problem of reducing the degradation at the insulating seal in a sodium-sulphur cell simply by introducing a graded seal having no halogen with comparable thermal expansion behaviour in the glass and glass-ceramic would appear to demonstrate the versatility and future applicability of these materials in high-temperature batteries.

CHAPTER SIX
FUTURE WORK

The equipment development necessary to further investigations of this unusual glass system is essentially complete. Future areas of research can now be carried out on mechanical, structural and microscopic levels.

1. The bulk nucleation properties of other mixed alkali and mixed halide borate-based systems can be investigated, and the corresponding effects upon mechanical and electrical properties determined. The link between these two types of measurement may be expressed in terms of volume fraction and mean crystallite size of the crystal phase(s). The most promising area of study would seem to be in the AB-NaCl-TiO_2 ternary system.

2. A strategy for the measurement of transport numbers in these systems has been formulated; which when completed, may complement the conductivity measurements in a fuller understanding of the applicability of the mixed alkali effect to halide containing glasses and glass-ceramics. This may require a more general investigation of silicate or phosphate glass systems, which if necessary may be used to present an alternative model.

3. To determine the crystal structure of the conducting phase, examine presented data on the extent of B-Cl bonding and interpret its relevance to the conduction mechanism. This may complement an MAS NMR study of the sites within the lattice responsible for conduction.

4. An understanding of the observed three orders of magnitude increase in the room temperature conductivity of the single glass-ceramic specimen investigated in the current work is felt to be important, and to determine if this effect may be extended to higher temperatures (~ 300 - 350° C), so that these materials may become good commercial competitors to the β''-Al_2O_3 electrolyte currently favoured for use in the Na-S cell.

5. A modification to the method of strength testing could be introduced, by measuring the breaking strengths of electrolyte tubes manufactured in a vertical melt casting apparatus.

6. Finally, to perform an in-depth microscopic study of the surface nucleation effect observed in these materials by examination of different powders and possibly again extend studies to other glass systems.

REFERENCES

1. "Modern batteries. An introduction to electrochemical power sources". C.A. Vincent et al. (eds.) Edward Arnold 1984.
2. R.A. Huggins, "Crystal structures and first ion conduction", in "Solid electrolytes. General principles, characterisation, materials, applications." Chapter 3 (p. 28) P. Hagenmuller and W. Van Gool (eds.) Academic Press 1978.
3. W.D. Kingery, H.K. Bowen, D.R. Uhlmann, "Introduction to Ceramics", Wiley 1976.
4. G.J. May, S.R. Tan, I.W. Jones, J. Mat. Sci. 15 (1980) 2311.
5. P.S. Nicolson, "The deterioration of sodium α/β" alumina electrolytes in sodium environments". in "Progress in solid electrolytes", eds. T.A. Wheat, A. Ahmad, A.K. Kuriakose, Energy, Mines and Resources, Ottawa, Canada, ERP/MSL 83-94 (TR) 1983.
6. C.C. Hunter, M.D. Ingram, Solid State Ionics 14 (1984) 31.
7. F.Y. Tsang, U.S. Patent 3829331.
8. S. Badzioch, European Patent 0079228 A1.
9. P.B. Daniels, Ph.D. Thesis, University of Warwick 1984.
10. W.H. Zachariasen, J. Am. Ceram. Soc. 54 (1932) 3841.
11. J. Wong, C.A. Angell, "Glass structure by spectroscopy", Dekker, 1976.
12. P.W. McMillan, "Glass ceramics" Academic Press 1979.
13. B.R. Lawn, T.R. Wilshaw, "Fracture of brittle solids", Cambridge University Press 1975.
14. C.H.L. Goodman, Postgraduate lecture notes, University of Warwick 1983.
15. H. Spaehn, "Electrochemical fundamentals of corrosion fatigue", Chapter 10 in "Subcritical crack growth due to fatigue, stress corrosion and creep", L.H. Larsson (ed.) Elsevier 1981.
16. Yu. Ya. Gurevich, A.K. Ivanov-Shits, Institute of electrochemistry, Academy of Sciences of the USSR, Moscow. Trans. from Elektrokhimiya, Vol 16 pp 3-22, 1980. Plenum.
17. A.J. Dekker, "Solid state physics", Macmillan 1981.
18. D.A. Fraser, "The physics of semiconductor devices", Clarendon 1979.
19. "Physics of dielectric solids", C.H.L. Goodman (ed.) Conference Series no. 58, Institute of Physics 1980.
20. W. Van Gool in "Solid electrolytes. General principles, characterisation, materials, applications" Chapter 2 (p. 9), P. Hagenmuller, W. Van Gool (eds.) Academic Press 1978.
21. P. McGeehin, A. Hooper, J. Mat. Sci. 12 (1977) 1.
22. H. Rawson, "Properties and applications of glass", Glass Science and Technology 3, Elsevier 1980.
23. D.J.H. Atkinson, P.W. McMillan, J. Mat. Sci. 11 (1976) 994.

24. Y. Haven in "Solid electrolytes. General principles, characterisation, materials, applications" Chapter 5 (p. 59), P. Hagenmuller, W. Van Gool (eds.) Academic Press 1978.

25. H. Jain, J. Non-Cryst. Sol. 66 (1984) 517.

26. R. J. Elliott, A. F. Gibson, "Solid State Physics", Macmillan 1976.

27. G. Couturier et al., Solid State Ionics 9 and 10 (1983) 699.

28. J.O. Isard, J. Sci. Instrum. 40 (1963) 403.

29. F.R. Conner, "Noise", Edward Arnold 1982.

30. H. Mitomo, V. Uemura, J. Mat. Sci. Lett. 16 (1981) 552.

31. J.L. Piguet, J.E. Shelby, J. Am. Ceram. Soc. 68 (1985) 450.

32. M.J. Hyatt, D.E. Day, J. Am. Ceram. Soc. Comm. 70 (1987) C-283.

33. T. Minami, T. Shimizu, M. Tanaka, Solid State Ionics 9 and 10 (1983) 577.

34. D. Hayward, M. Gawayne, B. Mahboubian-Jones, R.A. Pethrick, J. Phys. E. Instrum. 17 (1984) 683.

35. "Standard method of test for electrical resistance of ceramic materials at elevated temperatures". ASTM D1829-66.

36. "Standard method of test for a-c loss characteristics and dielectric constant (permittivity) of solid electrical insulating materials", ASTM D150-74.

37. A.P. French, "Vibrations and waves", Nelson 1978.

38. R. Coelho, "Physics of dielectrics for the engineer", Fundamental studies in engineering V1, Elsevier 1979.

39. A.K. Jonscher, Nature 253 (1975) 717.

40. A.K. Jonscher, J. Mat. Sci. 13 (1978) 553.

41. A.K. Jonscher, in "Physics of dielectric solids", C.H.L. Goodman (ed.) Institute of Physics, Confrence series 58, 1980.

42. R.H. Cole, in "Physics of dielectric solids", C.H.L. Goodman (ed.) Institute of Physics, Conference series 58, 1980.

43. D.P. Almond, C.C. Hunter, A.R. West, J. Mat. Sci. 19 (1984) 3236.

44. R. Syed, D.L. Gavin, C.T. Moynihan, A.V. Lesikar, Comm. Am. Ceram. Soc. 64 (1981) C-118.

45. K.K. Mallick, Ph.D. Thesis, University of Sheffield 1988.

46. J.R. Macdonald, A. Hooper, A.P. Lehnen, Solid State Ionics 6 (1982) 65.

47. Y.T. Tsai, D.H. Whitmore, Solid State Ionics 7 (1982) 129.

48. M.J. Verkerk, B.J. Middelhuis, A.J. Burggraaf, Solid State Ionics 6 (1982) 159.

49. J.C. Wong, N.J. Dudney, Solid State Ionics 18 and 19 (1986) 112.

50. D.B. Wiles, R.A. Young, J. Appl. Cryst. 14 (1981) 149.

51. P. Rudolf. A. Clearfield. Acta Cryst. B41 (1985) 418.

52. R. Shirley, "Methods and applications in crystallographic computing", S.R. Hall, T. Ashida (eds.) Clarendon Press 1984.

53. E.A. Davis, S.R. Elliott, G.N. Greaves, D.P. Jones in "The structure of non-crystalline materials", P.H. Gaskell (ed.), Taylor & Francis 1977.

54. P.H. Gaskell, Phil. Mag. 32 (1975) 211.

55. C.H.L. Goodman, Phys. Chem. Glasses 27 (1986) 27.

56. T.M. Hayes in "The structure of non-crystalline materials 1982", P.H. Gaskell, J.M. Parker, E.A. Davis (eds.) Taylor & Francis 1983.

57. L.H. Freeman, A. Howie, A.B. Mistry, P.H. Gaskell, in "The structure of non-crystalline materials", P.H. Gaskell (ed.), Taylor & Francis 1977.

58. K. Hulls, Ph.D. Thesis, University of Warwick 1970.

59. H. Hagiwara, R. Oyamada, T. Kurosawa, T. Yagihashi, J. Electrochem. Soc. Japan 37 (1969) 193.

60. R. Dupree, N. Ford, D. Holland, Phys. Chem. Glasses 28 (1987) 78.

61. B.M.J. Smets, T.P.A. Lommen, J. Non-Cryst. Sol. 48 (1982) 423.

62. P.J. Bray, M. Levenstal, H.O. Hooper, Phys. Chem. Glasses 4 (1963) 47.

63. P. Tarte, M.J. Pottier, in "The structure of non-crystalline materials", P.H. Gaskell (ed.), Taylor & Francis 1977.

64. O. Yamaguchi, A. Narai, K. Shimizu, J. Am. Ceram. Soc. Comm. C-36 (1986).

65. J. Briscoe, B.E. Warren, J. Am. Ceram. Soc. 21 (1938) 287.

66. N. Valyashov, E.A. Porai-Koshits, Z. Krist. 95 (1936) 195.

67. H.P. Klug, L.E. Alexander, "X-ray diffraction procedures", Wiley 1954.

68. S. Rao, C.R. Houska, Acta Cryst. A42 (1986) 6.

69. S.W. Lovesey, "Theory of neutron scattering from condensed matter", Volume 1, Oxford University Press 1986.

70. J. Krogh-Moe, Phys. Chem. Glasses 6 (1965) 46.

71. E.N. Boulos, N.J. Kreidl, J. Am. Ceram. Soc. 54 (1971) 368.

72. W.L. Konijnendijk, Philips Research Reports Supplements 1 (1975) 1.

73. A. Abragam, "Principles of nuclear magnetism", Clarendon Press 1986.

74. P.J. Bray, J.G. O'Keefe, Phys. Chem. Glasses 4 (1963) 37.

75. P.J. Bray, F. Bucholtz, A.E. Geissberger, I.A. Harris, Nuclear Instruments and Methods 199 (1982) 1.

76. I.A. Harris, P.J. Bray, Phys. Chem. Glasses 25 (1984) 44.

77. H. Jain, H.L. Downing, N.L. Peterson, J. Non-Cryst. Sol. 64 (1984) 335.

78. P.J. Bray, A.E. Geissberger, F. Bucholtz, I.A. Harris, J. Non-Cryst. Sol. 52 (1982) 45.

79. J. Krogh-Moe, Phys. Chem. Glasses 3 (1962) 1.

80. P.J. Bray, R.V. Mulkern, E.J. Holupka, J. Non-Cryst. Sol. 75 (1985) 37.

81. I. Simon, in "Modern aspects of the vitreous state", J.D. MacKenzie (ed.), Butterworths 1960.

82. T.W. Bril, Philips Res. Reports Supp. 2 (1976) 1.

83. G. Hertzberg, "Infra-red and Raman spectra", van Nostrand 1968.

84. J. Krogh-Moe, Arkiv. for Kemi 14 (1959) 567.

85. G.J. Exarhos, W.H. Risen, Chem. Phys. Lett. 10 (1971) 464.

86. G. Hartlief, reviewed by S. Urnes, in "Modern aspects of the vitreous state", J.D. MacKenzie (ed.), Butterworths 1960.

87. A.J. Sturgeon, Ph.D. Thesis, University of Warwick 1987.

88. R.S. Krishnan, R. Srinivasan, S. Devanarayanan, "Thermal expansion in crystals", Pergamon 1979.

89. H. Rotger, in "Amorphous materials", R.W. Douglas, B. Ellis (eds.) Wiley-Interscience 1970.

90. "Differential thermal analysis" Volume 2, R.C. MacKenzie (ed.) Academic Press 1972.

91. Stolyar, Klyuev, Bulaeva, Soviet J. Glass Phys. Chem. 10 (1984) 291.

92. C.A. Angell, Solid State Ionics 18 and 19 (1986) 72.

93. J.H. Gibbs, in "Modern aspects of the vitreous state", J.D. MacKenzie (ed.), Butterworths 1960.

94. P.M. Wholan, M.J. Hodgson, "Essential principles of physics", John Murray 1974.

95. F.W. Sears, G.L. Salinger, "Thermodynamics, kinetic theory and statistical thermodynamics", Addison-Wesley 1975.

96. A.R. West, "Solid state chemistry and its applications", Wiley 1985.

97. J. Briscoe, B.E. Warren, J. Am. Ceram. Soc. 21 (1938) 287.

98. T. Abe, J. Am. Ceram. Soc. 40 (1952) 284.

99. K. Grjotheim, J. Krogh-Moe, reviewed by J. Krogh-Moe in Arkiv for Kemi 14 (1959) 553.

100. B. Beekenkamp and G.A. Yaminskii, V.V. Tarasov, reviewed by D.R. Uhlmann, R.R. Shaw, J. Non-Cryst. Sol. 1 (1969) 547.

101. J. Krogh-Moe, Phys. Chem. Glasses 3 (1962) 101.

102. J. Krogh-Moe, Arkiv for Kemi 14 (1959) 553.

103. D.R. Uhlmann, R.R. Shaw, J. Non-Cryst. Sol. 1 (1969) 547.

104. D. Kline, P.J. Bray, Phys. Chem. Glasses 7 (1966) 41.

105. T. Nishida, N. Kai, Y. Takashima, Phys. Chem. Glasses 22 (1981) 107.

106. T. Minami, Y. Ikeda, M. Tanaka, J. Non-Cryst. Sol. 52 (1982) 159.

107. M. Irion, M. Couzi, A. Levasseur, J.M. Rean, J.C. Brethous, J. Solid State Chem. 31 (1980) 285.

108. J.E. Gordon, "The new science of strong materials", Penguin 1976.

109. G.W. Hollenberg, G.R. Terwilliger, R.S. Gordon, J. Am. Ceram. Soc. 54 (1971) 196.

110. D. Hull, "Introduction to dislocations", Pergamon 1979.

111. T.P. Dabbs, B.R. Lawn, J. Am. Ceram. Soc. 68 (1985) 563.

112. H.L. Ewalds, R.J.H. Wanhill, "Fracture mechanics", Edward Arnold 1984.

113. D.M. Allen, Uncorrected preprint from 15th Int. Power Sources Symp. 1986.

114. B.F. Brown, "Stress corrosion cracking in high strength steels", U.S. Naval Res. Labs., Washington 1972.

115. B.R. Lawn, B.J. Hockey, S.M. Wiederhorn, J. Mat. Sci. 15 (1980) 1207.

116. T.A. Michalske, S.W. Freiman, J. Am. Ceram. Soc. 66 (1983) 284.

117. M. Inagaki, K. Urashima, S. Toyomasu, T. Goto, M. Sakai, J. Am. Ceram. Soc. 68 (1985) 704.

118. T.A. Michalske, E.R. Fuller, J. Am. Ceram. Soc. 68 (1985) 586.

119. H.E. Powell, F.W. Preston, J. Am. Ceram. Soc. 28 (1945) 145.

120. ASTM D 785-65 "Standard method of test for Rockwell hardness of plastics and electrical insulating materials".

121. D.N. Jarrett, P.W. McMillan, J. Phys. E. : Scientific Instruments 7 (1974) 913.

122. A.G. Evans, J. Am. Ceram. Soc. 65 (1982) 127.

123. D.B. Marshall, T. Noma, A.G. Evans, Comm. Am. Ceram. Soc. 65 (1982) C-175.

124. D.B. Marshall, J. Am. Ceram. Soc. 66 (1983) 127.

125. J.L. Henshall, C.A. Brookes, J. Mat. Sci. Lett. 4 (1985) 783.

126. B.R. Lawn, A.G. Evans, D.B. Marshall, J. Am. Ceram. Soc. 63 (1980) 574.

127. G.R. Anstis, P. Chantikul, B.R. Lawn, D.B. Marshall, J. Am. Ceram. Soc. 64 (1981) 533.

128. P. Chantikul, G.R. Anstis, B.R. Lawn, D.B. Marshall, J. Am. Ceram. Soc. 64 (1981) 539.

129. T.P. Dabbs, B.R. Lawn, Comm. Am. Ceram. Soc. 65 (1982) C-37.

130. Kimura, Yagasaki, Kunio, Eng. Pract. Mech. 19 (1984) 1025.

131. Ito, Tomozawa, Comm. Am. Ceram. Soc. 64 (1981) C-160.

132. T.A. Michalske, B.C. Bunker, J. Am. Ceram. Soc. 70 (1987) 780.

133. Ito, Tomozawa, J. Am. Ceram. Soc. 66 (1983) 765.

134. K. Kendall, N. McN. Alford, S.R. Tan, J.D. Birchall, J. Mater. Res. 1 (1986) 120.

135. J.F. Knott, D. Elliott, "Worked examples in fracture mechanics", Institution of Metallurgists 1979.

136. D.K. Shetty, A.R. Rosenfield, W.H. Duckworth, P.R. Held, J. Am. Ceram. Soc. 66 (1983) 36.

137. ASTM C 648-78. The breaking strength of ceramic tile.

138. J.E. Ritter, K. Jakus, A. Batakis, N. Bandyopadhyay, J. Non-Cryst. Sol. 38 and 39 (1980) 419.

139. J.L. Henshall, D.J. Rowcliffe, J.W. Edington, J. Mat. Sci. Lett. 9 (1974) 1559.

140. C.E. Turner, Imperial College, London, private communication.

141. D.K. Shetty, A.R. Rosenfield, W.H. Duckworth, Comm. Am. Ceram. Soc. 66 (1983) C-10.

142. B.R. Lawn, J. Am. Ceram. Soc. 66 (1983) 83.

143. J.E. Srawley, M.H. Jones, B. Gross, NASA TN D-2396 (1964).

144. B. Gross, J.E. Srawley, NASA TN D-3092 (1965).

145. B. Gross, J.E. Srawley, NASA TN-2603 (1965).

146. W.F. Brown, J.R. Srawley, ASTM S.T.P. 410 (1966).

147. S. Timoshenko, "Strength of materials", Van Nostrand 1958.

148. R.F. Cook, B.R. Lawn, Comm. Am. Ceram. Soc. 66 (1983) C-200.

149. G.R. Anstis, P. Chantikul, B.R. Lawn, D.B. Marshall, J. Am. Ceram. Soc. 64 (1981) 533.

150. D.B. Marshall, B.R. Lawn, A.G. Evans, J. Am. Ceram. Soc. 65 (1982) 561.

151. R.F. Pabst, in "Fracture mechanics of ceramics" Vol. 2, p. 555 (Proc. Symp. on fracture mech., Penn. State Univ. July 11-13 1973).

152. P.V.C. Manning, CEGB internal report NER/SSD/R472, March 1982.

153. Ito, Tomozawa, J. Am. Ceram. Soc. 65 (1982) 368.

154. A.V. Virkar, D.K. Shetty, A.G. Evans, Comm. Am. Ceram. Soc. 64 (1981) C-56.

155. N. Claussen, B. Mussler, M.V. Swain, Comm. Am. Ceram. Soc. 65 (1982) C-14.

156. B. Mussler, M.V. Swain, N. Claussen, J. Am. Ceram. Soc. 65 (1982) 566.

157. E.E. Underwood, "Quantitative stereology", Addison-Wesley 1970.

158. J.A. Szpunar, B.K. Tanner, J. Mat. Sci. 19 (1984) 3349.

159. H. Jain, H.L. Downing, N.L. Peterson, J. Non-Cryst. Sol. 64 (1984) 335.

160. J.B. Farmer, Borax Research Ltd., Chessington, Surrey, private communication.

161. J.E. Shelby, J. Am. Ceram. Soc. 66 (1983) 225.

162. P.W. McMillan, J. Non-Cryst. Sol. 52 (1982) 67.

163. P.F. James, in "Advances in ceramics" Vol. 4, "Nucleation and crystallisation in glasses", J.H. Simmons, D.R. Uhlmann, G.H. Beall (eds), American Ceramic Society 1981.

164. C.J.R. Gonzalez-Oliver, P.S. Johnson, P.F. James, J. Mat. Sci. 14 (1979) 1159.

165. P.F. James, J. Non-Cryst. Sol. 73 (1985) 517.

166. T. Izumitani, in "Treatise on materials science and technology" Volume 17, "Glass II", H. Tomozawa, R.H. Doremus (eds.) Academic Press 1979 pp. 115-172.

167. R.F. Cook, B.R. Lawn, T.P. Dabbs, P. Chantikul, Comm. Am. Ceram. Soc. 64 (1981) C-121.

168. J.F. Archard, Physics Bulletin 36 (1985) 212.

169. D. Johnson-Walls, A.G. Evans, D.B. Marshall, M.R. James, J. Am. Ceram. Soc. 69 (1986) 44.

170. S. Badrioch, Final report, Borax Research Limited.

171. A.E. Owen, Phys. Chem. Glasses 2 (1961) 87.

172. W.C. Hagel, J.D. MacKenzie, Phys. Chem. Glasses 5 (1964) 113.

173. Technical data sheet 4A, Borax Consolidated Ltd., London 1978.

174. "Mellor's modern inorganic chemistry", G.D. Parkes (ed.), Longman 1963.

175. B.L. Domicz, R.C. Scheidt, Report no. USNRDL-TR-752 (1964).

176. R. Thompson, Borax Research Ltd., Chessington, Surrey, private communication.

177. E. Hecht, A. Zajac, "Optics", Addison-Wesley 1979.

178. H.J. Mathers, University of Warwick, private communication.

179. "Neatcut" oil, Kayex Corporation, Rochester, NY14624, U.S.A.

180. Production Techniques Ltd., 13 Kings Road, Fleet, Hants.

181. Hyprez fluid type O/S (oil based) Engis Ltd.

182. G. Tomandl, H.A. Schaeffer, J. Non-Cryst. Sol. 73 (1985) 179.

183. M.D. Ingram, Phys. Chem. Glasses 28 (1987) 215.

184. D.R. Bridge, Ph.D. Thesis, University of Warwick 1987.

185. W.G. Amey, F. Hamburger, "A method for evaluating the surface and volume resistance characteristics of solid dielectric materials", Trans. A.S.T.M. 59 (1959) 1079.

186. Technical data sheet, Coors Ceramics UK Ltd., Glenrothes, Scotland.

187. R. Greef, R. Peat, L.M. Peter, D. Pletcher, J. Robinson, "Instrumental methods in electrochemistry", Ellis Horwood 1985.

188. C. Tubandt in Handbuch der Experimentalphysik 12 (1932) Chapter 3, p. 383.

189. F. Beniere, in "Physics of Electrolytes Volume 1 : Transport processes in solid electrolytes and in electrodes", J. Hlakik (ed.), Academic Press 1972.

190. D. Hind, thesis proposal, University of Leeds 1978.

191. B.L. Pletcher, J.R. Stevenson, A. Whitaker, J. Am. Ceram. Soc. 53 (1970) 95.

192. JCPDS 28-1178.

193. J.R. Lacher, J. Am. Chem. Soc. 74 (1952) 5293.

194. M. Falk, P.A. Giguere, Can. J. Chem. 35 (1957) 1195.

195. R.J.H. Clark, P.D. Mitchell, J. Chem. Phys. 56 (1972) 2225.

196. C.A. Jasper, 3rd Year Project Report, University of Warwick 1984.

197. S. Mason, Ph.D. Thesis, University of Warwick 1988.

198. B.R. Lawn, T.R. Wilshaw, J. Mat. Sci. 10 (1975) 1049.

199. J.L. Chermant, M. Coster, J. Mat. Sci. 14 (1979) 509.

200. A.H. Heuer, N. Claussen, W.M. Kriven, M. Ruhle, J. Am. Ceram. Soc. 65 (1982) 642.

201. M.V. Swain, Comm. Am. Ceram. Soc. 68 (1985) C-97.

202. J. Krogh-Moe, Acta Cryst. B30 (1974) 578.

203. G. J. Pratt. M. J. A. Smith, J. Phys. E: Sci. Instrum. 15 (1982) 927.

APPENDIX 1

Equivalent Circuit Responses Used in Simple Complex Impedance Analyses and Time Domain Spectroscopy

The algebraic equations for a selection of displayed circuits are shown on the following pages. A simple analysis is presented below which shows the Cole-Cole plot of an R-C parallel circuit to be truly circular.

For this circuit, the impedance Z may be obtained:

$$Z = \frac{R(1 - i\omega RC)}{1 + \omega^2 R^2 C^2} . \qquad (A1)$$

For a circle with centre at (a,b), radius r, the parametric equation is given by

$$(x-a)^2 + (y-b)^2 = r^2 . \qquad (A2)$$

Assuming the variation to follow a circular locus, the x (real) and y (imaginary) expressions for the impedance from A1 are substituted in A2 and the equation simplified to give

$$R^2 + (1 + \omega^2 R^2 C^2)(2b\omega R^2 C - 2Ra) + \omega^2 R^4 C^2 + (1 + 2\omega^2 R^2 C^2 + \omega^4 R^4 C^4)(a^2 + b^2) = r^2. \qquad (A3)$$

Since a,b and r cannot be functions of ω, the coefficients can be examined separately:

ω^0: $R^2 - 2Ra + a^2 + b^2 = r^2$ (A4)

ω^1: $2bR^2C = 0 \quad > b = 0$ (A5)

ω^2: $-2aR^3C^2 + R^4C^2 + 2R^2C^2(a^2 + b^2) = 0.$ (A6)

Since $b = 0$ from (A5), this equation simplifies to give

$$R(R - 2a) + 2a^2 = 0 \qquad (A7)$$

Combining (A4) and (A7), we obtain

$$a^2 = r^2 \quad > \quad a = \pm r.$$

Substituting in (A4) gives a = R/2.

Therefore the response of a simple R-C parallel circuit has been shown to be semicircular, with the centre at (R/2,0), radius R/2, a result often referred to in texts introducing the features of Cole-Cole plots.

Case 1 : Time domain.

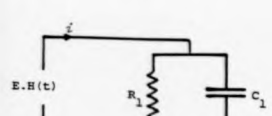

$$i = \frac{E}{R_1} + EC_1\delta(t)$$

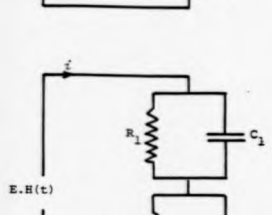

$$i = E\left(\frac{\delta(t)}{l} + \frac{k}{m} + \left(\frac{j}{l} - \frac{m}{l^2} - \frac{k}{m}\right)\right)$$

where:-

$$a = \frac{1}{R_1C_1} \; ; \; b = \frac{1}{R_2C_2}$$

$$j = a + b \; , \; k = a.b \; ;$$

$$l = \frac{1}{C_1} + \frac{1}{C_2} \; ; \; m = \frac{b}{C_1} + \frac{a}{C_2} \; .$$

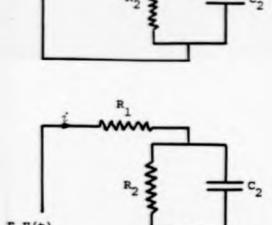

$$i = \frac{E}{R_1}\left(\frac{ab}{(x^2 - y^2)} + (1-k)\exp(xt).\cosh(yt) + \frac{(a+b+x(1+k))}{y}\exp(xt).\sinh(yt)\right)$$

where:-

$$a = \frac{1}{R_1C_1} \; ; \; b = \frac{1}{R_2C_2}$$

$$x = -\tfrac{1}{2}\left(a + b + \frac{1}{R_1}\left(\frac{1}{C_2} + \frac{1}{C_3}\right)\right) \; ;$$

$$y = \sqrt{\left(x^2 - ab - \frac{1}{R_1}\left(\frac{a}{C_2} + \frac{b}{C_2}\right)\right)}$$

$$k = \frac{ab}{x^2 - y^2} \; .$$

Case 2 : Frequency domain.

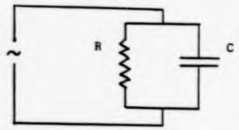

$$Z = \frac{R - jwR^2C}{1 + w^2R^2C^2}$$

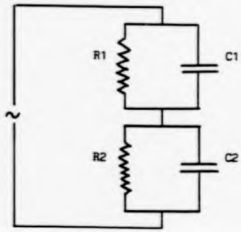

$$Z = \frac{R1}{1 + w^2R1^2C1^2} + \frac{R2}{1 + w^2R2^2C2^2} - jw\frac{R1^2C1}{1 + w^2R1^2C1^2} + \frac{R2^2C2}{1 + w^2R2^2C2^2}$$

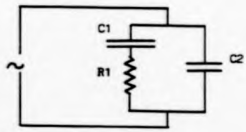

$$Z = \frac{R1 - j\frac{1}{wC1} + \frac{C2}{wC1^2} + wR1^2C2}{1 + \frac{C2}{C1}^2 + w^2R1^2C2^2}$$

Equivalent circuits used in the optimisation routine formulated during the course of this work.

1.

$$Z = \frac{R - j\omega R^2 C}{1 + \omega^2 R^2 C^2}$$

2.

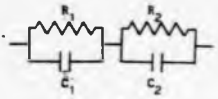

$$Z = \frac{R_1 - j\omega R_1^2 C_1}{1 + \omega^2 R_1^2 C_1^2} + \frac{R_2 - j\omega R_2^2 C_2}{1 + \omega^2 R_2^2 C_2^2}$$

3.

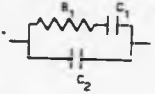

$$Z = \frac{\omega(C_1+C_2)R_1C_1 - \omega^2 R_1 C_1 C_2}{\omega^4 R_1^2 C_1^2 C_2^2 + \omega^2 (C_1+C_2)^2} + \frac{j\omega(C_1+C_2-R_1^2\omega^2 C_1^2 C_2)}{\omega^4 R_1^2 C_1^2 C_2^2 + \omega^2 (C_1+C_2)^2}$$

4.

$$Z = R - \frac{j\omega C}{\omega^2 C^2}$$

5.

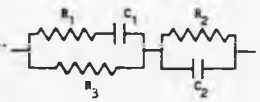

$$Z = \frac{R_3(1 + j\omega R_1 C_1)}{1 + j\omega C_1 (R_1 + R_3)} + \frac{R_2}{1 + j\omega R_2 C_2}$$

6.

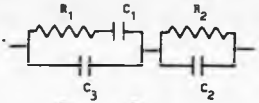

$$Z = \frac{1 + j\omega R_1 C_1}{-\omega^2 R_1 C_1 C_3 + j\omega(C_1 + C_3)} + \frac{R_2}{1 + j\omega R_2 C_2}$$

7.

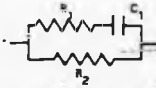

$$Z = \frac{j\omega C_1}{1 + j\omega R_1 C_1} + \frac{1}{R_2}$$

8.

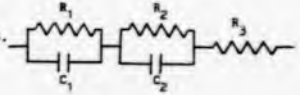

$$Z = \frac{R_1 - j\omega R_1^2 C_1}{1 + \omega^2 R_1^2 C_1^2} + \frac{R_2 - j\omega R_2^2 C_2}{1 + \omega^2 R_2^2 C_2^2} + R_3$$

9.

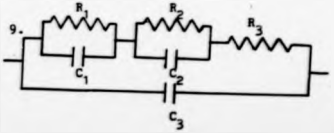

$$\frac{\dfrac{R_1 - j\omega R_1^2 C_1}{1 + \omega^2 R_1^2 C_1^2} + \dfrac{R_2 - j\omega R_2^2 C_2}{1 + \omega^2 R_2^2 C_2^2} + R_3}{1 + j\omega C_3 \dfrac{R_1 - j\omega R_1^2 C_1}{1 + \omega^2 R_1^2 C_1^2} \dfrac{R_2 - j\omega R_2^2 C_2}{1 + \omega^2 R_2^2 C_2^2} + R_3}$$

APPENDIX 2

Paper submitted to Journal of the American Ceramic Society

THE BORIC OXIDE ANOMALY - A LINK BETWEEN MACROSCOPIC AND MICROSCOPIC MEASUREMENTS?

A P Kemp* and D Holland

Centre for Advanced Materials

Physics Department

Warwick University

COVENTRY CV4 7AL

U.K.

* Now at: Physics Department, University of Nottingham, University Park, Nottingham, U.K.

A recent publication by Piguet and Shelby[1], in which the silver and alkali metal borate glass systems have been structurally likened on the basis of physical property comparisons, has once again promoted discussion of the nature of the boric oxide anomaly and has shown that a closer examination of the available data is required before such comparisons can be made. Furthermore, such an examination can also reveal hitherto unnoticed features.

As one example of the similarity of the two systems, Piguet and Shelby display the variation in molar volume with increasing Ag_2O content, upon which is superimposed a "line of best fit" for the sodium borate case obtained from the results of other workers[2]. This does superficially appear to be "in excellent agreement", as stated by the authors, however closer examination of the original silver data[1] shows the existence of a "wiggle" superimposed upon a monotonically decreasing variation of molar volume with increasing silver oxide content. A comprehensive re-analysis of density data from the references cited[2] shows that a similar feature also occurs in the lithium, sodium and potassium systems. Some examples of this are shown in figure 1. In all cases the "wiggle" can be seen in the 10-25 mol% modifer concentration range.

The observed scatter in the concentration of R_2O at which this feature occurs may be attributable to departures from the nominal compositions due to melting and storage problems. (Even where compositional analyses have been performed this was usually of one component only, whereas any structural effect which arises from the introduction of extra oxygen into the borate network will reflect not only R_2O content but also the presence of H_2O and CO_2 impurities.)

As has been discussed in a recent review[3], previous interpreta-

tions of the microscopic structural variations in alkali metal borate glasses from first principles seem to explain limited specific macroscopic property composition changes on a qualitative basis only. Here we attempt to interpret this "wiggle" by extending early ideas of Krogh-Moe[4], which appear to have been neglected by more recent reviews, in the following argument.

Examination of the now widely accepted variation of N_4 (the ratio of 4-coordinated boron to total boron atoms) with modifier content of borate glasses, shows good agreement over the region 5-20 mol% concentrations with the function $x/1-x$ as initially depicted by Bray and O'Keefe[5], shown as the dotted line in Fig. 2. For the purpose of illustration, the more complete theoretical description of the variation of N_4 with concentration evaluated by Bray et al.[6] (shown as the dashed line in Fig. 2) will be modelled to a general Gaussian lineshape of the form $Aexp[-B(x-C)^2]$, fitting within reported experimental scatter, as depicted as the full line in fig. 2.

If, as a gross simplification, the metal ions are presumed to take no active structural role, then the ratio N_4 could be taken as a measure of the rate of change of structure with added oxygen concentration, from the "planar" boroxol ring structure composed purely of trigonal boron atoms, found mainly in low-modifier containing glasses, to the more cross-linked network containing approximately equal concentrations of 3- and 4-coordinated borons at higher modifier concentrations. Consider a glass having a general molar composition $xM_2O.(1-x)M_2O_3$, where M represents a monovalent metal atom. If the Avagadro constant is defined as N_A, it is readily apparent that there are $2N_Ax$ metal atoms and $(2-2x)N_A$ boron atoms present. Let us now think of the glass as being composed of a

pseudo-random arrangement of spheres with radii equal to the B-O separation, and that the radii for 3- and 4-coordinated boron-centred spheres are different. This postulate is essentially linking the Bernal hard sphere model with the RCN concept, which have been shown previously to be incompatible [7]. Therefore, representing the volumes of these spheres by V_{B3} and V_{B4} respectively, and ignoring the contribution from the metal ions by assuming them to accommodate themselves in the 'gaps' in the network, we may express the molar volume as:-

$$m.v. = N_A N_3 (2-2x) V_{B3} + N_A N_4 (2-2x) V_{B4}$$

where $N_3 = 1-N_4$, $N_4 = A\exp(-B(x-C)^2)$. Defining the reduced variables $V_{B3}' = 2N_A V_{B3}$ and $B_{B4}' = 2N_A V_{B4}$ to reduce errors in the ensuing analysis, simplifying and substituting the previously determined values for A, B and C leads to:-

$$m.v. = (1-x)(V_{B3}' + (V_{B4}' - V_{B3}')[0.46\exp(-20(x-0.39)^2)])$$

Appropriate values for V_{B3}' and V_{B4}' were obtained by trial to produce a plot of the general form shown in fig. 3. Comparison with experimental data shows some similarities, and this could therefore be thought of as a representative model within limitations.

Comparison with experimental data shows some similarities, and this could therefore be thought of as a representative model within limitations. Although the contribution from the alkali ions has been neglected, the coordination requirements of the model cannot be dismissed. At present this modification is represented by a concentration-independent constant. In reality it is felt that this simplistic assumption is not valid, particularly at low alkali contents, where the molar volume may be greatly increased due to the inception of the cross-linked four-coordinated boron modification.

Considering the dynamics of the network in addition to its volume, thermal expansion is envisaged as a measure of the width of the potential well of a given system, which is controlled by the symmetry of the (external) local environment surrounding a given atom. Therefore, for increased localised symmetry, an associated decrease in linear thermal expansion coefficient might be expected, such as with a change from trigonal to tetrahedral borons in a borate glass. Hence, a measure of the dependance of thermal expansion coefficient on modifier concentration might be obtained by differentiating N_3 (= 1-N_4) with respect to x, thereby obtaining a curve similar to that observed experimentally, as shown in fig. 4. The model is not quantitative, however, producing a slightly broader minimum than is observed experimentally.

If this simple concept is valid for higher modifier concentrations, then a maximum in the thermal expansion vs. modifier concentration curve is predicted from the point of inflection in the NMR data at ~50 mol% modifier content, which is not inconsistent with the thermal expansion data presented by Shelby[8].

Further examination of published thermal expansion vs. concentration curves seem to imply that results obtained by this technique are heavily dependent upon the specimen preparation process. The minimum in the curve presented by Piguet and Shelby[1] appears to be sharper than for other data recently reported for the sodium borate binary system[9,10] and although it is in agreement with some more comprehensive results from alkali borate glasses in general[8], it is broader in turn than other published results[11]. A possible explanation for the observed differences in the width and depth of these minima may be due to the varied melting times used in specimen preparation, which although

justified from the point of view of minimisation of preferential volatilisation of a given component, may imply the retention of water[9] which can significantly alter viscosity and thermal expansion behaviour. In addition, the above considerations should affect the Tg value*, however there appears to be no simple relationship between this parameter and melting temperature or time. Another more obvious reason for the discrepancy in the Tg values inferred from dilatometry reported by Piguet and Shelby[1] and Boulos and Kreidl[12] may be due to inaccurate thermocouple positioning in the event of a badly assessed thermal gradient within the dilatometer used for one of the sets of measurements. To this end, these Tg values have been compared with independently obtained viscosity results[1], bearing in mind that Tg corresponds to a viscosity of 10^{11}-10^{12} Poise (Mg point)[13]. Consistency with Piguet and Shelby's results was obtained, assuming that the viscosity had been measured in Poise, rather than Poiseuille. This variation in thermal expansion behaviour may be thought to indicate that quantitative data comparison performed in the work under discussion is invalid.

A somewhat tentative extension to the model presented above may also explain a previously-reported conductivity anomaly. If ionic conductivity is thought to depend upon the ease of ion movement through the network, then it may further be related to the vibrational motion of the "stationary" ions surrounding a given conduction pathway, which in turn

---

*This may also arise from residual stresses within the glasses[14], bringing the thermal history of the specimens into question, with the chosen "anneal" presumably being a fine balance between strain relief and nucleation.

will be affected by the network distortion. Therefore, if this argument is valid, then a conductivity minimum will exist at ~22mol%, and a corresponding maximum at ~50mol% modifier. Martin and Angell[15] recently reported a conductivity maximum in sodium aluminoborate glasses of general composition $xNa_2O.(1-x)(0.87B_2O_3.0.13Al_2O_3)$. If we assume the aluminium atom to be 4-coordinated it will require the presence of a fixed sodium ion to preserve electroneutrality[13] and may be considered to be removing modifier from the borate network. Their data may then be reduced to obtain the effect of ionic conduction purely within the residual borate network. The reported maximum is at ~50mol% sodium oxide, which when converted to the borate network alone, reduces to an equivalent composition $50Na_2O.50B_2O_3$, in excellent agreement with that predicted.

Unfortunately, it would appear that glasses of low soda content could not be formed in a condition amenable to production of good conductivity specimens and so the position of the associated minimum cannot be verified. However, Tg values for glasses having a lower soda content have previously been reported by the same authors [16], which may be reduced in a similar manner to verify the initial assumption, and further test the implications of our model.

A simplistic view of viscosity (of which Tg may be deemed a measure in a naive interpretation) is of ions "slipping" over each other under the influence of an applied shear force. As such, a measure of the interatomic bond strength might be obtained from the width and depth of the potential well presented in the thermal expansion argument. That is to say, a deep and narrow potential well would imply a high viscosity material. Taking the thermal expansion analogue still further leads us to the conclusion that a high viscosity would be observed in a borate glass

having a low thermal expansion coefficient. This aspect of the model, however, has not been researched in detail. If the above tenuous link is valid, then a viscosity maximum corresponds to a thermal expansion minimum, i.e. at ~22mol% modifier. Similarly a viscosity minimum would be expected at ~50mol% modifier.

Taking the maximum and minimum (the latter is still more tenuous, since the earlier Tg data [16] would not seem to imply a local minimum but a shoulder before decreasing still further) Tg values then, the corresponding soda concentrations are respectively ~25 and ~68mol%. Reducing these values as outlined above gives corrected values of ~19 and ~70mol%. Whilst the first value is in reasonable agreement with our postulate, the latter is obviously quite unacceptable. Any further qualitative structural inferences to explain this discrepancy are, we feel, at this time, of little intrinsic value.

As one further point, returning to the work of Piguet and Shelby, the structure of the crystalline analogues of the sodium and silver borate systems has previously been reported by Krogh-Moe [17-19], thereby adding weight to their argument of a sodium-silver analogy by virtue of the structural group analogue employed in many of the indirect inferences made in the determination of glass structure.

Acknowledgements

We are grateful to the SERC for provision of a studentship (APK) and to Borax Research (UK) for initiating this project.

References

1. J L Piguet and J E Shelby, "Preparation and properties of silver borate glasses", J.Am.Ceram.Soc. 68 (1985) 450

2. From the Physical Sciences data 15 "Handbook of glass data pt. B: Single component and binary non-silicate oxide glasses", Mazurin et al. (eds.) Elsevier 1986

3. D R Uhlmann, R R Shaw, "Thermal expansion of alkali borate glasses and the boric oxide anomaly", J.Non-Xtal.Sol. 1)1969) 347

4. J Krogh-Moe, "Relation of structure to some physical properties of vitreous and molten borates", Arkiv för Kemi 14 (1959) 553

5. P J Bray, J G O'Keefe, "Nuclear magnetic resonance investigations of the structure of alkali borate glasses", Phys.Chem.Glasses 4 (1863) 37

6. P B Bray, R V Mulkern, E J Holupka, J.Non-Xtal.Sol. 75 (1985) 37

7. J L Finney, in "The structure of Non-Crystalline Materials", P H Gaskell (eds.) Taylor and Francis 1977

8. J E Shelby, "Thermal expansion of alkali borate glasses", J.Am.Ceram. Soc. 66 (1983) 225

9. S V Stolyar, V P Klyuev, A V Bulaeia, Soviet J.GlassPhys.Chem. 10 (1984) 291

10. W L Konijnendijk, Philips Res.Repts.Suppl. 1 (1875)

11. S Suzuki, Y Abe, "The free volume of some oxide glasses at the transition temperature", 43 (1981) 141

12. E N Boulos, N J Kreidl, "Structure and properties of silver borate glasses", J.Am.Ceram.Soc. 54 (1971) 368

13. P W McMillan, "Glass Ceramics", Academic Press 1979

14. H Rotger, in "Amorphous materials", R W Douglas, B Ellis (eds.) Wiley - Interscience 1970

15. S W Martin and C A Angell, American Ceram.Soc.Comm. 7 (1984) C-148

16. S W Martin and C A Angell, "Glass formation and transformation temperatures in sodium and lithium borate and aluminoborate melts up to 72 real % alkali", J.Non-Xtal.Sol. 66 (1984) 429

17. J Krogh-Moe, "The infrared spectra of some vitreous and crystalline borates", Arkiv för Kemi 12 (1958) 475

18. J Krogh-Moe, "Vitreous potassium pentaborate modifications", Arkiv för Kemi 14 (1959) 567

19. J Krogh-Moe, "Description of the infrared spectra of boron oxide and alkali borate glasses", Phys.Chem.Glasses 6 (1965) 46

Figure Captions

Figure 1 Glass molar volumes derived from density data in the literature indicated, as a function of modifier concentration in x%R_2O (100-x)% B_2O_3.

Figure 2 Variation of N_4 (the ratio of 4-coordinated boron to total boron) with concentration of modifier in x% R_2O (100-x)% B_2O_3. The dotted line corresponds to the function x/(1-x) (Bray and O'Keefe [5]) and the dashed line to the theoretical fit by Bray et al [6]. The full line is a general Gaussian of the form $Aexp[-B(x-C)^2]$. Values are as follows:- A = 0.46, B = 20.0, C = 0.39.

Figure 3 A comparison of observed molar volume variation with concentration of modifier with that predicted by the formula.

$m.v = (1-x)(V_{B3}' + (V_{B4}' - V_{B3}')[0.46\ exp(-20(x-0.39)^2)])$

$V_{B3}' = 36.25$, $V_{B4}' = 47.5$

Figure 4 Comparison of the dependence of thermal expansion on modifier content with the differential of N_3 (= $1-N_4$) with respect to x.

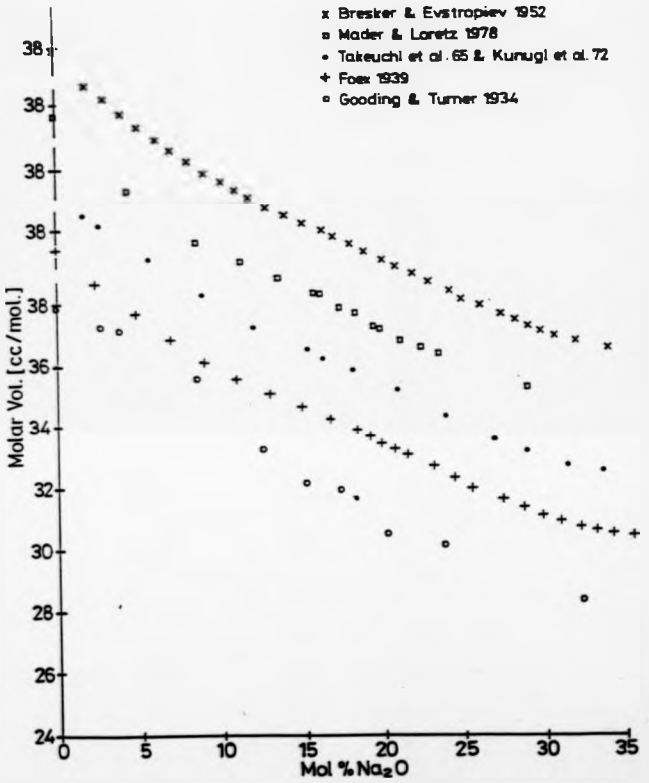
x Bresler & Evstropiev 1952
▫ Mader & Loretz 1978
• Takeuchi et al. 65 & Kunugi et al. 72
+ Foex 1939
▫ Gooding & Turner 1934
Molar Vol. [cc/mol.]
38
36
34
32
30
28
26
24
0
5
10
15
20
25
30
35
Mol % Na2O

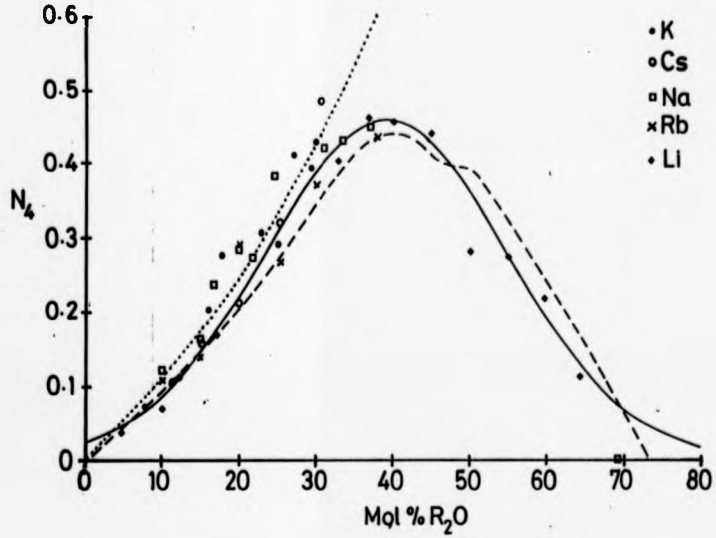
0·6
0·5
0·4
0·3
0·2
0·1
0
N_4
0
10
20
30
40
50
60
70
80
Mol % R_2O
• K
o Cs
□ Na
× Rb
• Li

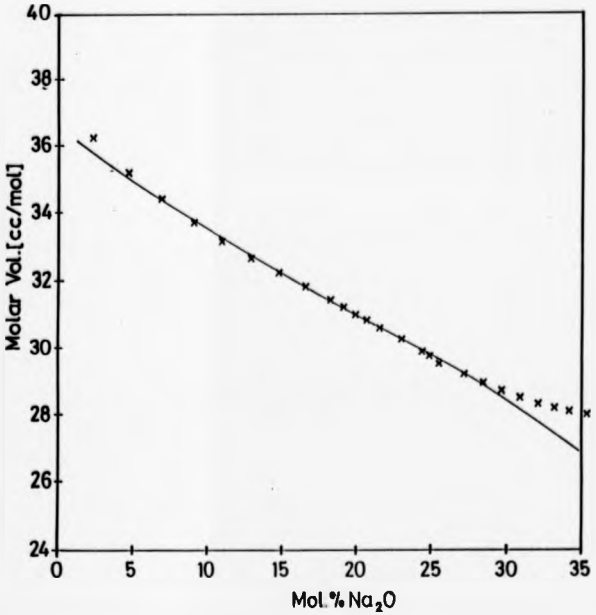
40
38
36
34
32
30
28
26
24
Molar Vol.[cc/mol]
0
5
10
15
20
25
30
35
Mol.% Na_2O

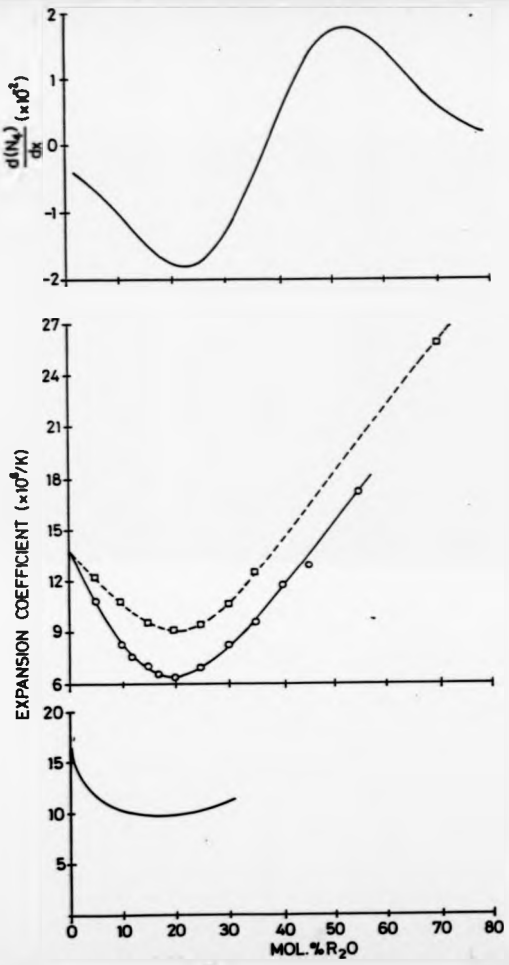
$\frac{d(N_4)}{dx}$ (×10²)
2
1
0
-1
-2
EXPANSION COEFFICIENT (×10⁶/K)
27
24
21
18
15
12
9
6
20
15
10
5
0
10
20
30
40
50
60
70
80
MOL.% R_2O

APPENDIX 3

Materials Science Forum Volumes 19-20 (1987) pp. 147-166

NMR OF SOME HALIDE CONTAINING GLASSES

R.S. Aujla, R. Dupree, D. Holland and A.P. Kemp
Centre for Advanced Materials, Department of Physics
University of Warwick, Coventry CV4 7AL (UK)

INTRODUCTION

The development of glasses for particular technological applications generally requires an understanding of the structure of the glass and its relation to corresponding crystalline materials. The various techniques developed for the study of oxide based glasses have been extended to the halide glasses with varying degrees of success in producing an understanding of the structural units involved. A relatively new technique is that of magic-angle-spinning (MAS) NMR. Static NMR has always been difficult to interpret for solids, particularly glasses, although excellent work has been carried out on borate systems, largely by Bray.[1] Only certain nuclei are suitable for NMR studies and, of these, some present greater problems than others. The main parameters which control the ease of acquisition of data are isotopic abundance and relaxation time. The parameters which control the ease of interpretation of data are: the range of chemical shifts, the linewidth, and line shape. We can subdivide those nuclei of interest to halide glasses as shown in Table 1. From the table, it can be seen that certain isotopes are of low natural abundance and require either isotopic enrichment (eg.^{17}O) or long acquisition times. Spin $\frac{1}{2}$ nuclei may present problems of lack of efficient relaxation mechanisms. Quadrupolar nuclei produce complex line shapes depending on size of the quadrupole moment and the asymmetry of the site occupied. If the resonances obtained are very broad, then the detailed information of various sites may be obscured by this width. The three major contributions to the line broadening are:- quadrupolar interactions for $I > \frac{1}{2}$; chemical shift anisotropy and dipolar broadening, where the local field at a nucleus is modified, from that applied, by the influence of neighbouring dipoles. In a solution, these broadening mechanisms are eliminated by the averaging nature of molecular motion. This can be simicked for solids by rotating the sample at high speed about an axis oriented at 54.7^{0} to the applied field - so-called "magic angle spinning".[2] The different chemical shifts corresponding to distortions of environment give additional broadening in a glass and this broadening cannot be eliminated by spinning. This paper aims to give examples of the application of this technique to halide containing glasses and to highlight some of the problems involved.

FLUORIDE GLASSES

In a ZBLAN glass one can, in principle, observe all the nuclei present i.e. ^{91}Zr, $^{135/137}Ba$, ^{139}La, ^{27}Al, ^{23}Na and ^{19}F. All, except ^{19}F, have spin $I > \frac{1}{2}$ and are likely to exhibit considerable quadrupolar broadening of the lineshape. This will be particularly so for low symmetry environments, and is a problem which increases with atomic number.

^{19}F. High resolution spectra of ^{19}F in quartz glass have been reported by Yonemar[1,2]. It is found that ^{19}F resonance linewidths in crystalline fluorides are generally quite broad (~15kHz); any variation from crystallinity can broaden the linewidth even further. Consequently, the broad static spectrum from a glass cannot be narrowed simply by spinning. We are investigating the use of multiple pulse sequences to reduce the residual broadening. Table 2 lists some values for static linewidths measured at 15MHz for some crystalline and glassy fluorides. It should be noted that the values for the glasses are large enough to indicate the presence of two or more fluorine types in the glass.

$^{135/137}Ba$. Both isotopes of barium produce relatively narrow static lines (~2kHz) from systems possessing cubic geometry. ^{135}Ba has a smaller quadrupolar moment than ^{137}Ba. Consequently the ^{135}Ba lines are approximately half as broad as those from ^{137}Ba. For instance, ^{135}Ba and ^{137}Ba static linewidth (FWHM) in BaF_2 at 40MHz are found to be 580Hz and 1100 Hz respectively. MAS of BaF_2 effectively narrows the ^{137}Ba line to 260Hz.[Fig.1]. However, the barium line in glass is likely to be much broader than in BaF_2 due to the range of site distortions present.

^{23}Na and ^{27}Al. Usually both ^{23}Na and ^{27}Al nuclei give rise to broad featureless resonance lines in glasses. Fig. 2 shows a series of ^{23}Na and ^{27}Al MAS spectra following heat treatments of ZBLAN glass at 315°C and 416°C. In ^{23}Na spectra, it is seen that on heating the glass to 416°C, the FWHM linewidth is reduced by 40%. This indicates that the Na environment has become more symmetric and that it may be present in the crystallised phase. In addition, the resonance shifts by approximately 4ppm from -21.9 to -17.7ppm (wrt dilute aqueous NaCl) i.e. towards the resonance position of NaF indicating that Na may be octahedrally coordinated by F in the crystallised phase. In ^{27}Al spectra, chemical shift and linewidth remain unchanged on heat treatment and indicate that either ^{27}Al site is very distorted in these materials or that Al is not present in the crystallised phase. The ^{27}Al peak position of -8.1ppm (from $Al(H_2O)_6^{3+}$) is characteristic of octahedral coordination.

HALOBORATE GLASS-CERAMIC, FAST-ION CONDUCTORS

If certain alkali borate glasses are doped with metal halides they become capable of producing glass-ceramics with unexpectedly high ionic conduction. Some systems give 3 orders of magnitude increase in conduction on devitrification. The mechanism of the increased conductivity is not well understood. NMR charging has shown that one of the crystal phases appears to provide the major conduction path but more evidence is required before it is possible to tailor compositions to optimise conduction. ^{23}Na has been studied by MAS-NMR in borax + NaCl glasses and glass-ceramics to obtain additional information about the site occupancy of Na^+ (the mobile ion) in these materials. Fig. 3 shows the ^{23}Na spectra for glassy borax ($Na_2B_4O_7$) and for borax doped with 30 mole % NaCl. The spectra are very similar being centred at -9ppm and very broad ~35ppm. Fig. 4 shows the ^{23}Na spectra from

the devitrified materials where now distinct differences can be observed. The complexity of the spectrum from crystalline borax arises because there are 4 crystallographically distinct Na sites all of which have low symmetry giving rise to complex quadrupole line shapes. The glass ceramics produced from 70 borax 30 NaCl gives a simpler spectrum in which three sites are apparent:- site I - a highly symmetric site at -6ppm which is typical of an octahedral site (e.g. NaCl -8ppm); site II at -1.7ppm; and site III at ~ -9ppm. The questions now to be answered are (a) which sites are responsible for high conductivity and (b) are the properties and site symmetries a result of the extra sodium ion concentration or does the presence of chlorine play a vital role? To assess this, various sodium oxide doped glasses were prepared e.g. 70 borax 30 Na_2O and 70 borax 15 Na_2O to simulate equivalent anion doping and equivalent cation doping respectively. The ^{23}Na spectra of the devitrified glasses are shown in Fig. 5. Neither spectrum shows site I or site III resonances, nor do they resemble the borax spectrum. The site II resonance is present. Sodium oxide doped glass-ceramics do not possess fast-ion conduction properties. Thus we can conclude that that Na^+ in one or both of
site I and site III are responsible for high conduction and chlorine plays an important part in the creation of these sites.

REFERENCES

[1] e.g. P. J. Bray et al. J.Non.Cryst.Solids 52 65-66 (1982)
[2] E. R. Andrew, Progress in NMR Spectroscopy 8 1-39 (1971)
[3] S. Yonemori, A. Masui and M. Washiro, Yogyo-Kyokai Shi 94 (8) 861 (1986)

TABLE I NMR parameters for nuclei of importance to halide glasses

Nucleus	Spin (I)	Abundance (%)	Sensitivity (rel. ^1H)	Chemical Shift Range (ppm)	Quadrupole Moment $10^{-28}e.m^2$
Abundant spin ½					
^{19}F	½	100	0.83	-250 to 550	-
Dilute spin ½					
^{207}Pb	½	22.6	$2.07\ 10^{-3}$	-5850 to 4550	-
Quadrupole					
^{27}Al	5/2	100	0.21	-225 to 220	0.15
^{23}Na	3/2	100	$9.25\ 10^{-2}$	-170 to 150	0.1
^{17}O	5/2	$3.7\ 10^{-2}$	$1.08\ 10^{-5}$	-56 to 1598	$-2.6\ 10^{-2}$
^{35}Cl	3/2	75.53	$3.55\ 10^{-3}$	-1050 to 80	-0.1
^{37}Cl	3/2	24.47	$6.63\ 10^{-4}$	-18 to 12	
^{91}Zr	5/2	11.23	$1.06\ 10^{-3}$		-0.21
^{135}Ba	3/2	6.59	$3.33\ 10^{-4}$		0.18
^{137}Ba	3/2	11.32	$7.76\ 10^{-4}$		0.28
^{139}La	7/2	99.9	$5.91\ 10^{-2}$		0.22

TABLE 2 Static ^{19}F linewidths, measured at 15 MHz

Test Material	Crystalline Form	Linewidth (FWHM), kHz
AlF_3	Triclinic	48
BaF_2	Cubic	15
BiF_3	Cubic	44
CaF_2	Cubic	25
LaF_3	Distorted Trigonal	43
NaF	Cubic or Tetrahedral	31
PbF_2	Rhombohedral	19
ZrF_4	Hexagonal	30
ZrF_4-BaF_2-LaF_3 65.0 25.0 10.0	-	67
ZrF_4-BaF_2-NaF-LaF_3 53.9 16.7 27.4 2.0	-	82

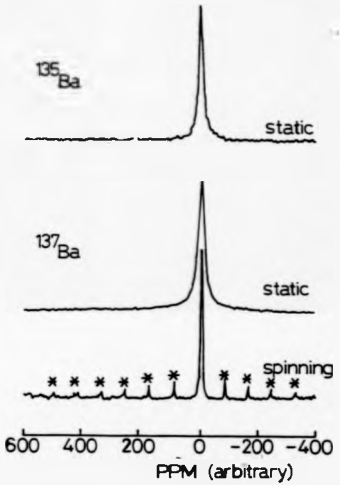

* spinning side bands

Fig. 1 ^{135}Ba and ^{137}Ba NMR spectra of BaF_2

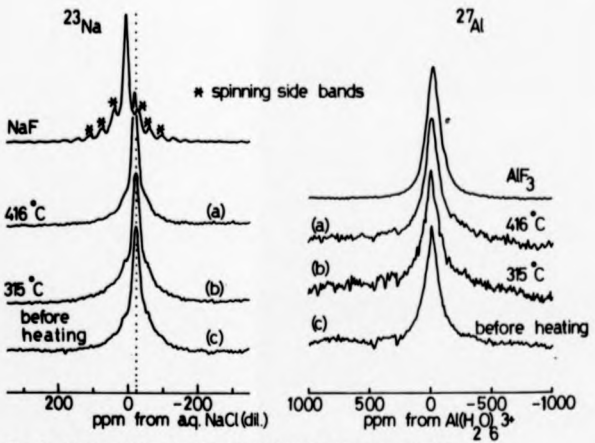

Fig. 2 NMR spectra of ZBLAN system (a,b,c), NaF and AlF_3

Fig.3 ^{23}Na spectra of glasses

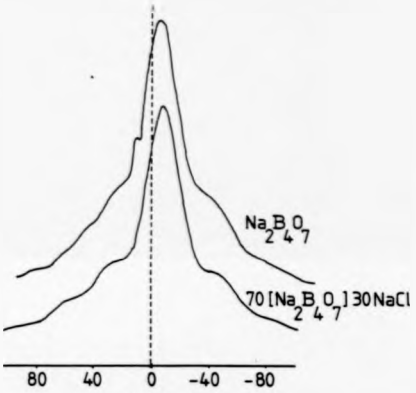

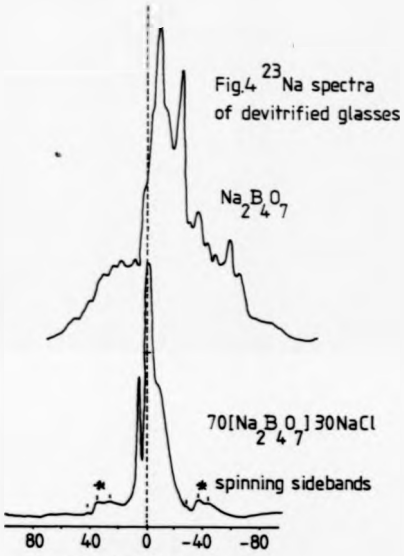

Fig.4 ^{23}Na spectra of devitrified glasses

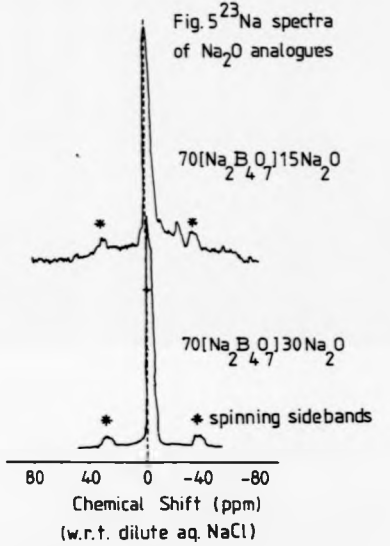

Fig. 5 ^{23}Na spectra of Na_2O analogues